

COMMISSIONING AND OPTIMIZATION OF A TOTAL SKIN ELECTRON THERAPY TECHNIQUE USING A HIGH DOSE RATE ELECTRON FACILITY

By

Yousif Abd Allah Mohammed Yousif

Dissertation submitted to comply with the requirements for the M.Med.Sc degree in the Faculty of Health Sciences, Medical Physics Department, at the University of the Free State.

June 2007

Supervisor: Prof. C. A. Willemse

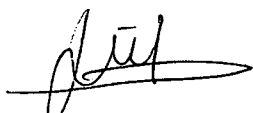
Universiteit van die
Vrystaat
BLISSIEFEN

13 AUG 2008

UV SAKELLE BIBLIOTEEK

I, Yousif Abd Allah Mohammed Yousif, declare that the dissertation hereby submitted by me for the MASTER OF MEDICAL SCIENCE: MEDICAL PHYSICS degree at the University of the Free State is my independent effort and has not previously been submitted for a degree at another university or faculty. I furthermore waive copyright of the dissertation in favour of the University of the Free State.

Signed at BLOEMFONTEIN on this twenty fifth day of JUNE Y 2007



Y. A. M. Yousif

DEDICATION

This thesis is dedicated with love to my parents

Yousif. A. Mohammed

ACKNOWLEDGEMENTS

With a deep sense of gratitude, I would like to express my sincere thanks to my promoter Prof. C. A. Willemse for his expert guidance, advice, availability and continuous support during the research and revising of the dissertation. It is highly appreciated.

I specially thank Mr Kobus van der Walt and Claude Wainwright from the National Hospital mechanical workshop for their design of the platform and solid water phantom. Furthermore my sincere thanks to Mr Ben Kriel from ELEKTA for his co-operation and valuable advice in operating the Precise Linear accelerator in a HDRE special procedure mode.

My gratefulness to all the staff members and colleagues in the Department of Medical Physics at the University of the Free State for help directly or indirectly enabling the compilation of my dissertation, especially Dr. F. Du Plessis for his valuable suggestions and technical support during simulation and programming. My sincere thanks are due to Mr Willie Shaw for his co-operation and assistance in many aspects concerning the simulation.

Also I would like to thank the Ministry of Higher Education and Scientific Research-Sudan, for sponsoring me all the way. Furthermore special thanks are due to all my superiors and colleagues at Alneelain University-Khartoum-Sudan, for affording me the opportunity to complete my research in the Republic of South Africa.

Mostly, I extend my sincere and heartfelt thanks to my family for the underlying support and encouragement. I am thankful to, Aunt P and her family, as well as friends for their advice and encouragement.

Finally, I thank every one else in or outside the department contributed to making this research possible.

LIST OF ABBREVIATIONS USED

TSET	Total Skin Electron Therapy
MC	Monte Carlo
CT	Computer Tomography
SSD	Source to Surface Distance
PDD	Percentage Depth Dose
MU	Monitor Units
CM	Component Module
PPSF	Primary Phase Space File
SPSF	Secondary Phase Space File
ECUT	Electrons Cutoff Energy Value
PCUT	Photons Cutoff Energy Value
2D	Two Dimensional
3D	Three Dimensional

CONTENTS

DEDICATION

ACKNOWLEDGEMENTS

LIST OF ABBREVIATIONS

CHAPTER 1

INTRODUCTION

1.1	Radiotherapy.....	1
1.2	Types of radiotherapy treatment.....	4
1.2.1	Radical radiotherapy.....	4
1.2.2	Adjuvant radiotherapy.....	4
1.2.3	Chemoradiotherapy.....	5
1.2.4	Intraoperative radiotherapy.....	5
1.2.5	Palliative radiotherapy.....	5
1.3	Electron beam in radiotherapy.....	6
1.4	Electron therapy treatment planning.....	7
1.5	Monte Carlo simulation techniques.....	8
1.5.1	Advantage of Monte Carlo simulation.....	9
1.5.2	Limitations of Monte Carlo simulation	10
1.6	Monte Carlo simulation of linear accelerator head.....	11
1.7	Aims of the study.....	12
1.8	Specific objectives.....	12

CHAPTER 2

LITERATURE REVIEW

2.1	Medical linear accelerator.....	14
2.1.1	Introduction.....	14
2.1.2	Principles of operation.....	14
2.1.3	The linac photon and electron beams.....	15

2.1.4	Beam collimation and monitoring.....	16
2.2	Photon interaction processes.....	16
2.2.1	Photoelectric absorption.....	17
2.2.2	Compton Effect (Incoherent).....	17
2.2.3	Pair production.....	18
2.2.4	Coherent scattering.....	19
2.3	Electron interaction Processes.....	20
2.3.1	Collisional energy loss.....	20
2.3.2	Radiative energy loss (bremsstrahlung production).....	21
2.3.3	Electron stopping powers	21
2.3.3.1	Mass collision stopping power	22
2.3.3.2	Radiative stopping power.....	22
2.3.4	Restricted stopping power.....	23
2.3.5	Range Concept (CSDA).....	23
2.3.6	Radiation dosimetry.....	24
2.4	Total skin electron therapy (TSET).....	25
2.4.1	TSET irradiation requirements.....	27
2.4.1.1	Irradiation beam requirements.....	27
2.4.1.2	Irradiation room requirements.....	31
2.4.2	Irradiation techniques.....	31
2.4.2.1	Translational techniques.....	32
2.4.2.1.1	Beta particles.....	32
2.4.2.1.2	Narrow rectangular beams.....	33
2.4.2.2	Large electron field techniques.....	33
2.4.2.2.1	Different categories in large field techniques.....	34
2.4.2.2.1.1	Scattered single beam.....	34
2.4.2.2.1.2	Pair of parallel beams.....	34
2.4.2.2.1.3	Pendulum- arc.....	35
2.4.2.2.1.4	Patient rotation.....	35
2.4.2.2.1.5	Stanford technique (rotational technique).....	36
2.4.2.2.1.5.1	Dual field angle.....	37

2.4.2.2.1.5.2	Calibration.....	38
2.4.2.2.1.5.3	In vivo dosimetry.....	40
2.4.2.2.2	Dosimetric parameters in large field technique.....	41
2.4.2.2.2.1	Field flatness.....	41
2.4.2.2.2.2	X-ray contamination.....	42
2.4.2.2.2.3	Dose distribution.....	42

CHAPTER 3

PRINCIPLES OF MONTE CARLO SIMULATION

3.1	Introduction.....	43
3.2	The ESG4 code.....	43
3.3	Random numbers generator (RNG).....	44
3.4	Electron transport.....	45
3.5	Running the EGS4 code.....	45
3.6	The BEAMnrc code.....	45
3.6.1	Introduction.....	45
3.6.2	Running the BEAM code.....	46
3.7	Efficiency and variance reduction techniques.....	47
3.8	Phase space files.....	49
3.9	BEAMDP program.....	50
3.10	DOSXYZ code	51
3.11	CT Based Phantom/ CTCREATE.....	51

CHAPTER 4

MATERIALS AND METHODS

4.1	Introduction	53
4.2	HDRE – special procedures mode	54
4.3	Experimental measurements.....	57
4.3.1	Depth dose measurements	57
4.3.2	Beam profile measurements	59
4.3.3	Multiple field measurements	60

4.3.4	Absolute measurements.....	65
4.4	Monte Carlo simulation of the Elekta Precise accelerator.....	65
4.4.1	Modeling of the radiation head of an Elekta Precise linear accelerator.....	65
4.4.2	Monte Carlo simulation of the Elekta Precise linear accelerator.....	66
4.4.2.1	First stage of simulation	68
4.4.2.2	Second stage of simulation.....	77
4.4.3	Analysis of the phase space file.....	78
4.4.4	Determining primary electron parameters.....	78
4.4.5	DOSXYZ – Calculations of dose distributions in a 3D water phantom.....	78
4.4.5.1	The construction of the water phantom model.....	79
4.4.5.2	Transport control parameters.....	80
4.4.5.3	Number of histories and uncertainty.....	81
4.5	Comparison of Monte Carlo and measured profile data.....	82
4.6	Monte Carlo simulation on Rando phantom.....	83
4.6.1	CT based simulations.....	83
4.6.2	CT Based Phantom/ CTCREATE	83
4.6.2.1	Data input.....	83
4.6.2.2	Conversion of CT number to density in CT Based Phantom/ CTCREATE	84
4.7	Comparison of measured and Monte Carlo dose distributions.....	86
4.7.1	Film registration.....	86
4.7.2	DOSXYZ dose distribution.....	86
4.7.3	The CT image.....	87
4.7.4	Normalization of the dose distribution	87

CHAPTER 5

RESULTS AND DISCUSSION

5.1	Introduction.....	88
5.2	HDRE – special procedures mode	88
5.3	Single field depth dose measurements.....	90
5.4	Single field profile measurements.....	93
5.5	Multiple field measurements	94

5.5.1	Depth doses and beam parameters.....	94
5.5.2	Ratio of <i>average skin dose</i> to <i>calibration dose</i> : The overlap factor (OV).....	98
5.6	Absolute measurements.....	99
5.7	X-ray contamination	99
5.8	Monte Carlo simulation	100
5.8.1	Simulation geometry of the Elekta Precise linear accelerator.....	100
5.8.2	Monte Carlo simulation of the Elekta Precise linear accelerator.....	101
5.8.3	Analysis of the phase space files.....	103
5.8.3.1	Electron fluence variation with position.....	103
5.8.3.2	Energy fluence variation with position.....	106
5.8.3.3	Spectral distribution	109
5.8.3.4	Angular distribution	112
5.8.4	Validation of the Monte Carlo model	114
5.8.5	Calculations of the beam data in a water phantom with the DOSXYZ code.....	115
5.8.6	Dual beam characteristics	120
5.8.7	Comparison of PDDs obtained by the Monte Carlo method and the measurements.....	122
5.8.8	Comparison of cross plane profiles obtained by the Monte Carlo method and the measurements.....	126
5.8.9	Comparison between dose distributions in a Rando phantom calculated by Monte Carlo and measured with film.	129
5.8.9.1	Percentage depth doses.....	129
5.8.9.1.1	Introduction.....	129
5.8.9.1.2	Head level.....	129
5.8.9.1.3	Thorax level.....	131
5.8.9.1.4	Navel level.....	132
5.8.9.1.4	Pelvis level	134
5.8.9.2	Isodose distributions.....	136
5.8.9.2.1	Introduction.....	136
5.8.9.2.2	Head level.....	137

5.8.9.2.3 Thorax level..... 139

5.8.9.2.4 Navel level..... 142

5.8.9.2.4 Pelvis level..... 145

5.8.9.3 Statistical uncertainty analysis..... 147

CHAPTER 6

CONCLUSION AND RECOMMENDATIONS.....148

REFERENCES.....152

SUMMARY..... 159

OPSOMMING.....161

1 INTRODUCTION

1.1 Radiotherapy

Radiotherapy or radiation treatment is defined as the treatment of diseases (mostly malignant) with ionizing radiation. The radiation may be applied as beams from the outside of the body, a process known as external beam radiotherapy, or by introducing radioactive sources into the body cavities, which is called intracavitary or intraluminal radiotherapy. Sources may be inserted into the patient's tissue to give interstitial radiotherapy. Occasionally radioactive fluids are introduced into the body either via a vein or into the cavity.

The type of treatment used depends partly on the body site requiring treatment. These types of radiotherapy treatment are practiced in most radiotherapy departments; radical radiotherapy, adjuvant radiotherapy, chemoradiotherapy, intraoperative radiotherapy and palliative radiotherapy. Radiotherapy is usually prescribed according to the intention, required for each patient (Griffiths and Short, 1994).

There are various types of ionizing radiation used in radiotherapy such as x-rays, gamma rays, electrons, neutrons, etc. Ionizing radiation is capable of damaging the genetic material (DNA) in vivo without significant deleterious effects on normal tissues. Usually, x-rays are produced in a linear accelerator by stopping fast electrons in a target material such as tungsten, or gamma rays generated in a TeleCobalt unit. Radiation can cure or control cancer by damaging the cancer cells so they cannot divide or reproduce. About fifty to sixty percent of patients with cancer will require radiation at some time or other during the course of their disease. Radiation is a safe and effective form of treatment for patients of all ages (Rath, 2000). Radiotherapy combined with surgical and medical disciplines improve treatment outcome better than surgery or radiotherapy alone. The radiotherapy specialty was born immediately after the discovery of Röntgen rays or x-rays by Wilhelm Conrad Röntgen in the year 1895. The first generations of low energy x-ray generators were very inefficient in penetrating deep-seated tumours. Subsequently

the discovery of radium in 1898 by Marie Curie gave birth to the specialty brachytherapy. It was the discoverer of the telephone, Alexander Graham Bell, who proposed the concept of using a radium source inside the tumour.

Following 1945, from the experience of radar systems, the concept of the linear accelerator evolved. More and more refined x-ray generators (Van de Graaff generator and linear accelerators) have developed afterwards to make radiation more penetrating than the previously available low energy x-ray generators. Artificially prepared radionuclides such as cobalt-60 (^{60}Co) and Caesium-137 (^{137}Cs) have been in use as sources of radiation in the past seven decades.

In the past, the understanding about radiation safety was not clear. People used radiation casually to treat patients with cancers and non-cancerous conditions. Radiation sources were used widely over several years for brachytherapy purposes until the introduction of radiation safety principles in the 1950s. From the experiences of radiation hazards, afterloading systems for brachytherapy evolved, making radiation therapy safer without the risk of exposure to the medical personnel. With growing technology and better understanding of radiation biology, radiotherapy achieved many milestones at a faster rate. Since the early 1990s, radiation oncology has increasingly become technology oriented. This has resulted in accurate target localization and precise delivery of radiation to the target area resulting in better tumour control, minimal normal tissue complications and to some extent improved survival rates (Rath, 2000).

Now radiation therapy plays an important role in cancer management. Today about 45 percent of all cancer patients can be cured, about one half of them are cured by radiation therapy applied alone or in combination with surgery or chemotherapy (Wambersie and Gahbauer, 1995). The clinical experience accumulated in decades shows that, to be efficient, the radiation treatment must be delivered with a high physical selectivity. At present, electron linear accelerators are the primary equipment of a modern radiotherapy department, and are used to irradiate a large proportion of the patients for at least part of the treatment. Photon beams of about 6-20 MV have in general a sufficient penetration in

the tissues to treat most of the tumours with an adequate physical selectivity. A combination of several beams adequately oriented allows the radiation-oncologist to deliver the prescribed dose to the "target volume" (tumour) without exceeding the tolerance of the surrounding normal tissues. Conformal therapy, which needs well-equipped and well-staffed centers, further improves the physical selectivity of the treatment, and offers definitive advantages at least for some tumour types and/or locations. Finally, modern linear accelerators are used to maximize accuracy in dose delivery to obtain better therapeutic results in radiotherapy (Wambersie and Gahbauer, 1995), to deliver a high dose to a target volume (tumour) and spare as much as possible the normal surrounding tissue.

In general the radiotherapy aims to deliver enough radiation to the tumour to destroy it without irradiating normal tissue to a dose that will lead to serious complications (morbidity) (Rath, 2000). Study has shown that the dose-response curve is quite steep and there is evidence that a 7 to 10 % variation in the dose to the target volume may result in a significant change in both the tumour control and normal tissue complication probabilities (Kutcher, 1992).

Radiation therapy demands more accurate dosimetry for good patient care (Metcalfe et al, 1997). The demand has increased tremendously with the advent of computer technology like CT scanners, which allow detailed knowledge of the geometry and densities of the body to be irradiated (Ma et al, 1999). Taking into consideration the steepness of the dose response curve as mentioned above, methods that can be employed for the accurate determination of absorbed dose distributions in the patient have a big role to play (Awusi, 2000, Metcalfe et al, 1997). In fact Monte Carlo simulation is fast becoming the next generation of dose calculation engine for radiation treatment planning systems in routine clinical practice (Mohan, 1997 and Ma and Jiang, 1999).

1.2 Types of radiotherapy treatment

1.2.1 Radical radiotherapy

Radical radiotherapy is used in early stages of cancers for curative purposes. The radiation oncologist takes a lot of time to accurately delineate the tumour volume, analyze image data, simulate, perform dosimetric analysis of a plan and actual radiation dose delivery. It usually takes about 6-8 weeks to complete a course in multiple sequential phases called the shrinking field technique. Some common tumours treated by radical radiotherapy are cancers of the larynx, nasopharynx, uterine cervix, skin, bladder, breast, and prostate. Radical radiotherapy involves multiple hospital visits, a prolonged course of treatment up to normal tissue tolerance, and the patient has to expect and accept some degree of acute and chronic side effects (Griffiths and Short, 1994).

1.2.2 Adjuvant radiotherapy

The word adjuvant is derived from the Latin verb 'adjuvere' meaning 'to help'. In situations where radiotherapy is utilized for the improvement of the results of another modality (usually surgery) it is called adjuvant radiotherapy. Radiotherapy can be delivered before surgery (preoperative radiotherapy), after surgery (postoperative radiotherapy), during surgery (intraoperative radiotherapy) and as a combination of preoperative and postoperative radiotherapy (sandwich radiotherapy). When radiation therapy is administered during surgery, the microscopic and minimal macroscopic disease in the tumour bed get sterilized and thereby local control and ultimately survival is improved. The commonly encountered cancers requiring adjuvant radiotherapy are rectal cancers, head and neck cancers, breast cancers, and brain tumours (Mohan B B, 1999). Radiotherapy is however, most frequently used postoperatively.

Surgeons find difficulty in excising an infiltrating tumour, because their excision may not be pathologically complete. They are likely to leave residual disease, or spill tumour to the adjacent areas during handling of the tumour. In this situation radiotherapy frequently helps surgeons to circumscribe the tumour and overcome the above difficulties.

Radiotherapy treatment has a higher failure rate at the tumour center which contains radioresistant tumour clonogens. In contrast, radiotherapy is efficient in the eradication of a small number of well vascularized tumour cells at the resection margin. Hence combination of radiotherapy and surgery sounds logical. The best example of postoperative radiotherapy is demonstrated in stage-I seminoma of the testis. By giving prophylactic postoperative radiotherapy, the relapse rate reduces from 15% to near zero percent. The other example is in post excision breast cancer. In this situation the breast relapse rate reduces from 35% to less than 10% after postoperative radiotherapy (Mohan B B, 1999).

1.2.3 Chemoradiotherapy

Sometimes anti-neoplastic drugs when given in conjunction with radiotherapy, enhance the efficiency of radiation. When radiation is given concurrently with chemotherapy the cancer cell kill increases by two fold. These principles are used in the organ preservation techniques in anal canal cancer, bladder cancer, esophageal cancer and cervical cancers (Mohan B B, 1999).

1.2.4 Intraoperative radiotherapy

Radiation can be delivered during operation resulting in sterilization of the malignant cells in the tumour bed. The irradiation of the tumour using this technique is superior to percutaneous external beam radiotherapy in multiple doses. Sometimes, electron beam irradiation and interstitial brachytherapy are used to improve local control. This principle of radiotherapy is used in soft tissue sarcoma, pancreatic cancers, stomach cancer and retroperitoneal sarcomas (Mohan B B, 1999).

1.2.5 Palliative radiotherapy

In very advanced cancers, there are poorly defined generalized symptoms which are difficult to manage. In this situation, cure is not possible and the concern is with the issues of quality of life. The aim is therefore the minimization of discomfort, called palliative treatment. This form of therapy should be simple, should not produce

morbidity, and improve quality of life without necessarily prolongation of life expectancy. Palliation can involve some of the following: surgical diversion procedure, nerve block, analgesic medication, transcutaneous electrical nerve stimulation and radiotherapy. Chemotherapy is rarely utilized for palliation in chemosensitive tumours (Griffiths and Short, 1994).

The total skin electron therapy technique can be used for radical, palliative cases as well as adjuvant radiotherapy.

1.3 Electron beam radiotherapy

The features of the electron beams that make it a unique therapeutic tool are related to physical characteristics rather than to any special biological effectiveness of the electrons. The most attractive characteristic in radiotherapy is the shape of the depth dose curve. The curve displays a moderately flat plateau in the first few centimeters of tissue, followed by a rapid fall in the absorbed dose to a small "tail" produced by x-ray. With high energy electrons the fall in depth dose after the initial plateau, is less steep. The advantage to be drawn from the depth dose pattern are, therefore, greatest at low energies, making the use of electrons for irradiation of sub-dermal tumour with the benefit of sparing the underlying tissues.

The characteristics which are of particular significance in clinical applications are:

- (i) The dose distribution from a single beam is such as to allow the treatment of the surface slab of tissue to relatively uniform doses whilst sparing underlying, deeper regions of healthy tissues.
- (ii) The depth dose curve with electrons of lower energy offer rapid and simple treatment set-up, with the use of one field in many cases.
- (iv) There is no difference in biological effectiveness of electrons compared with megavoltage photon radiation.
- (v) The build-up of absorbed dose below the skin is rapid: thus the skin sparing effect is smaller than with high energy photons.

(vi) The dose distribution in tissue suffers perturbation if tissue inhomogeneities are presents with in the beam.

The principal applications of electrons are in (ICRU report 42, 1987):

- (i) The treatment of skin cancers.
- (ii) Chest wall irradiation for breast cancers.
- (iii) The treatment of head and neck cancers.

Although many of these sites can be treated with superficial x-rays, irradiation using electron beam offers distinct advantages in terms of uniformity of the dose in the target volume and in minimizing dose to deep seated tumours (Mohan, 1999).

1.4 Electron therapy treatment planning

The complexity of electron-tissue interactions does not make electron beams well suited to conventional treatment planning algorithms, because of their difficulty in modelling and predicting the dose for oblique incidence or tissue interfaces.

The early methods of electron dose distribution calculations were empirical and based on water phantom measurements of percentage depth doses and beam profiles for various field sizes, similar to the Milan and Bentley method developed in the late 1960s for use in photon beams (ICRU report 35, 1984). Inhomogeneities were accounted for by scaling the depth dose curves using the Coefficient of Equivalent Thicknesses (*CET*) technique (Khan, 2003). This technique provides useful parametrization of the electron depth dose curve but has nothing to do with the physics of electron transport that is dominated by the theory of multiple scattering. The Fermi-Eyges multiple scattering theory (Jette, 1983) considers a broad electron beam as being made up of many individual pencil beams which spread out laterally in tissue, approximately as a Gaussian function with the amount of spread increasing with depth. The dose at a particular point in tissue is calculated by an addition of contributions of spreading pencil beams. This algorithm can account for tissue inhomogeneities, patient curvature and irregular field shape. Rudimentary pencil beam algorithms dealt with lateral dispersion, but ignored angular dispersion and back scattering from tissue interfaces. Subsequent analytically advanced

algorithms refined the multiple scattering theory through applying both the stopping powers as well as the scattering powers but nevertheless generally failed to provide accurate dose distributions in general clinical conditions.

The most accurate way to calculate electron beam dose distributions is through Monte Carlo techniques. The main drawback of the current Monte Carlo approach as a routine dose calculation engine is its relatively long calculation time. However, with the ever-increasing computer speed combined with the decreasing hardware cost, one can expect that in the near future Monte Carlo-based electron dose calculation algorithms will become available for routine clinical applications (Podgorsak, 2004).

1.5 Monte Carlo simulation techniques

Monte Carlo (MC) simulation is one of the most accurate methods available at the moment for obtaining the dose distribution due to a radiation beam. The method can precisely model the physical processes involved in radiation therapy and is powerful in dealing with any complex geometry (Ma et al, 1999 and Johns and Cunningham, 1982). The MC method is a statistical simulation method (Bushberg et al, 1994). It simulates the tracks of individual particles by sampling appropriate quantities from the probability distribution governing the individual physical processes using machine-generated random numbers. By simulating large number of histories, information can be obtained about average value of macroscopic quantities such as energy deposition. Moreover, since one follows individual particle histories, the technique can be used to obtain information about the statistical fluctuation of particular kinds of events. It is also possible to use Monte Carlo to answer questions which cannot be addressed by experimental investigation, such as “what fraction of these electrons were generated in the collimator versus the filter” or “how often have certain photons undergone Compton scattering”.

MC method consists of computer simulations that involve transport of a photon, or electron beams through a medium and calculating the deposition of energy within the phantom by using the laws of probability and the known physical characteristics (Nahum,

1988). The transport of an incident particle, and of the particles that it subsequently sets in motion, is referred to as a particle history and in MC each history is uniquely followed by random selection from the probability distribution that control each possible interaction (Metcalf et al, 1997). The histories of a very large number of individual photons or electrons as they interact, scatter and eventually disappear are tracked (Rogers, 2002). Because the MC method requires modeling a stochastic set of events, the computer essentially rolls the dice to determine how each particles interacts and what the fate of that particle will be after the interaction (Nelson, 1988, Mohan, 1988).

In contrast, MC simulation of photon transport is much faster compared to electron transport (Nahum, 1988). Photons on average undergo a moderate number (tens) of interactions and also the cross-section data needed for most applications are known to a high degree of accuracy (Andreo, 1991). While the electron transport it is time-consuming to simulate each interaction individually because an electron undergoes a large number (thousands) of elastic scattering from nuclei during its history (Rogers et al, 1990). Moreover in the photon simulations, the electron transport consumes most of the computing time for high energies where the electron range is large (Mackie, 1990). This is because there are usually many short electron transport steps corresponding to each photon step (Awusi, 2000). Therefore the simulation of electron requires a different approach involving a combination of multiple scattering and stopping power theories. Berger, 1963 first introduced the condensed history technique in which electron histories were “condensed” into a series of steps in which the effects of many scattering events were considered at once and a multiple scattering theory used to account for the elastic and inelastic scattering during this step (Rogers et al, 1990).

1.5.1 Advantages of Monte Carlo simulation

The main advantages the Monte Carlo method for the calculations of the dose distributions in a patient (Rogers 1991; Ma and Jiang, 1999; Andreo, 1991; Metcalfe et al, 1997), are:

- (a) Monte Carlo method can be accurately model the physics of radiation therapy transport and can be applied to any absorbing medium, geometry and radiation beam.
- (b) Electrons and positrons produced in case of photon interactions can also be tracked.
- (c) Information about macroscopic quantities such as particle fluence can be obtained.
- (d) The method can be used to obtain the information that cannot be measured experimentally.
- (e) The Monte Carlo methods can handle backscatter from high-density materials such as bone and scatter perturbations by air cavities more accurately than any other existing dose calculation model (Rogers and Bielajew 1990).
- (f) The method can be predicate some of the experimental investigation, such as what fraction of the electrons was generated in the collimator versus the filter, or how often have certain photons undergone Compton scattering.
- (g) The Monte Carlo can provide information such as fluence, energy fluence, energy spectra and angular distributions of the radiation beam which is almost difficult to measure.
- (h) The Monte Carlo method allows the generation of the energy spectrum, not only in the central part of the beam, but also in regions away from it.
- (i) Using Monte method it possible saving in manpower at the expense of computer time.

Monte Carlo simulation is therefore the method of choice for solving complicated recitation transport problems (Williamson, 1989).

1.5.2 Limitations of Monte Carlo simulation

- (a) The method required a large number of histories to achieve adequate statistical uncertainty in the distribution. The lower the uncertainty the smoother the depth dose or cross beam profiles obtained from the distributions (Metcalf et al, 1997).
- (b) Due to a large number of histories are simulated in the method, a large amount of computer memory and long computing times are required.

The Monte Carlo method at the present is only used for simulation as a benchmark to compare other simpler and faster calculation methods. The major shortcoming of the

Monte Carlo method, namely being computationally intensive, has become much less severe due to the rapid increase in speed and decrease in cost of computers, and the employment of innovative variance reduction techniques. A parentally the OMEGA project has been under the development of MC based three dimensional (3D) treatment planning systems (TPSs) (Rogers et al, 1995). Hopefully with these new developments the dose to be delivered to a patient will be calculated in a few minutes.

1.6 Monte Carlo simulation of linear accelerator head

There are several simulation codes available which can be used to simulate therapy units. Examples are:

- 1) The MCNP (Monte Carlo N-Particle) code system (Lewis et al, 1999).
- 2) The VMC (Voxel Monte Carlo) code system (Kawrakow et al, 1996).
- 3) The GEANT (Geometry And Tracking) code system (Beaulieu et al., 2003).
- 4) The ETRAN (Electron Transport) code system (Berger and Seltzer, 1988).
- 5) The ITS (Integrated Tiger Series) code system (Halbleib and Melhorn, 1992).
- 6) The EGS4 (Electron Gamma Shower) code system (Rogers et al, 2005).
- 7) The FLUKA (FLUktuierende KAskade) code system (Ferrari et al, 2005).

In all of the above simulation codes, the EGS4 code, is the most widely used MC code in medical radiation physics. The EGS4 code is written in MORTRAN language, which is based on FORTRAN, but has extensions to make it more flexible and easier to use (Metcalf et al, 1997).

MC simulations of the radiation beam output for radiation treatment machine head, offer a practical means for obtaining energy spectrum and angular distribution of the photon and electron beam, which are important in radiation dosimetry (Nahum, 1988). The user has to set up the problem geometry, which includes arrangement and description of the various relevant components of the head, in a manner that can be understood by the computer program (Awusi, 2000). One of particular advantage of the BEAM code is the way it was designed and simplified in such a way that it can be accurately used to

simulate treatment heads by other individuals with minimum effort (Rogers et al, 2005). The other advantage of the BEAM code is that the generated phase space files can be re-used by the BEAM itself, allowing the user to simulate a treatment head output in separate steps to reduce CPU time.

In this study the Monte Carlo simulation codes, were used to simulate the 4 and 6 MeV electron beams from an Elekta Precise linear accelerator and to calculate the dose distribution in a phantom. The BEAMDP code was used for the analysis of the phase space files (PSF), as well as the CT based Phantom/CTCREATE program was used in the simulation of CT based models.

1.7 Aim of the study

The aim of this study was to commission and optimize a high-dose rate electron (HDRE) facility on an Elekta Precise linear accelerator for a Total Skin Electron Therapy (TSET) technique.

1.8 Specific objectives

The specific objectives required to achieve the above aim are as follows:

- (a) Measurements of reference beam data for the 4 and 6 MeV electron beams in high dose rate mode in a water phantom at isocentre (100 cm SSD).
- (b) Measurements of reference beam data for the 4 and 6 MeV electron beams in high dose rate mode at the position of the treatment plane (350 cm SSD).
- (c) Monte Carlo simulation of the Elekta Precise linear accelerator using the BEAM code to obtain phase space files at the isocentre for the 4 and 6 MeV electron beams.
- (d) Simulation of beam data in a water phantom using the phase space files and the DOSXYZ code and comparing the results to the measured reference data at isocentre, so that Monte Carlo simulation parameters can be optimized.
- (e) Simulation of beam data at the treatment plane distance and comparing the results with the measured reference data to validate the simulation parameters.

- (f) Simulation of a multiple beam treatment on a Rando phantom and comparing the results with film measurements to verify the accuracy of the simulation.
- (g) Optimizing the treatment parameters by simulation of alternative treatment set-ups.

2 BASIC PHYSICS OF RADIOTHERAPY

2.1 Medical linear accelerator

2.1.1 Introduction

The electron linear accelerator (linac) was developed at early 1950s by several different research groups (Metcalf et al, 1997). The basic design of these machines is similar to a heavy-ion accelerator. The linac uses high frequency electromagnetic waves to accelerate charged particles such as electrons to high energies through a linear tube. There are several types of linear accelerator designs but the ones used in radiotherapy accelerate electrons either by traveling or stationary electromagnetic wave of a frequency 3 GHz, giving a wavelength = 10 cm in a vacuum (Khan, 2003).

2.1.2 Principles of operation

Figure 2.1 is a block diagram of a medical linear accelerator showing major components and auxiliary components. A power supply provides DC power to the modulator that includes the pulse forming network and a switch tube known as hydrogen thyatron. High voltage pulses from the modulator section are flat-topped DC pulses of a few microseconds in duration (Khan, 2003). These pulses are delivered to the magnetron or klystron and simultaneously to the electron gun. Pulsed microwaves produced in the magnetron or klystron are injected into the accelerator tube or structure via a wave guide system. At the proper instant electrons, produced from the electron gun are also pulse injected into the accelerator structure. The accelerator structure consists of an evacuated copper tube with its interior divided by copper discs or diaphragms of varying aperture and spacing (Khan, 2003, Metcalf et al, 1997, Johns and Cunningham, 1983). As the electrons are injected into the accelerator structure with an initial energy of about 50 KeV, the electrons interact with the electromagnetic field of the microwaves. And the electrons gain energy from the sinusoidal electric field (Johns and Cunningham, 1983).

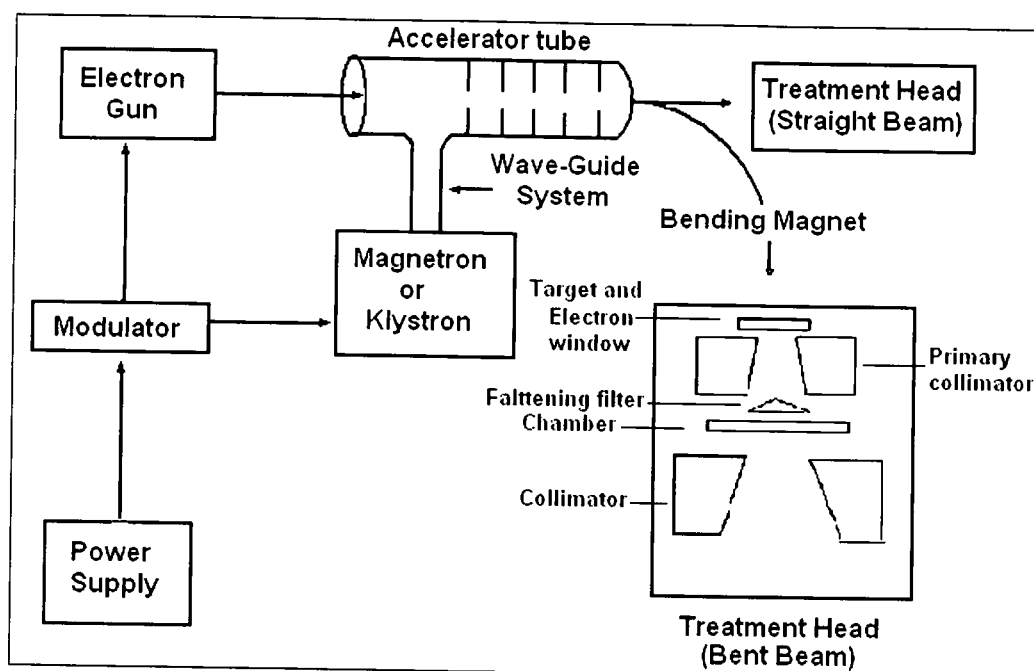


Figure 2.1: A block diagram of typical medical Linear Accelerator (adapted from Khan, 2003).

As the High-energy electrons emerge from the exit window of the accelerator structure, they are in the form of a pencil beam of about 3 mm in diameter. In the low energy linear accelerators (up to 6 MeV) have relatively short accelerator tubes, the electrons are allowed to proceed straight on to strike a target for X-ray production (Khan, 2003). In the higher-energy linear accelerators, the accelerator structure is too long and, therefore, is placed horizontally or at an angle with respect to horizontal. The electrons are bent through an angle (usually about 90° or 270°) between the accelerator structure and the target using bending magnets, focusing coils and other components such that the beam emerges facing down wards (Khan, 2003, Johns and Cunningham, 1983).

2.1.3 The Linac photon and electron beam

In the photon beam, after the accelerate of the electron beam to relativistic velocities within the linear accelerator wave guide they strike a target and photons with a broad energy spectrum forward peaked fluence are emitted due to bremsstrahlung production (Khan, 2003). X-rays are produced when high energy electrons are incident on a target of

a high Z material such as tungsten. The target is thick enough to absorb most of the incident electrons and as a result the electron energy is converted into a spectrum of X-ray energies (Johns and Cunningham, 1983). In the electron mode of an accelerator, this beam, instead of striking the target, is made to strike an electron scattering foil (usually of lead) in order to spread the beam as well as get a uniform electron fluence across the treatment field (Khan, 2003).

2.1.4 Beam collimation and monitoring

The treatment beam is first collimated by a fixed primary collimator located immediately below the X-ray target. In case of X-rays the collimated beam then passes through the flattening filter whose main function is to modify the forward peaked X-ray beam to a uniform beam and to filter the low energy X-ray spectrum (Khan, 2003). In the electron mode the flattening filter is moved away and replaced by a scattering foil whose main function is to spread the electron beam (Khan, 2003, Metcalfe et al, 1997). The flattened X-ray beam or the electron beam is incident on the dose monitoring chambers, whose main functions are to monitor dose rate, integrated dose and field symmetry. After passing through the ion chamber, the X-ray beam is further collimated by a continuously movable collimator consisting of two pairs of lead or tungsten block jaws that provide a rectangular opening. For electron beams an applicator of appropriate size is used. The field size localizer is provided by a light source system in the treatment head (located between the ion chamber and the jaws) which is a combination of a mirror and a light source (Khan, 2003, Johns and Cunningham, 1983).

2.2 Photon interaction processes

Attenuation of a photon beam by an absorbing material is caused by four interactions describe photon absorption in tissue: the photoelectric effect, Compton effect, pair production and coherent scattering.

2.2.1 Photoelectric Effect

The photoelectric effect is a phenomena in which a photon interacts with an atom and ejects one of the orbital electrons from the atom. In this process the entire energy, $h\nu$, of the photon is transferred to the atomic electron. The kinetic energy of the ejected electron (called the photoelectron) is equal to $h\nu - E_B$, E_B is the binding energy of the electron. Interactions of this type can take place with electrons in the K, L, M, or N shells. Figure 2.2. shows the the Photoelectric effect phenomena.

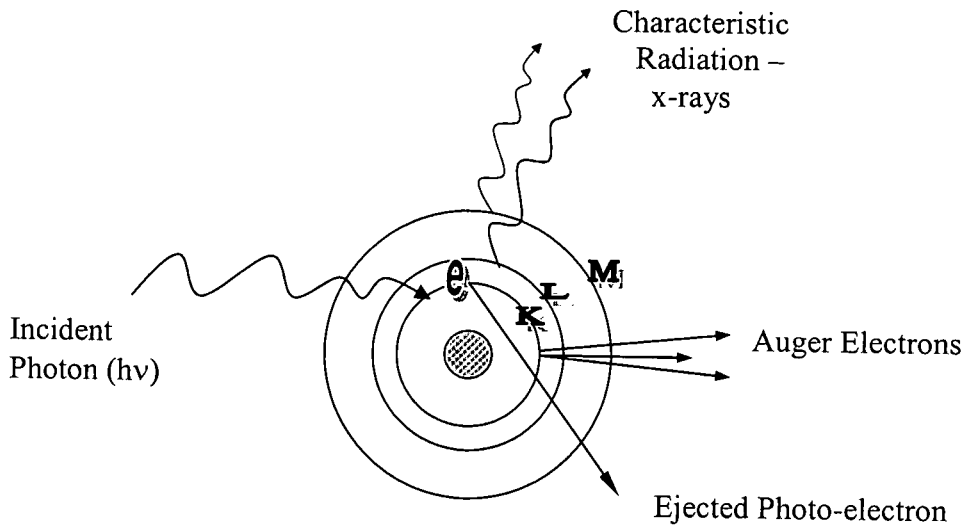


Figure 2.2: illustrating the Photoelectric effect (adapted from Khan, 2003).

2.2.2 Compton Effect (Incoherent)

The Compton process, the photon interacts with an atomic electron as though were a “free” electron. The term “free” here means that the binding energy of the electrons is much less than the energy of the bombarding photon. In this interaction, the electrons receives some energy from the photon and is emitted at angle θ . The photon, with $= h\nu_0$ reduced energy, is scattered at an angle ϕ (see figure 2.3).

The Compton process can be analyzed in terms of a collision between two particles, a photon and electron. By applying the laws of conservation of energy and momentum, one can derive the following relationship.

$$E = h\nu_0 \frac{\alpha(1 + \cos \phi)}{1 + \alpha(1 - \cos \phi)} \quad 2.1$$

$$h\nu' = h\nu_0 \frac{1}{1 + \alpha(1 - \cos \phi)} \quad 2.2$$

$$\cot \theta = (1 + \alpha) \tan \phi / 2 \quad 2.3$$

Where, $h\nu_0$, $h\nu'$, and E are the energies of the incident photon, scattered photon, and electrons, respectively and $\alpha = h\nu_0 / m_0c^2$, where m_0c^2 is the rest energy of the electron (0.511 MeV). If $h\nu_0$ is expressed in MeV, then $\alpha = h\nu_0 / 0.511$.

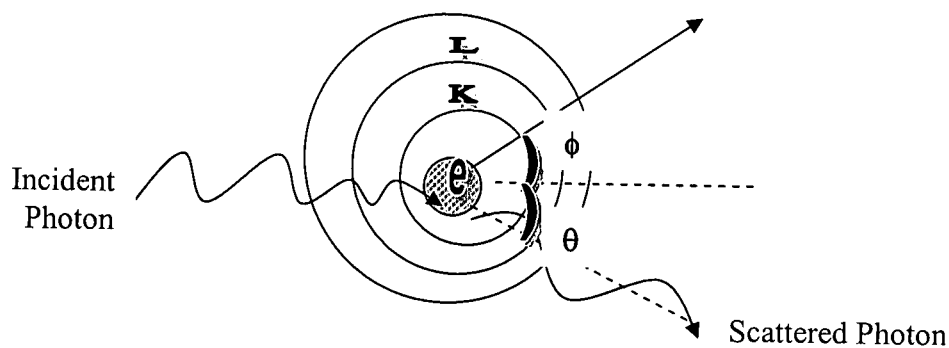


Figure 2.3: illustrates the Compton process (adapted from Khan, 2003).

2.2.3 Pair production

In this process, a photon interacts with the nucleus of an atom, not an orbital electron. The photon gives up its energy to the nucleus and, in the process, creates a pair of positively and negatively charged electrons. The positive electron (positron) ionizes until it combines with a free electron. This generates two photons that scatter in opposite directions. The probability of pair production is proportional to the logarithm of the energy of the incoming photon and is dependent on the atomic number of the material. The energy range in which pair production dominates is ≥ 25 MeV. This interaction does occur to some extent in routine radiation treatment with high-energy photon beams. Figure 4.5. shows the Pair Production process.

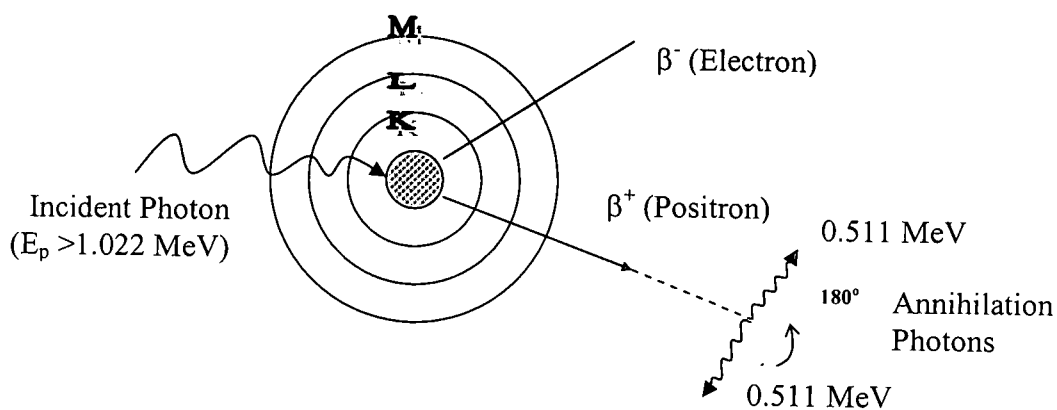


Figure 2.4: illustrates the Pair Production process (adapted from Khan, 2003).

2.2.4 Coherent scattering

The coherent scattering, known as known as classical scattering or Rayleigh scattering, is illustrated in figure 2.5. The process can be visualized by considering the wave nature of electromagnetic radiation. This interaction consists of an electromagnetic wave passing near the electron and setting in into oscillation. The oscillating electron re-radiates the energy at the same frequency an incident electromagnetic wave. The scattered X-rays have the same wave length as the incident beam. Thus no energy is transferred and no energy is absorbed in the medium. Coherent scattering is probable in high atomic number materials and with photons of low energy.

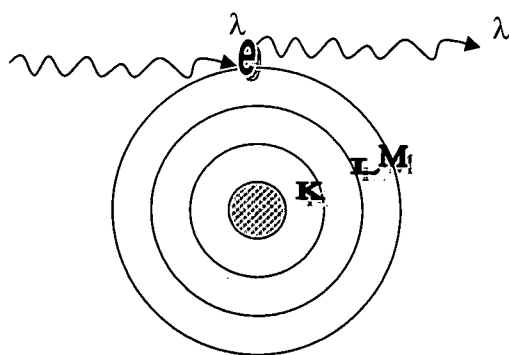


Figure 2.5: illustrates the Coherent scattering process (adapted from Khan, 2003).

2.3 Electron interaction processes

As an energetic electron traverses matter, it interacts with the matter through Coulomb interactions with atomic orbital electrons and atomic nuclei. Through these collisions the electrons may lose their kinetic energy (collision and radiative losses) or change their direction of travel (scattering). Energy losses are described by stopping power; scattering is described by scattering power. The collisions between the incident electron and an orbital electron or nucleus of an atom may be elastic or inelastic. In an elastic collision the electron is deflected from its original path but no energy loss occurs, while in an inelastic collision the electron is deflected from its original path and some of its energy is transferred to an orbital electron or emitted in the form of bremsstrahlung (Podgorsak, 2004).

Energetic electrons experience thousands of collisions as they traverse an absorber; hence their behavior is described by a statistical theory of multiple scattering embracing the individual elastic and inelastic collisions with orbital electrons and nuclei.

2.3.1 Collisional energy loss

Collisional energy loss occurs when a secondary electron passes close enough to an atomic electron to eject it from its shell either permanently or temporarily.

Collisional energy losses in which the electron loses a small amount of energy are very frequent. The rate of energy loss by this mechanism depends on the electron energy, the number of the atomic electrons per unit volume, and slightly on the ionization energy of the atoms in the medium (Metcalf et al, 1997). Less frequently, large energy losses occur when a much higher portion of electron energy is transferred to an orbital electron. The ejected electron is known as a δ ray, which itself causes ionization and excitation. Such collisions are called Möller scattering events (Ali, 2001).

2.3.2 Radiative energy loss (bremsstrahlung production)

In these types of energy losses, Coulomb interactions between the incident electron and nuclei of the absorber atom result in electron scattering and energy loss of the electron through production of X-ray photons (bremsstrahlung). Figure 2.6 illustrates the mechanism of the bremsstrahlung production.

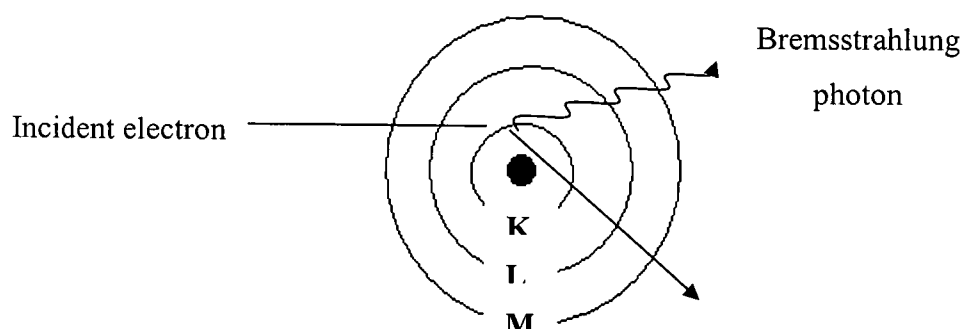


Figure 2.6: This figure shows Bremsstrahlung emitted when an electron interacts with the coulomb field of the nucleus. The electron continues with its energy reduced (adapted from Metcalfe et al, 1997).

The probability of this interaction increases as the distance of the electron from the nucleus is decreased. The energy of the Bremsstrahlung photon cannot be larger than the incident electron energy (Metcalfe et al, 1997).

2.3.3 Electron stopping powers

Stopping powers are widely used in radiation dosimetry, but they are rarely measured and have to be calculated from theory. The linear stopping power is defined as the expectation value of the rate of energy loss per unit path length, dE/dZ of the charged particle. Stopping power can be divided into collisional stopping power and radiative stopping power. When the stopping power is divided by the density the ratios are called the mass collisional stopping power and mass radiative stopping power. The total mass stopping power has units of $\text{MeV cm}^{-2} \text{g}^{-1}$. The total mass stopping power is given by (ICRU Report 37, 1984):

$$\left(\frac{S}{\rho}\right)_{tot} = \left(\frac{S}{\rho}\right)_{col} + \left(\frac{S}{\rho}\right)_{rad} \quad 2.4$$

2.3.3.1 Mass collision stopping power

The mass collision stopping power is $\left(\frac{S}{\rho}\right)_{col}$ resulting from electron-orbital electron interactions (atomic excitations and ionizations). The mass collision stopping power can be given by the formula:

$$\left(\frac{S}{\rho}\right)_{col} = \frac{N_A Z}{Z} \frac{\pi r_e^2 4 m_e c^2}{\beta^2} Z^2 \left[\ln \left(\frac{(2 m_e v^2)}{2(I)} \right) - \ln(1 - \beta^2) - \beta^2 \right] \quad 2.5$$

where;

β is the velocity of the electron relative to the speed of light c .

r_e is the classical electron radius

Z is the projectile charge in units of electron charge

I is the mean excitation energy.

2.3.3.2 Mass radiative stopping power

The mass radiative stopping power is the rate of energy loss by electrons that results in production of bremsstrahlung. The radiative stopping power increases with higher atomic number and higher energy. The radiative stopping power is given by the following formula (Metcalf et al, 1997):

$$\left(\frac{S}{\rho}\right)_{rad} = \frac{4 N_A Z(Z-1)}{A} r_0^2 E \frac{183}{Z^{1/3}} \quad 2.6$$

where E is the energy,

A very approximate expression of the ratio of radiative to collision stopping power is given by the following formula,

$$\frac{S_{rad}}{S_{col}} = \frac{E(Z + 1.2)}{800} \quad 2.7$$

The equation predicts that the two stopping powers will be equal when the energy is approximately equal to $800/Z$ MeV.

2.3.4 Restricted stopping power

In radiation dosimetry the concept of restricted stopping power $\left(\frac{L}{\rho}\right)$ is introduced which accounts for that fraction of the collisional stopping power $\left(\frac{S}{\rho}\right)_{col}$ that includes all the soft collisions (in which only a small amount of the incident particle energy is transferred to the secondary particles, in the form of excitation energy) plus those hard collisions (in which a large fraction of the incident particle energy is transferred to a secondary electron causing what is called a “delta ray”), which result in delta rays with energies less than a cut-off value Δ .

The restricted stopping power (also referred to as a linear energy transfer) L_{Δ} of a material, for charged particles, is the quotient of dE_{Δ} by dL , where dE_{Δ} is the energy lost by charged particles due to collision in traversing a distance dL minus the total kinetic energy of charged particles released with kinetic energy in excess of Δ :

$$L_{\Delta} = \frac{dE_{\Delta}}{d\ell} \quad 2.8$$

The restricted stopping power is the restricted linear collision stopping power divided by the density of the material.

2.3.5 Range concept (CSDA)

A charged particle such as an electron is surrounded by its Coulomb electric field and will therefore interact with one or more electrons or with the nucleus of practically every atom it encounters. Most of these interactions individually transfer only minute fractions

of the incident particle's kinetic energy and it is convenient to think of the particle as losing its kinetic energy gradually and continuously in a process often referred to as the continuous slowing down approximation (CSDA).

The CSDA range (or the mean path-length) for an electron of initial kinetic energy E_0 can be found by integrating the reciprocal of the total stopping power:

$$R_{csda} = \int_0^{E_0} \left(\frac{S(E)}{\rho} \right)^{-1}_{tot} dE. \quad 2.9$$

Where, E_0 is the starting energy of the particle.

The CSDA range thus represents the mean path-length and not the depth of penetration in a defined direction.

2.4 Radiation dosimetry

This thesis considers the dosimetry of a Total Skin Electron Therapy (TSET) technique. It is therefore appropriate, before we proceed any further, to define radiation “dose”. The absorbed dose, D is defined as energy absorbed in a medium per unit mass or (Johns and Cunningham, 1983 1983).

$$D = \frac{dE_{ab}}{dm} \quad 2.10$$

The dose can also be derived from a particle fluence. The fluence, Φ , is defined as the number of particles crossing a surface of unit area perpendicular to the direction of motion. The energy fluence, Ψ , is sometimes used and this is the total energy passing through a surface of unit area.

Differential fluence, $\Phi_{E,U}$, is an element of fluence possessing an energy, E , and a trajectory, U . Often it is sensible to separate a fluence into such components. When we examine a beam spectrum or the in-air distribution of a point source, we are referring to a differential fluence.

When a particle interacts with the medium, it does so with probability per unit length, μ , and $\frac{1}{\mu}$ is the mean free path between interactions. If $\bar{E}_{a,b}$ is the mean energy absorbed by the medium, then the absorbed dose is defined as:

$$D = \Phi \left(\frac{\mu}{\rho} \right) \bar{E}_{a,b} \quad 2.11$$

Dose can also be calculated from the divergence of the vectorial energy fluence, Ψ , (Rossi and Roesch, 1962), and this is the manner in which the fluence transport equation is used to generate analytic models of dose distribution.

$$D(x) = - \frac{1}{\rho(x)} \nabla \cdot \Psi \quad 2.12$$

2.5 Total skin electron therapy

Skin cancer is rarely a fatal disease (a notable exception being melanoma). The majority of lesions grow slowly and 90 per cent of the lesions arise in exposed areas. They are usually diagnosed in an early stage of development. These tumours are often readily curable and therefore the selection of the optimum treatment modality should be considered with respect to the expected effects, the relative comfort, time and cost of treatment of the patient, as well as upon the probability of cure. Curability of the common skin tumours by competent surgery is not questioned by reasonable radiation therapists nor should it be challenged (Walter, 1967).

Radiation therapy has a special role in the palliation of the widespread cutaneous lymphomas and some multicentric diseases such as Kaposi sarcoma. Some tumours are radioresistant or are located in sites that tolerate irradiation poorly. These include the position of the extremities. Ionizing radiation is preferred as it has a high probability of eradicating the lesion and preserving normal tissues. All this can be achieved with minimal time and cost to the patient. This demands a good clinical knowledge of anatomical factors, radiobiology, and a judicious computation of all the physical factors in radiation therapy, including treatment volume, quality of irradiation, dosage, overall treatment time and fractionation (Walter, 1967).

Malignant skin diseases, such as mycosis fungoides and cutaneous lymphomas (Lo TCM, et al 1979, Richard, 2003), are often treated with nitrogen mustard and Photo Ultra Violet type-A (PUVA), but the most effective treatment is Total Skin Electron Therapy or TSET (Richard, 1997). TSET (AAPM, 1988) is an external beam therapy. It is a complex technique for which special irradiation and dosimetry conditions have been studied based on the particular methods implemented (AAPM, 1988). Technical challenges in setting up a TSET program arise primarily from the unusual target volume of the disease that often includes the whole-body skin surface extending to a depth of about 5 mm. Because of the shallow depth of the disease, low-energy electrons that have a limited penetration are the favoured choice of radiation source. The goal is then to deliver a relatively uniform dose (e.g., $\pm 10\%$) to the skin of the entire body amid the ever-changing curvature of the body surface and the unavoidable self-shielding among the body structures. In addition, the X-ray contamination, produced by the inevitable interactions of the electrons with materials in the beam path, has to be kept low to prevent serious radiotoxicity arising from whole-body X-ray exposure (Chen et al, 2004). A high dose rate is required in order to treat the patient at 3 to 4 meters SSD in the time that a conventional field would be treated at the isocentre. For TSET, in order to achieve a flat profile in the vertical axis, two beams may be combined such that the 50% point of one beam overlaps the 50% point of the other (Richard, 1997).

Monte Carlo (MC) methods have been widely used to design radiotherapy beams because of their accuracy and efficiency in estimating the performance of various designs under consideration (Sung et al, 2005). It is well recognized that MC dose calculations are the most accurate way of computing patient relative dose delivery. Nevertheless, to achieve reliable results, some MC experience as well as the use of a powerful computing facility is needed (Faddegon et al, 1998, Ma and Jiang 1999). Fields greater than $20 \times 20 \text{ cm}^2$ are not commonly used in the clinic. Only very recent studies using Monte Carlo simulations cover electron beam commissioning of these large fields (Antolak et al 2002, Bieda et al 2001, Björk et al 2002). However, Monte Carlo applications for the design of TSET beams have been limited primarily because they involve large-scale simulations in time-consuming electron transport. Recent progress in computing power, (Pavón et al, 2003), demonstrated the capability of Monte Carlo simulations to evaluate the beam properties of the TSET unit (Pavón, et al, 2003, Sung et al, 2005).

2.5.1 TSET irradiation requirements

2.5.1.1 Irradiation beam requirements

When using electron beams, the most common situation would be to treat superficial tumours according to certain conditions and requirements of the radiation beam. These requirements involve characteristics of the treatment electron beam, the disease entity and the patient population. They include specification of: field size, penetration, energy, dose, dose rate, field flatness in the treatment plane, x-ray contamination, and the need for and nature of boost fields. The central requirement is to treat virtually the entire body surface to a limited depth and to a uniform dose using electrons with a low x-ray contamination. These requirements are coupled with the varied obliquity of body surfaces, beam directions, patient self-shielding, etc, (Hoppe et al, 1979). The required penetration depth of TSET treatment is usually varied with the stage and type of the disease and as well as the body surface. This penetration depth ranges from approximately 5mm to 15 mm or more at the 50 percent isodose surface which encompasses most lesions. It appears advantageous to provide more than one TSET beam energy to cover this range of depth.

Figure 2.7. shows Geometrical arrangements of the symmetrical dual-field treatment technique.

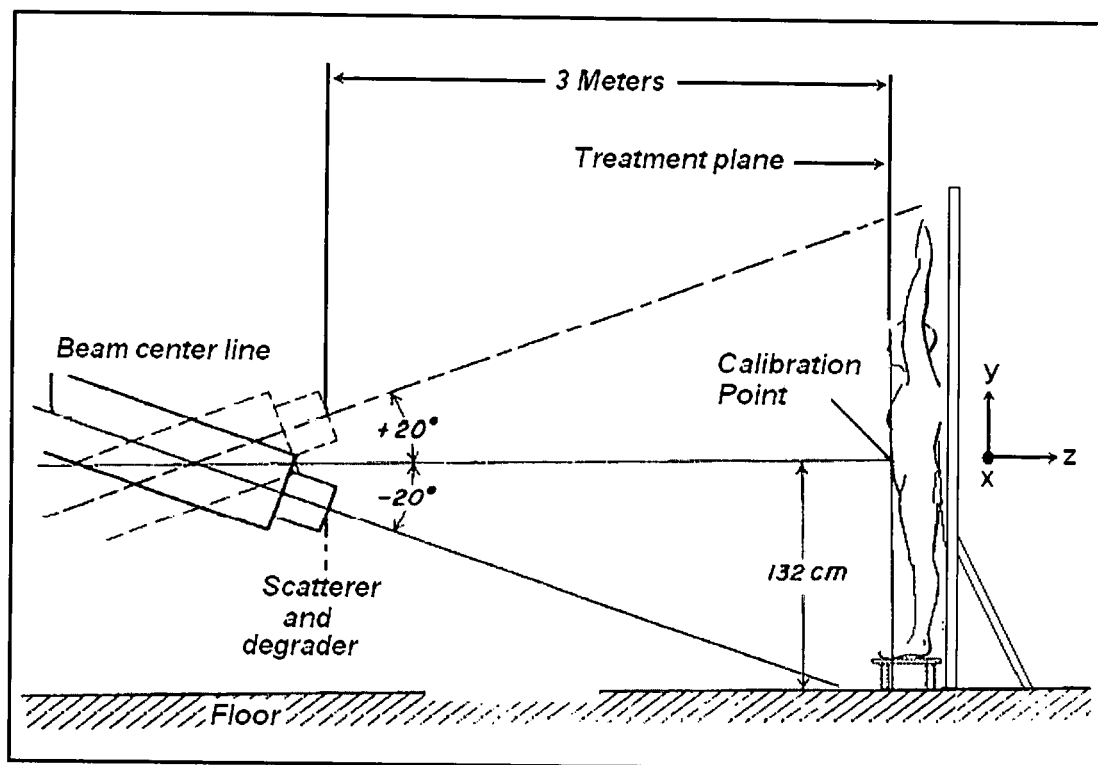


Figure 2.7. Geometrical arrangements of the symmetrical dual-field treatment technique. Equal exposures are given with each beam. The Calibration point dose is ($x=0$, $y=0$) in the treatment plane (Adapted from AAPM, 1988).

The electron beam incident on the exit window of the accelerator can be characterized by a relatively narrow distribution of energy fluence whose peak is termed the accelerator energy, \bar{E}_a (see fig 2.8). As the beam passes through the exit window and different materials between the exit window and the phantom surface, the energy will decrease and the energy spread will increase. The energy fluence distribution of such a beam arriving at the treatment plane (phantom surface) is characterized by its peak, or most probable energy, $E_{p,0}$, and a lower mean energy, E_0 . The value of $E_{p,0}$ can be obtained by subtracting the most probable energy loss in the energy-degrading materials traversed from the accelerator energy, E_a , or from the range-energy equation given below. In this

low energy range, the most probable energy loss for the low-energy TSET electrons is just the mean collision ionization energy loss for an electron of energy E (Khan, 2003).

The range-energy relationship:

$$E_{p,0} = 1.95R_p + 0.48 \quad 2.19$$

is used to relate the most probable energy at the phantom surface, $E_{p,0}$, in MeV, to the practical range, R_p , in cm of water. The mean energy at the phantom surface (treatment plane), E_0 , in MeV is related to the half-value depth, R_{50} , in cm of water by:

$$\bar{E}_0 = 2.33R_{50} \quad 2.20$$

The treatment beam traversing the patient or phantom further degrades and spreads out in energy. Its mean energy can be estimated as a function of depth, z , and the mean entrance energy, \bar{E}_0 , by the equation:

$$\bar{E}_z = \bar{E}_0 \left(\frac{z}{R_p} \right) \quad 2.21$$

As noted, equation (2.19) is used to relate the most probable energy at the surface, $E_{p,0}$, in MeV, to the practical range, in cm of water. The mean energy at the phantom surface (treatment plane), in MeV is related to the half-value depth and is usually in the range 3 to 7 MeV with accelerator energies, \bar{E}_a , ranging from about 4 to 10 MeV. Occasionally, lower energies have been employed. Most irradiation techniques involve significant electron energy loss from the sequence of materials traversed by the electron beam, as much as several MeV between the accelerator vacuum and the patient treatment plane (AAPM, 1988).

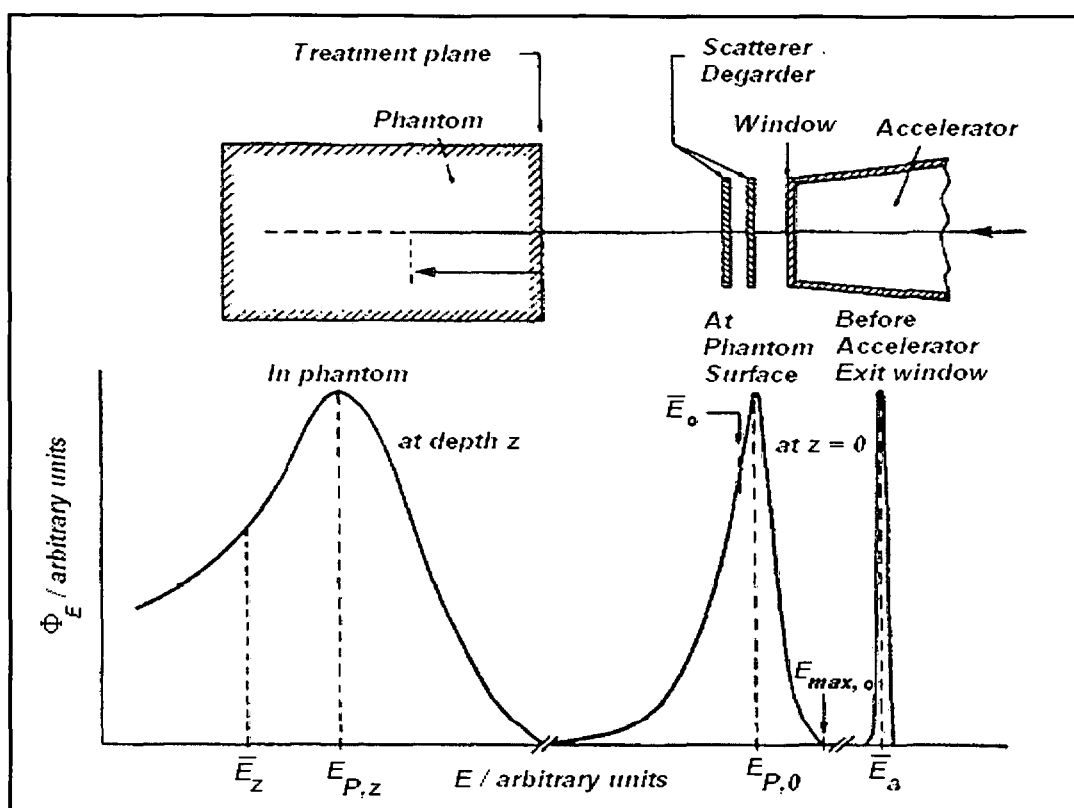


Figure 2.8: Distribution of electron fluence in energy, Φ_E , as the beam passes through the collimation system of the accelerator and the phantom (Adapted from AAPM, 1988).

Often, there are body areas shielded in part by other body sections or inadequately exposed because of limitations of the geometry of the treatment technique. Small supplementary boost fields of electrons or orthovoltage x-rays are therefore frequently needed. The accompanying megavoltage x-ray contamination is penetrating and forward directed; it often exposes much of the body volume and should be as low as reasonably achievable. It is roughly proportional to the number of fields used since all fields contribute penetrating x-rays; often it can be estimated prior to the selection of the technique. The average x-ray dose can be reduced by angling the beam axes so that the peaks of the forward-directed x-rays lie outside the body. A desirable x-ray contamination level averaged over the body volume is 1% or less of the total mean electron dose at dose maximum. This may be difficult to achieve with some equipment and techniques. Most TSET procedures are time-consuming to carry out because of the

multiple field and patient-position requirements. Since patients requiring TSET are often elderly and infirm, a high dose rate, which shortens the treatment time, is desirable. Average dose rates from 0.25 to several grays per minute at the depth of dose maximum are used, with the lower end of this range usually considered only marginally acceptable. Some patients require physical support devices to ensure their safety as well as correct positioning in a standing position. Radiation shielding of specific anatomical surfaces or organs may also be required. Commonly, finger and toe nails, tops of feet, and the eyes are protected during at least part of the treatment, with the use of shielding being dependent on the extent of disease (Karzmark et al, 1988).

2.5.1.2 Irradiation room requirements

Providing good dose uniformity over the height and width of a patient usually necessitates the use of large distances between scatterer and patient, typically 2-7 meters, with the distance being technique dependent. Hence existing treatment room layouts may restrict the choice of a TSET technique. The TSET procedure involves significant ozone production from ionizing large volumes of air in the treatment room. Frequent exchange of the air in the treatment room is essential for confining ozone exposure to acceptable limits. For most installations, the shielding provided by megavoltage x-ray treatment rooms has been found adequate for TSET therapy, which involves bringing a large fluence of energetic electrons into the treatment room. However, measurements must be made to ensure that radiation protection for TSET is adequate (Karzmark et al, 1988).

2.5.2 Irradiation techniques

The patient population requiring TSET is relatively small; therefore, the technique is available only in major radiotherapy centers. Prior to the use of electron beams, low-energy x-rays were used for total skin electron therapy. They presently have limited usage. The clinical results using a variety of such x-rays were less than encouraging because it was difficult to treat the entire skin area adequately. There was maximum field-size and field-junction limitations, and it was not possible to treat to an adequate depth without a large x-ray integral dose.

During this period, a number of TSET techniques adapted to the equipment available have been developed. Historically, machine-producing electrons have been used with an accelerator energy range, E_a , from 1.5 MeV to 10 MeV for TSET. The Van de Graaff generator, which was the first accelerator employed for TSET, has been largely supplanted by the isocentrically mounted electron linac. Electron beams from accelerators show the typical characteristics of a dose maximum occurring just below a normally incident skin surface and a rapid fall-off of dose with depth to maximum range determined by the incident electron energy (Ekstrand and Dixon, 1982).

There were different groups of techniques used in TSET treatment, such as translational techniques, in which the patient is placed in a horizontal position and is then translated with respect to a beam whose dimensions cover the patient laterally. In large field techniques, the patient is usually irradiated standing upright in the path of one or more fields, aiming to cover the upper and lower parts of the body. A number of large-field treatment techniques have been developed, some of which are very complex and time-consuming (Christina, 2005). However, the Stanford technique which utilizes a large horizontally directed electron beam produced by a medical linear accelerator and treats patients at extended distance in six standing positions has been adapted as the standard technique for TSET treatment (Richard, 1997).

2.5.2.1 Translational techniques

2.5.2.1.1 Beta particles

In this technique the patient lies on a motor-driven couch and moves relative to a downward-directed beam at a suitable velocity. Beta particles from radioactive sources, such as ^{90}Sr , provide an alternative electron source which are preferred because of their wide spatial divergence, broad spectrum of energies and low average energy (1.12 MeV) and have a limited penetration depth in tissue (Haybittle, 1957, Proimos, et al, 1960.). A $^{24}\text{Ci } ^{90}\text{Sr } \beta$ source in the form of a 60 cm linear array is used. The source is contained in a source shield housing and is positioned above the couch. The maximum energy of beta particles emitted by ^{90}Sr is 2.25 MeV. However, due to the spectral distribution of

β -ray energies the effective depth of treatment in this case is only a fraction of millimeter.

In a beta-particle unit, the ^{24}Ci source is spread over an area 53 cm long by 2 cm wide (Haybittle, 1957), a treatment distance of 40 cm was used, and the source was arranged horizontally with its long axis perpendicular to its direction of motion as it traversed the length of the recumbent patient. Although beta particles have been successfully employed for TSET, the majority of patients are treated with electrons from accelerators at this time. Long exposure times, lesser average penetration associated with their energy spectrum and poorer uniformity characterize beta-particle treatments. High output and the variable electron energy feature of linacs have led to their increasing adoption for TSET.

2.5.2.1.2 Narrow rectangular beams

In this technique, the Van de Graaff accelerator is in a fixed position with vertically downward narrow rectangular beams and patients are translated on a motor-driven couch placed under the electron beams (Williams et al, 1979). The energies used in this technique are about 1.5 to 4.5 MeV.

Another Van de Graaff TSET technique, made use of a wide cone with the beam scanned magnetically in vacuum transversely in the X direction while the patient is moved longitudinally under the beam in the Y direction. The dose distribution across the beam in a treatment plane was uniform to an extent dependent on the distance below the cone but at least as good as $\pm 5\%$. The energy of the Van de Graaff accelerator was adjusted to control the depth of penetration for treatment. Treatment times were about one minute for each full length pass and less for small treatment areas (Andrews and Swain, 1957).

2.5.2.2 Large electron field techniques

In order to achieve good uniformity in TSET treatment, the electron beam should cover the whole length of the patient. This requires a large electron field, which is produced by scattering electrons through a wide angle and using large treatment distances. The field is made uniform over the height of the patient by vertically combining multiple fields or

vertical arcing. The patient is treated in a standing position with four or six fields directed from equally spaced angles for circumferential coverage of the body surface.

2.5.2.2.1 Different categories in large field technique:

2.5.2.2.1.1 Scattered single beam

Different techniques have been employed to achieve uniform skin treatment by using a large electron field. The large electron beam can be produced by scattering a single field or parallel fields. Patients treated with a single electron field at extended distance showed excellent clinical results. A scattered single electron beam technique employing a linac for a standing stationary patient (Tetenes and Goodwin, 1977), in order to obtain a flattened beam with an electron energy of 4 MeV at the treatment plane, and initial accelerator energy of 6.5 MeV is used with a titanium scattering foil 0.15 mm thick placed 10 cm from the accelerator exit window. A shaped polystyrene scatterer beam-flattening filter is mounted on the front of the treatment head with a distance of 7 meters between the accelerator beam exit window and the treatment plane. The measured transverse uniformity in the treatment plane for this technique was $\pm 1\%$ within a 40 cm radius around the central axis and within $\pm 8\%$ for a 200 cm diameter circle. The maximum dose rate at the treatment plane with both the normal linac scatterer and the added scatterer in place was 3 Gy/min.

2.5.2.2.1.2 Pair of parallel beams

In this technique, two horizontal parallel beams are used and their axes are contained in a vertical plane at a treatment distance of about 2 meters. The technique was developed for an 8 MeV linear accelerator and includes the use of carbon energy degraders located just beyond the exit window of the accelerator. By using different thicknesses of carbon degraders, the depth of penetration was adjusted from about 2 to 25 mm to meet the requirements of the individual patient. Energy degraders (decelerators) produce less-rapid fall-off of depth dose, as well as a reduction in the beam energy; two horizontally directed beams, with a central axis vertical separation of 150 cm, were used to obtain $\pm 5\%$ uniformity for a treatment plane 200 cm high. The X-ray dose was about 2% of the

peak value for each field when using a 2 cm thick carbon decelerator. For thinner decelerators, the integral dose from electrons increased, but that due to x-rays showed little variation (Szur et al, 1962).

2.5.2.2.1.3 Pendulum-arc

An isocentrically mounted 8 MeV linac has been used in this technique (Sewchand et al, 1979). The accelerator is rotated continuously during treatment in a 50° arc about the isocenter starting from an initial angle with the beam axis aimed below the feet to a final angle with the beam aimed above the head of the standing patient. It may be feasible to vary the dose rate, or gantry rotation speed at constant dose rate, automatically, as a function of gantry angle so as to vary the dose rate and hence, optimize the dose uniformity in the vertical direction. A large Plexiglas sheet 1 cm thick placed 5 cm from the patient is used to degrade the beam energy further and provide large-angle electron scattering near the patient skin. A six-arc-field technique is described with the total x-ray dose measured at 10 cm depth equal to 4.2% of the average electron dose at the depth of maximum dose, D_{\max} .

2.5.2.2.1.4 Patient rotation

Studies of treatments involving patient rotation about a vertical axis for total skin irradiation include the work of Tetenes and Goodwin, 1977, Podgorsak et al, 1983 and Kumar, 1978. These groups use a single horizontal beam, the first with a single scatterer located near the beam exit window and a 7-meter treatment distance. The latter two groups have a first scatterer placed near the beam exit window and a second large planar scatterer located 20 cm from the treatment plane, which is located 265 cm and 3 m, respectively, (Kumar and Patel, 1978 and Podgorsak et al 1983) from the beam exit window. Podgorsak et al, 1983, have developed analytical expressions for rotational dose distributions using stationary depth- dose data and a variety of phantom and patient cross sections. The calculated and measured dose distributions show close agreement. With an accelerator electron energy of 6 MeV and a depth-dose curve equivalent to 3.5 MeV in the treatment plane, the x-ray background amounted to 4% compared to 2.2% for the Tetenes and Goodwin method.

2.5.2.2.1.5 Stanford technique (rotational technique)

In the Stanford technique, the patient is treated with six fields (anterior, posterior, four oblique) positioned 60 degree apart around the circumference of the patient. Each field is made up of two component beams, oriented at a suitable angle with respect to the horizontal. The patient treatment positions for the full six-dual field treatment cycle, is shown in figure 2.9.

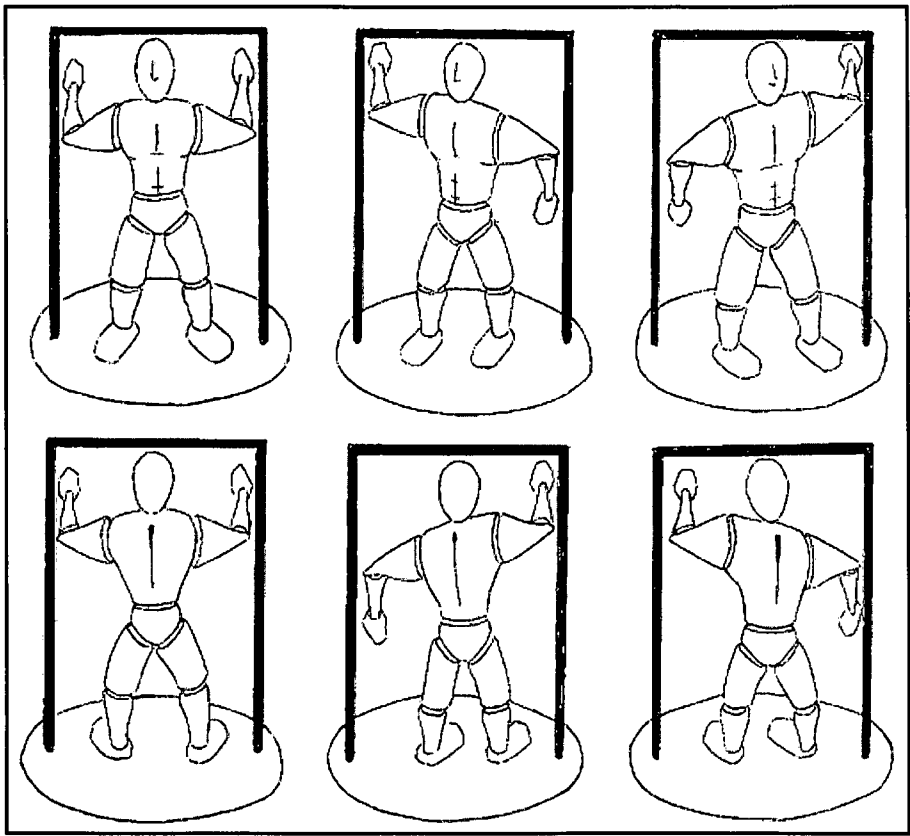


Figure 2.9: patient positions for the six–dual fields Stanford technique. Patient treated by two beams at each position, one beam directed below horizontal and the other above horizontal (Adapted from Chen et al, 2004).

The Stanford technique of six-dual fields, requires modification of the accelerator such as removing the scattering foil and installing a scatterer at the front of the collimator. These

changes would require safety interlocks to prevent operation of the accelerator in this configuration for conventional electron beam treatments.

Most institutions have adopted the Stanford technique in principle without making alterations in the accelerator hardware. Because the regular scattering foils and various interlocks are left in place, no special precautions are required in preparing the machine for Total Skin Electron Therapy. In some accelerators a high dose rate mode is installed to allow an output of more than 2000 monitor units per minute. This significantly speeds up the treatments. Because conventional electron cones are not used, the electron field is collimated by a special wide-aperture insert attached at the end of the collimator. It is preset via interlock to a wider jaw setting and specific electron energy, selected for high dose rate mode of operation.

To shorten the treatment time, the patient is treated with three dual fields per day, for example day 1: one dual field from the anterior, two dual oblique fields from the posterior; day 2: one dual field posterior and two dual fields anterior oblique. A complete cycle of six dual fields is thus completed in two days. A source-to-patient distance of about 4 m is sufficient for this technique (Khan, 2003).

2.5.2.2.1.5.1 Dual field angle

A low energy electron beam is considerably widened in size by scattering in air. As an example, a 9 MeV electron beam (of unspecified initial width), after transversing 4 m of air and an acrylic scatter plate, attains a Gaussian dose profile measuring a 90% to 90% isodose width of about 60 cm, which is usually sufficient to cover a patient's width. Along the height of the patient, two fields, one directed toward the head and the other toward the feet, are angled such that in the composite dose distribution a $\pm 10\%$ dose uniformity can be obtained over a length of about 200 cm (Khan, 2003).

A method of determining dual field angle by film dosimetry has been described by Khan, 2003. A series of dosimetry films in their jackets are mounted in a vertical board, larger than the height of a typical patient, and are positioned at the treatment distance. The scatter plate is placed in front of the films as in actual treatment. The films are exposed to

a single electron field directed at a 10 degree to 15 degree angle with respect to the horizontal axis. The films are scanned for an optical density profile in the vertical direction. The profile is then placed side by side with its mirror image and separated by a distance such that the combined profile shows not more than $\pm 10\%$ variation within about 200 cm. The separations between the two profiles gives the desired angle between the dual fields. A confirmatory composite profile is then measured by exposing the films to the dual fields with the interfiled angle determined above.

2.5.2.2.1.5.2 Calibration

A thin window ($\leq 0.05 \text{ g/cm}^2$) plane-parallel chamber is a suitable instrument for measuring the depth dose distribution for the low energy beams used for this technique. Because plane-parallel chambers are presently not calibrated by calibration laboratories, they may be calibrated by intercomparison with a calibrated Farmer-type chamber, using a high energy ($\geq 10 \text{ MeV}$) electron beam.

The AAPM, 1988 recommends that the total skin electron therapy dose be measured at a calibration point located at the surface of the phantom on the horizontal axis. This dose for a single dual field is called the *calibration point dose*, D_p .

A plane-parallel chamber, embedded in a polystyrene phantom, is positioned to first measure the depth dose distribution along the horizontal axis for the single dual field (the depth dose distribution can also be measured by a film sandwiched in a polystyrene phantom and placed parallel to the horizontal axis). The surface dose measurement is made at a depth of 0.2 mm.

Suppose M is the ionization charge measured, then the calibration point dose to polystyrene, $(D_p)_{poly}$, is given by:

$$(D_p)_{poly} = M \cdot C_{T.P.} \cdot N_{gas} \cdot \left(\frac{\bar{L}}{\rho} \right)_{air}^{poly} \cdot p_{ion} \cdot p_{repl} \quad 2.22$$

Where;

p_{repl} is the replacement correction factor

p_{ion} is the ion recombination correction factor

N_{gas} is the cavity-gas calibration factor

M is the charge measured

$\left(\frac{\bar{L}}{\rho}\right)$ is the restricted mass collisional stopping power

$C_{T,P}$ is the temperature and pressure correction factor

The calibration point dose to water, $(D_p)_w$, can then be determined as:

$$(D_p)_w = (D_p)_{poly} \cdot \left(\frac{\bar{S}}{\rho}\right)_{poly}^w \cdot \Phi_{poly}^w \quad 2.23$$

$\left(\frac{\bar{S}}{\rho}\right)_{Poly}^w$ is the mass stopping power ratio, water to polystyrene.

The electron fluence factor Φ_{poly}^w is approximately unity, because the calibration measurement is made close to the surface. p_{repl} can also be equated to unity for the plane-parallel chambers (AAPM, 1983). The parameters $\left(\frac{\bar{L}}{\rho}\right)$ and $\left(\frac{\bar{S}}{\rho}\right)$ are determined for the mean energy of electrons at the depth of measurement, which is given by equation 2.21.

The *treatment skin dose*, $\left(\bar{D}_s\right)_{poly}$ is defined by the AAPM as the mean of the surface dose along the circumference of a cylindrical polystyrene phantom 30 cm in diameter and 30 cm in height that has been irradiated under the total skin electron therapy conditions with all six dual fields. If $(D_p)_{poly}$ is the calibration point dose for a single dual field, then

$$\left(\bar{D}_s\right)_{poly} = (D_p)_{poly} \cdot B \quad 2.24$$

where B is a factor relating the treatment skin dose with the calibration point dose, both measured at the surface of a cylindrical polystyrene phantom. Typically, B ranges between 2.5 to 3 for a Stanford type technique.

The skin dose for a water phantom, $\left(\bar{D}_s\right)_w$ can be calculated from equation 2.22 and 2.23.

$$\left(\bar{D}_s\right)_w = \left(D_p\right)_w . B \quad 2.25$$

The factor B can also be determined by taping a film strip in its light-tight paper to the surface of a cylindrical polystyrene phantom, and exposing it to a single dual field. Another film strip taped around the phantom is exposed to six dual fields. By relating the optical densities to doses in the two cases, factor B can be determined from equation 2.23.

The composite depth-dose distribution for the six dual fields may be determined by sandwiching dosimetry film (in its paper jacket) in the cylindrical polystyrene phantom and cutting the excess film so that the edges conform to the circular surface of the phantom. A black tape is wrapped around the phantom over the film edges to make the film light-tight. The phantom, with the film parallel to the horizontal axis, is exposed to the six dual fields, duplicating the actual treatment conditions. After appropriate processing, the film is scanned for optical density distribution, which is related to the dose distribution by a reference sensitometric curve.

2.5.2.2.1.5.3 In vivo dosimetry

Although an overall surface dose uniformity of $\pm 10\%$ can be achieved at the treatment distance, in a plane perpendicular to the horizontal axis and within an area equivalent to a patient's dimensions, there are localized regions of extreme nonuniformity of dose on the patient's skin. Excessive dose (e.g., 120%-130%) can occur in areas with sharp body projections, curved surfaces, and regions of multiple field overlaps. Low-dose regions occur when the skin is shielded by other parts of the body or overlapping body folds. From in vivo measurements, areas receiving a significantly lower dose can be identified for local boost. If eyelids need to be treated, internal eye shields can be used, but the dose to the inside of the lids should be assessed, taking into account the electron backscatter from lead.

Thermoluminescent dosimeters (TLD) are most commonly used for in vivo dosimetry. For these measurements the TLD must be thin (<0.5 mm) to minimize the effect of dose gradient across the dosimeters. TLD chips are commercially available that meet these specifications. These chips can be sealed in thin polyethylene sheets to avoid contamination. The reference chips may be calibrated in a polystyrene phantom using an electron beam of approximately the same mean energy incident on the TLDs as in the in vivo measurement conditions. The desired mean energy may be obtained by selecting an appropriate incident beam energy and depth (Khan, 2003).

2.5.2.2.2 Dosimetric parameters in large field techniques

Dosimetric characteristics of TSET beams are examined for a single horizontal beam, a single angled dual-field beam, and the full array of six dual-field beams. These parameters include depth dose, isodose distributions, field flatness in the treatment plane and X-ray background.

2.5.2.2.2.1 Field flatness

Low energy electron beams are considerably widened by scattering in air. For example, a 6 MeV 20×20 cm² electron beam, after passing through 4 m of air, achieves a Gaussian intensity distribution with a 50% to 50% width of approximately 1 m (Holt and Perry, 1982). This usually gives adequate uniformity over the patient width. If two such fields are joined together vertically at their 50% lines, the resultant field will be uniform over a height of approximately 1 m. A proper combination of more such fields or a continuous arc can lead to a larger uniform field, sufficient to cover a patient from head to feet. The size and shape of an electron beam developed at a distance by air scatter can be estimated by multiple scattering theory. Holt and Perry, 1982, have used this approach to obtain a uniform field by combining multiple profiles in proper proportions and angular separation. In addition to air, the electron beam is scattered by the scattering foil inside (or sometimes, by design, an additional scattering foil outside) the collimator. However

the x-ray contamination would be increased, because unnecessarily wide beams waste electron flux to the sides.

2.5.2.2.2.2 X- ray contamination

X-ray contamination is present in every therapy electron beam and becomes a limiting factor in total skin electron therapy. Ordinarily, these X-rays are contributed by bremsstrahlung interactions produced in the exit window of the accelerator, scattering foil, ion chambers, beam-defining collimators, air, and the patient. The Bremsstrahlung level can be minimized if the electron beam is scattered by air alone before incidence on the patient. This would necessitate some modifications in the accelerator, such as removing the scattering foil and other scatterers in the collimation system. Various safety interlocks would be required to make this separation feasible for routine clinical use (Khan, 2003).

2.5.2.2.2.3 Dose distribution

The depth-dose distribution in a single large field incident on a patient will depend on the angle of incidence of the beam relative to the surface contour for an oblique beam, the depth dose curve and its d_{\max} shift toward the surface. When multiple large fields are directed at the patient from different angles, the composite distribution shows a net shift with apparent decrease in beam penetration. This shift of the relative depth dose closer to the surface has been explained by Bjarngard et al, 1977. as been due to the greater path length taken by obliquely incident electrons in reaching a point. Although dose uniformity of $\pm 10\%$ can be achieved over most of the body surface using the six field technique, areas adjacent to surface irregularities vary substantially due to local scattering. Areas such as the inner thighs and axillae, which are obstructed by adjacent body structures, require supplementary irradiation. The total bremsstrahlung dose in the middle of the patient for the multiple field technique is approximately twice the level of a single field. This factor of two has been experimentally observed by a number of investigations.

3 PRINCIPLES OF MONTE CARLO SIMULATION

3.1 Introduction

In the previous chapter the interaction processes of the electrons and photons were discussed. Although the physics of the interactions are well understood, in general it is impossible to develop an analytic expression to describe particle transport in a medium. This is because the electrons can create both photons (e.g., as bremsstrahlung) and secondary or knock-on electrons (δ -rays) and conversely, photons can produce both electrons and positrons. In addition, both electrons and photons scatter a great deal.

One widely used technique for solving this problem involves MC simulation of radiation transport in which one uses knowledge of probability distributions governing the individual interactions of electrons and photons in materials to simulate the random trajectories or histories of individual particles. One keeps track of physical quantities of interest for a large number of such histories to provide information about required quantities and their distributions.

MC techniques are becoming more and more widely used. In general this is because the cost of computing continues to decrease dramatically. In medical radiotherapy physics this increase in use is also because of availability of general purpose and specialized code systems, such as EGSnrc (Rogers, 2002) and BEAMnrc (Rogers et al, 2005).

3.2 The EGS4 code

The EGS (Electron–Gamma-Shower) code system for MC simulation of electron and photon transport (EGS4) is a FORTRAN based, electron and photon transport, Monte Carlo code (Rogers, 2002). The routines making up the package are coded in MORTRAN language, a macro extension to FORTRAN language (Richard, 1997). Macros are used as a faster method of coding frequently called geometry routines and the random number generator. EGS4 is comprised of internal and user oriented routines.

The EGS4 internal routines deal with specific elements of the particle transport. Standard EGS4 contains algorithms for photons to determine the consequences of Compton scatter, the photoelectric effect and pair production. For electrons bremsstrahlung, Möller scatter, Bhabha Scattering, annihilation events and multiscattering/ condensed history steps are considered. The EGS4 preprocessing package (PEGS4) calculates the relevant cross section data by reference to a suitable input file that contains among other variables the atomic composition, physical density and energy range over which the data must be generated for photons and electrons. The state of materials can be mixtures and compounds and can be generated of arbitrary density. The input requires setup for each material through which transport simulations are to be carried out. PEGS4 generates cross section data and the hatch routine places this data in accessible arrays for the EGS4 photon and electron interaction routines to use (Richard, 1997).

3.3 Random numbers generator (RNG)

Monte Carlo calculations attempt to stochastic nature of particle-particle interactions by sampling in a random fashion from known particle interaction cross-sections. This requires a random number generator (RNG) capable of producing a sequence of truly random numbers. A significant proportion of the computing time in a simulation is spent generating random numbers so it is important that the code used for generating these numbers is efficient (Metcalf et al, 1997). For the EGS4 code, the random number generator is of the multiplicative congruential type. The n^{th} random number is found recursively using the expression:

$$X_n = (aX_{n-1}) \bmod 2^\kappa \quad 3.1$$

where a is a constant multiplier and κ is the integer word size of the computer, “mod” is the modulo function. The first number in the sequence, X_0 , is called the seed and is usually specified by the user.

3.4 Electron transport

As an electron slows down in a material, it can undergo hundreds of thousands of scattering events and a large number of interactions. In order to simulate its energy loss and scattering through a medium efficiently a different approach is needed to account for energy loss and scatter (Metcalf et al, 1997). The EGS4 code utilizes the condensed random walk method. The electron loses energy in a continuous fashion by combining its interactions. The appropriate scatter angle is sampled from electron elastic multiple-scattering distribution functions (Nelson et al., 1988).

In an actual MC simulation the user must define the lower bound of the electron's kinetic energy transport by specifying the variable ECUT. An ESTEPE variable is also specified that indicates the maximum fractional energy loss an electron can experience (Rogers et al, 2005). An algorithm called PRESTA was also introduced that optimizes the accuracy of energy deposition with simulation speed (Bielajew and Rogers, 1988 and Nelson et al, 1988).

3.5 Running the EGS4 code

The beauty of the EGS4 system is that a structured set of subroutines handles all of the physics in the simulation in a manner which allows users to write their own geometry and scoring routines without actually altering the EGS system itself. The user is responsible for writing the main program that contains two subroutines, HOWFAR and AUSGAB (Rogers, 2000). HOWFAR determines the geometry of the simulation and AUSGAB determines the dose scoring zones. These subroutines have been generalized in user friendly codes such as DOSXYZ and BEAM that allow the use of these powerful EGS4 transport simulation codes without any knowledge of MORTRAN.

3.6 The BEAMnrc code

3.6.1 Introduction

The BEAMnrc code has been designed to simulate the radiotherapy beams from any radiotherapy sources, including low energy x-rays, ^{60}Co units, and both electron and

photon beams from accelerators (Rogers et al, 1995). BEAMnrc is based on the PRESTA algorithm extension of the EGS4 / MC code system for simulating radiation transport.

The BEAM model can be build from a series of individual component modules (CMs), each of which operate completely independently of the other component modules and contains between two planes which are perpendicular to the z-axis and which can not overlap (Rogers et al, 1995). The beam axis is usually defined from the origin of the center of the beam as it exits from the accelerator window. The CMs in the BEAM code can be used for modeling the accelerator components such as; exit window, scattering foil, primary collimator, ionization chamber, mirror, jaws, etc. For each CM, all the geometrical and physical properties of the materials are specified at run time.

3.6.2 Running the BEAM code

There are three main stages are involved running the BEAM code (Rogers et al, 2005):

a) “Specifying” Accelerators:

Before compiling and running a BEAM accelerator simulation, user must “specify” which component modules are to be used and in what order. The user may use the same CM as often as needed, as long as the identifiers used are unique. The user also has to specify the accelerator model via giving it a name representing the machine they are modeling.

b) Building an accelerator:

Once the accelerator has been specified, it must be “built”. Building an accelerator consists of gathering all the source code, automatically editing it to avoid duplicate names (Awusi, 2000). The user has to specify the modules to use.

c) Compiling an accelerator:

Once the accelerator specified and built, the accelerator must be compiled. This required the MORTRAN and FORTRAN code. The user has to specify the name of

the specific module they are running and once that is done the user is presented with a compilation menu with several options to select and modify before BEAM is compiled.

At this stage of the simulation with the BEAM code, some of the main tasks of the user are to:

- (a) Specify the geometry of the accelerator, which are the dimensions and materials of the treatment head.
- (b) Specify the variance reduction techniques.
- (c) Specify the transport parameters (the PCUT and ECUT values).
- (d) Specify the physical properties of each material to be used in the simulation.
- (e) The track of the particle's history by using the LATCH feature.
- (f) Define the location of the scoring planes of interest to the user.

3.7 Efficiency and variance reduction techniques

The efficiency of a particular simulation is inversely proportional to both the variance of the results and the time taken for the simulation (Metcalf et al, 1997). If the uncertainty of a result is σ and the computing time used in the simulation is t , then the efficiency ε is defined as:

$$\varepsilon \propto \frac{1}{t \cdot \sigma^2} \Rightarrow \varepsilon = \frac{K}{t \cdot \sigma^2} \quad 3.2$$

where K is a proportionality constant.

since t is directly proportional to N , by assuming ε to be a constant, then equation 3.2 can be rewritten as

$$\varepsilon = \frac{K}{N \sigma^2} \Rightarrow \sigma = \frac{\kappa}{\sqrt{N}} \quad 3.3$$

where $\kappa = \sqrt{K/\varepsilon}$ is another constant.

Since the fractional uncertainty is inversely proportional to the square root of the incident numbers, it is also inversely proportional to the square root of the simulation time. This means that efficiency is invariant with simulation time for a particular simulation type.

It is possible to increase efficiency by using variance reduction techniques, where either, (a) the variance for particular simulation time is reduced or (b) the time required to obtain results with in a certain variance is reduced (Metcalf et al, 1997). There are various techniques for variance reduction (Bielajew et al, 1988), but those employed by the BEAM code are:

i) **Range rejection:**

Range rejection can save significant quantities of computing time for electron transport calculations. The basic method is to calculate the residual range of a charged particle and terminate its history if it can not escape from the current region (Rogers et al, 1995). The BEAM code includes a subroutine, which is used to pre-compute the residual range of the threshold energy in each medium as a function of electron energy. BEAM can automatically compute the minimum energy needed by electrons as they leave each CM if they are to reach the scoring plane and this can be the energy used in the range rejection routines. The transport cut-off energies it has to be set at $ECUT = AE = 0.70 \text{ MeV}$ for electrons and $PCUT = AP = 0.01 \text{ MeV}$ for photons (Rogers et al, 2005).

ii) **Bremsstrahlung splitting and Russian roulette:**

For the simulation of clinical photon beams from a therapy machine, a variance reduction technique called "Bremsstrahlung splitting" can be used in BEAM to increase the number of Bremsstrahlung photons created in the simulation geometry. At each Bremsstrahlung interaction most of the time is spent in tracking of the electron histories. The statistical uncertainty in photon energy fluence spectrum scored for a given number of photons of incident electrons can be reduced dramatically since most of the time in these simulations is taking up by tacking electron histories. BEAM can use Russian roulette on the electrons created in the

multiplicity of bremsstrahlung photons. In fact, Russian roulette means the number of electrons followed is restricted to the same number as would occur if bremsstrahlung splitting were not used (Rogers et al, 1995).

iii) **Photon forcing:**

The BEAM code offers an option whereby the user can force photons to interact in specified CMs within a simulation. One of the main purposes of implementing this option was to study the generation of contaminated electrons in a photon beam. In BEAM, photons can be forced to interact in any subset of a component module (Rogers et al, 1995).

3.8 Phase space files

One of the most important outputs of the BEAM code simulation is the phase space file (PSF). A phase space file contains data relating to particle position, direction, charge, etc. for every particle crossing a scoring plane (Rogers et al, 2005). A Phase space files can output for each scoring plane in an accelerator simulation, input file for other simulations or used as input file for the calculating the dose through DOSXYZ program.

Usually the Phase space file contains:

- a) The Particle position, direction and energy.
- b) Particle charge e.g. positive charge for positrons, negative charge for electrons or zero charge for photons.
- c) Total number of particles.
- d) Total number of photons, electrons and positrons.
- e) Maximum and minimum kinetic energy of the particles.
- f) Number of particles (histories) incident from the original source used to generate the PSF.

The PSFs created can be analyzed by another program BEAMDP.

3.9 BEAMDP program

Another important program for processing phase space files is the BEAMDP program. The BEAMDP (BEAM Data Processor) is a subsidiary of the BEAM program (Ma and Rogers, 2005). BEAMDP helps the BEAMnrc users to analyze the beam data obtained by the Monte Carlo simulation of the coupled transport of photons and electrons in a clinical accelerator and to derive the data required by the simplified sub-source models of these electron beams for use in Monte Carlo radiotherapy treatment planning.

When running BEAMDP, the user is having several options to analyze from the phase space file; some of them are:

- a) Derivation of planar fluence distributions. The program gives the total number of particles scored in spatial bins of equal area. Usually a plot of fluence versus position in the X-direction is given.
- b) Derivation of spectral distributions. The program gives the total number of particles scored in each energy bin of user specified bin width within a specified spatial region. Usually a graph of planar fluence per incident particle versus energy (MeV) is plotted.
- c) Derivation of the mean energy distributions. The program gives the ratio of the total particle energy to the total number of particles scored in a spatial bin of equal area.
- d) Derivation of angular distributions. The program gives the total number of particles scored in an angular bin of user specified bin width within a specified spatial region. Usually a plot of particles per bin versus angle in degrees is given.

Also the user has to describe the input parameters e.g., the file name, field type, particle type, type of graph, scoring regions for spectrum and angular distributions, energy ranges and range of angles for angular distributions.

The BEAMDP program analyzed the phase space data and generates energy distributions for particles inside and outside the treatment field.

3.10 DOSXYZ code

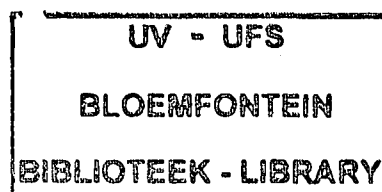
The DOSXYZ is an EGSnrc based Monte Carlo simulation code for calculating a 3D absorbed dose (Walters et al, 2005). The co-ordinate system is cartesian. The geometry consists of a rectilinear volume with perpendicular x, y and z directions. The dimensions of the voxels are completely variable in all three dimensions. The material in each direction can be specified and its density can be varied. The code allows sources such as a monoenergetic diverging or parallel beam, phase-space data generated by a BEAM simulation, or a model-based beam reconstruction produced by BEAMDP. DOSXYZ also has parameter ISMOOTH that can be used to redistribute PSF particles when used more than once during a simulation.

3.11 CT Based Phantom/ CTCREATE

The CT phantom is an option of DOSXYZ code that allows calculation of dose distributions in phantoms that are derived from CT data sets (Walters et al, 2005). This allows simulations in realistic anthropomorphic phantoms. At this point in time, the system fully supports data in sets in the ADAC pinnacle format, the CADPLAN format and DICOM format. It is possible to generate a CT phantom from CT data sets since all the required material and geometry information is contained in the data set.

There are several input parameters that the user has to specify in order to use the CT Phantom/ CTCREATE program:

- (a) The Format of the CT data.
- (b) The CT file name, the name of the file containing either the header information (pinnacle) or specifying the names of the actual CT data files (CADPLAN and DICOM), that make up the full CT image (one file/slice). Files must be in order of increasing Z.
- (c) The lower and upper X, Y, Z boundaries (cm) for the subset of the CT data to be considered for the DOSXYZ phantom.
- (b) The voxel dimensions in X, Y, Z to be used in DOSXYZ.



- (c) The number of the materials and ramps that are to be read from the file.
- (d) The transport parameters e.g. the ECUT and PCUT values.

After the successful data input of CT Phantom/CTCREATE, the appropriate CT phantom information is stored in "file.egs4phant", where "file" is the original CT data set name. This CT phantom file created can then be read in and used by the DOSXYZ program to calculate the dose distribution in each voxel of the phantom. The CT phantom option in DOSXYZ is used by setting the number of materials (nmed) of the DOSXYZ input file to zero, which causes the program to execute differently than when $nmed > 0$. Instead of geometry, material and density data being input in the DOSXYZ input file, DOSXYZ reads data from a CT phantom file that has been created using CTCREATE (Awusi, 2000, Rogers et al 1995) .

4 MATERIALS AND METHODS

4.1 Introduction

In this study the Elekta Precise linear accelerator with High Dose Rate Electron (HDRE) mode was investigated for TSET treatment. This accelerator has three x-ray energies (6, 8, 15 MV) and is also capable of producing electrons of 4, 6, 8, 10, 12 and 15 MeV. The 4 MeV and 6 MeV electron energies were investigated in this study because only these two energies are available for High Dose Rate Electron mode. The distance from the isocentre of the accelerator to the treatment plane was 250 cm. The treatment is to be delivered from six equally spaced patient orientations by rotating the patient through 60 degrees after each stationary beam had been delivered. The treatment length will be encompassed by irradiating from two different vertical angles.

The first step for commissioning a TSET technique is to determine the characteristics of the beam data at isocentre (at 100 cm Source Skin Distance (SSD)) and at the treatment plane (at 350 cm SSD). Since our objective was to use Monte Carlo simulation in the commissioning of a TSET technique, the first step was to match the MC simulation with data obtained for a single horizontal beam. MC simulation for the linear accelerator head was done to obtain the beam data for the 4 and 6 MeV electrons. Phase Space Files (PSFs) were generated, and then analyzed to get the energy spectrum and angular distributions. The BEAM and the BEAMDP, MC codes (Rogers et al, 2005) were used for the simulation of the accelerator and analysis of the data files. The DOSXYZ and the CTCREATE MC codes were used for the calculation of the 3D dose distributions in the water phantom and CT based patient models. The beam data obtained by the DOSXYZ code in the water phantom was verified by comparing it with data measured in a polystyrene phantom for the same Elekta Precise machine. The dose distributions obtained by the MC data in the simulation of the Rando phantom were directly compared with measured data by using films and TLD dosimeters.

In this chapter, in section (4.2) the HDRE special procedure mode is discussed. In section (4.3) the procedures followed in the measurement of the beam data on the Elekta Precise linear accelerator, the multiple field measurements for irradiation of the Rando phantom and the absolute measurements are described. In section (4.4.1) details of the construction of the MC model of the Elekta Precise linear accelerator, in the 4 and 6 MeV mode that was used for the simulations is described. Section (4.4.2) outlines the detailed modeling of the Elekta Precise accelerator from the electron window up to 100 cm SSD (isocentre) to obtain a Primary Phase Space file (PPSF). The PPSF was then used as source in the simulation of the second stage, which entailed transport through air up to treatment plane to obtain secondary phase space files (SPSF's). Section (4.4.3) gives a brief discussion on how the PSFs were analyzed. Determination of the primary electron beam parameters are discussed in section (4.4.4). In Section (4.4.5) the procedure for the calculation of the absorbed dose distributions in a water phantom from the generated PSFs with the DOSXYZ MC code is discussed. In section (4.5) the method used for the comparison of the MC calculated data and the ionization chamber measured data is outlined. In section (4.6) a procedure followed in CT based MC simulation using the CT based Phantom/CTCREATE program is discussed. This data is then used directly for the preparation and running of the DOSXYZ MC code to calculate 3D dose distributions in a whole patient's skin. In Section (4.7) a procedure for the comparison of the dose distributions from the MC method and film measurements is presented.

4.2 HDRE - special procedures mode

Our TSET unit in this study is based on the 4 and 6 MeV electron beams from an Elekta Precise medical linear accelerator, operating in the High Dose Rate Electron (HDRE) mode. The treatment head geometry is the same as in the standard 4 and 6 MeV electron modes.

As this technique requires the patient to be positioned at a considerable distance from the treatment machine (e.g. 3-7m), one of the main problems with this is that patient dose rate is considerably lower than at the isocentre so the treatment times are extended,

making patient movement more likely. HDRE reduces this problem by allowing the electron dose rate to be increased.

The HDRE mode is controlled by an independent program, but shares the same scattering foil assembly with the conventional electron beams (Precise Operators Manual, 2003). To prevent unauthorized use of this mode, a HDRE key must be inserted at the control console and a HDRE applicator must be inserted into the head of the treatment unit. This applicator does not collimate or modify the electron beam in any way, although it may be used as a support plate for devices used to scatter the beam or degrade its energy (see figure 4.1 and 4.2). On entering the HDRE treatment mode, the X-ray collimators are automatically set to the maximum collimator setting of 40x40 cm² projected to 100 cm SSD.

The high dose rate interlocks prevent dose rates exceeding 1000 MU per minute during non-HDRE treatments. In addition to this feature, an interlock is provided which terminates radiation if the measured dose exceeds 125 percent of the nominal dose rate for a period of five seconds (Precise Operators Manual, 2003).

In order to deliver a high dose rate with the HDRE option, an electronic attenuator is introduced into the dosimetry circuit which divides the dosimetry signal by an approximate factor of 10, allowing HDRE dose rates of 3000 MU per minute at isocentre. This means that during HDRE operation the dose and the dose rate reading at the console do not reflect the dose at the isocentre as for normal treatments, but that at a distance of approximately 3-4 meters from the isocentre.

In this Elekta Precise linear accelerator the HDRE beam is configured to a nominal energy of 4 MeV as option HDRE1, and 6 MeV as option HDRE2.



Figure 4.1. The high dose rate electron applicator.

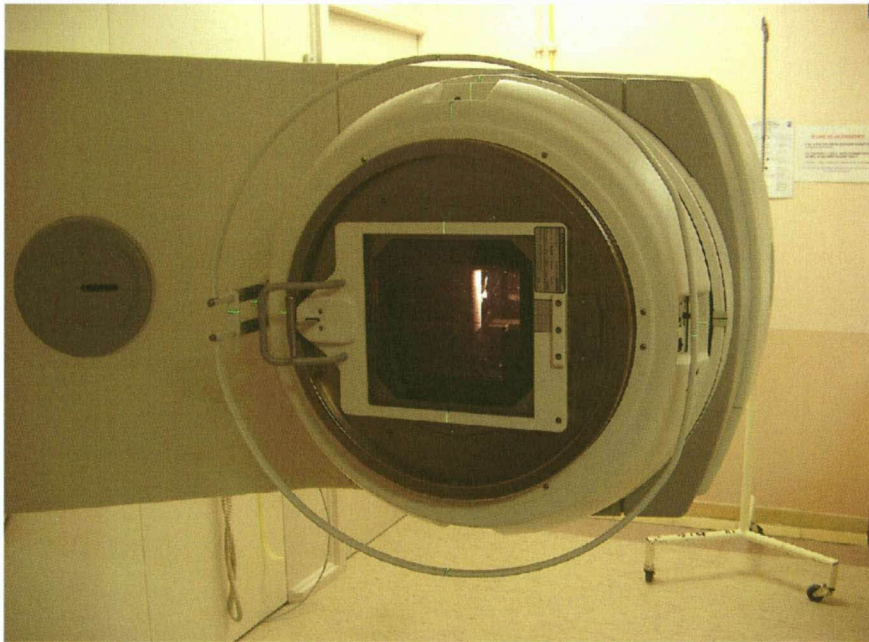


Figure 4.2. The high dose rate electron applicator attached to the head of the Elekta Precise treatment machine.

4.3 Experimental measurements

4.3.1 Depth dose measurements

All the depth dose measurements at the machine isocentre (100 cm SSD) were made with the gantry angle 0° (beam pointing down) and at the treatment plane (350 SSD cm) with the gantry angle 90° (beam horizontal). Measurements were carried out with both a SHM parallel-plate ionization chamber (fig 4.3.a) connected to a Keithley 602 solid-state electrometer (fig 4.3.b), and with Kodak EDR2 (Extended Dose Range) film in a polystyrene phantom. The ionization chamber was embedded in a Perspex block with dimensions $15 \times 15 \times 5 \text{ cm}^3$, such that the top surface of the chamber (the effective point of measurement) was flush with the top surface the phantom (fig. 4.3). Polystyrene sheets (which have dimensions of $15 \times 15 \times 0.15 \text{ cm}^3$) were then added on top of the detector to achieve a range of depths from the surface to 200 mm depth. The density of the polystyrene was taken into account by multiplying all depths by a factor of 1.06. A depth dose curve was drawn by taking readings at the different depths. At each depth, three readings were taken, and these reading were then averaged. The depth ionization curve was converted to a depth dose curve by applying stopping power ratios for water to air (Ding et al, 1995); this curve was then normalized to its maximum value.

For the film measurements, a calibration curve was determined as follows: single sheets of ready pack Kodak EDR2 film from the same batch were cut into several equal sections and each packet was sealed with black insulation tape. These films were all irradiated on the Elekta Precise linear accelerator using a 10×10 field, at an SSD of 100 cm to the top of a solid phantom with a thickness of 10 cm. The films were placed perpendicular to the beam central axis at the depth of d_{max} for each electron energy. Doses of 50, 100, 200, 300, 400, 500, and 600 cGy were given to establish the characteristic curve for the EDR2 film. The films were all developed in one session in a Dörr automatic film processor. The optical density of the films was measured using a B/W densitometer Model TDX. The depth dose data were obtained by placing unpackaged film in a RMI solid water film cassette designed for this purpose. After irradiation of the films, the central axis data were measured using a Wellhöfer Model WP102 scanning densitometer running WP700 software. The film data were compared against measured central axis percentage depth

dose data obtained with the SHM ionization chamber and those derived from Monte Carlo simulation. The measurements and simulations of the PDD curves were performed for both electron energy settings of 4 MeV and 6 MeV.

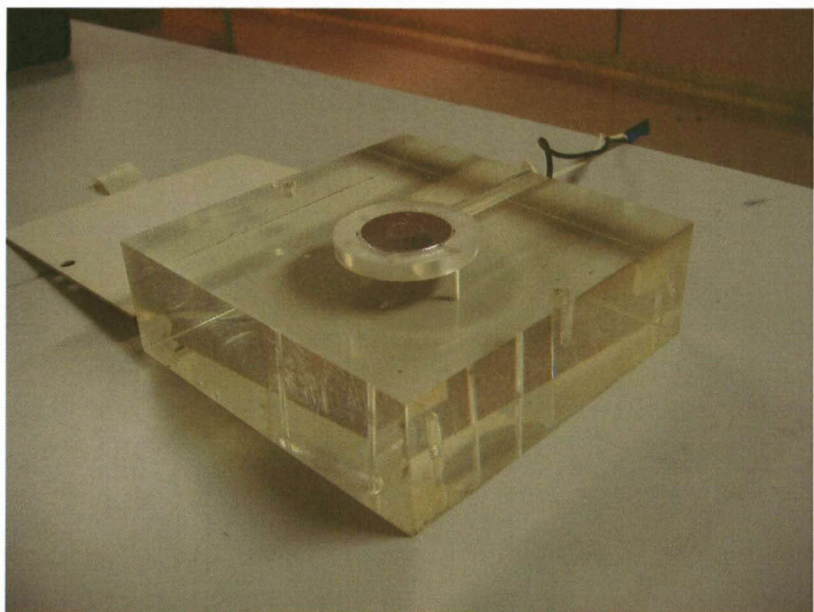


Figure 4.3.a. SHM ionization chamber embedded in a Perspex block.

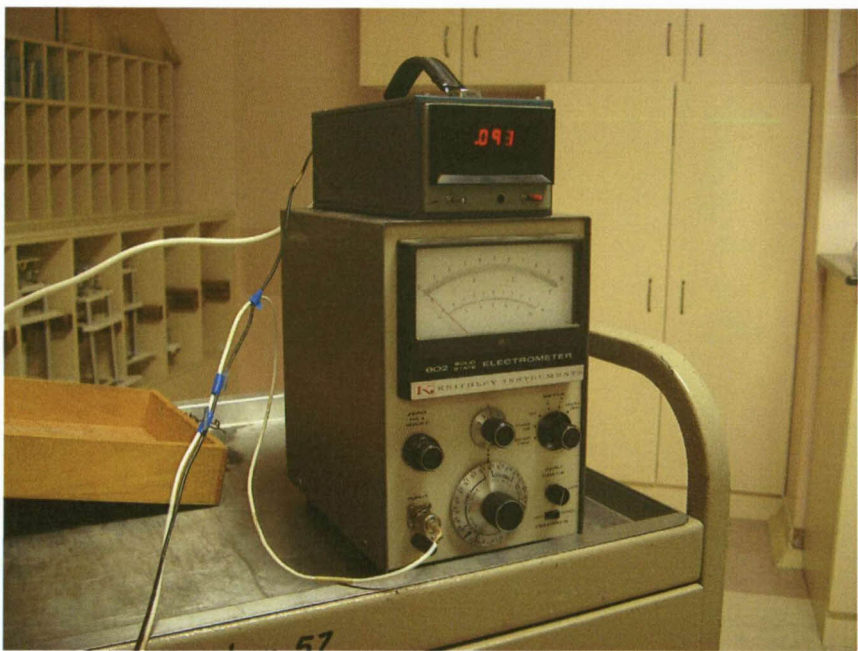


Figure 4.3.b. The ionization chamber and the electrometer that were used in the beam data measurements.

4.3.2 Beam profile measurements

The cross-beam profiles at the corresponding depth of the dose maximum at 100 cm SSD were measured in a polystyrene phantom for both 4 and 6 MeV energies. The ionization chamber was placed at a depth of d_{\max} for each electron beam energy. The x-ray collimator field size was automatically set to $40 \times 40 \text{ cm}^2$ projected at 100 cm SSD by using the high dose rate applicator. A series of readings were taken by positioning the ionization chamber at various off-axis distances from the central axis. Three readings were taken at each position and then averaged.

The cross-beam profiles at the treatment plane were measured with the gantry rotated to 90° . These beam profiles are very large, which means that conventional water phantom measurements are not possible. A polystyrene phantom was used. The ionization chamber was localized at the depth of the maximum dose (d_{\max}), positioned vertically at isocentre height at 350 cm SSD, and then moved to different positions horizontally perpendicular to the central axis. Readings were taken up to about 200 cm off-axis on both sides of central axis in increments of 5 cm. Great care was taken to accurately position the ionization chamber for these measurements (see figure 4.4). Plots of the depth doses and cross-beam profile curves are shown in the results.

Electron beam parameters, namely the depth of the maximum dose (d_{\max}), depth of the 50% dose (R_{50}) and practical range (R_p), were determined from each depth dose curve.

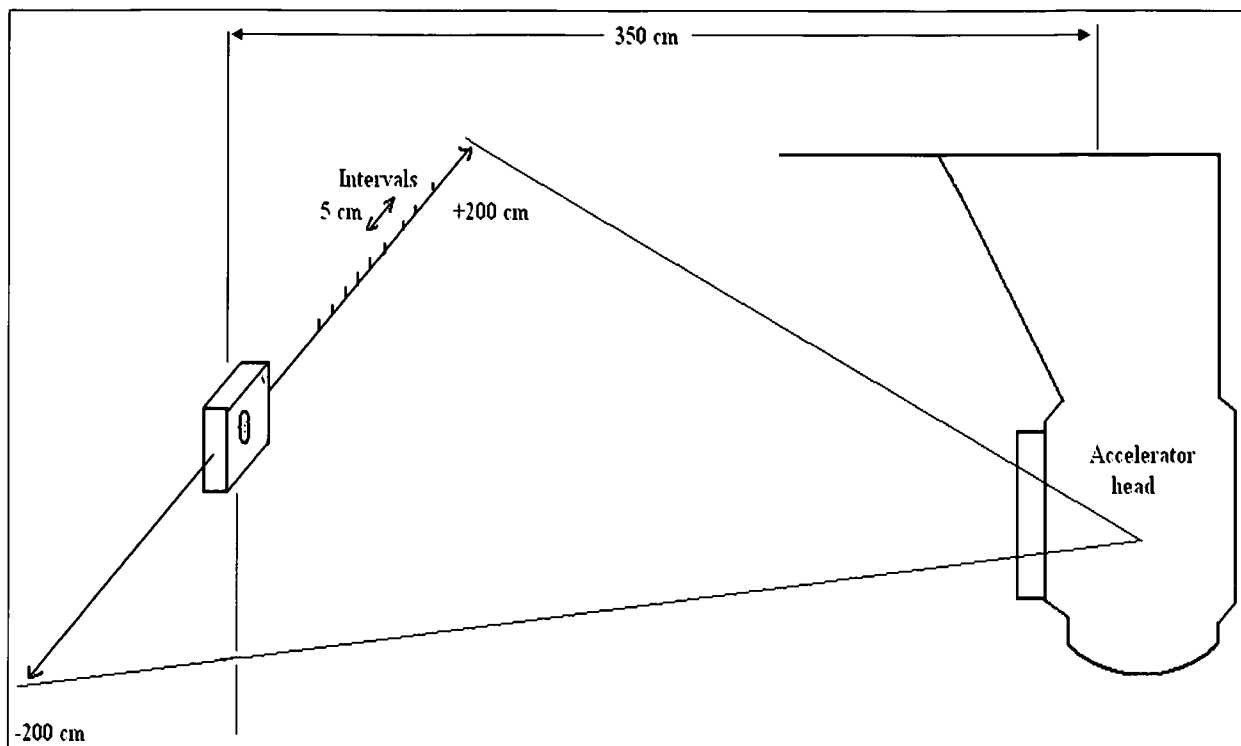


Figure 4.4. Schematic diagram for the beam data measurements.

4.3.3 Multiple field measurements

The purpose of these measurements was:

- To investigate the effective depth dose for multiple fields.
- To investigate the regional distribution of dose over a Rando phantom.
- To investigate the *in vivo* measurements using a Rando phantom.

Several different types of phantom were employed including a Rando phantom and a cylindrical phantom (see fig 4.6). Dosimetric measurement of TSET was important for the determination of the distribution of the dose to the Rando phantom surface and verifying that the monitor units were correct. Film and lithium fluoride thermoluminescent dosimeters (TLD) were used in a complementary way.

The TSET technique chosen was similar to the modified Stanford technique (Karzmark et al, 1988), but with variation of the gantry angles used along with the irradiation fields. Film was used to determine depth doses from multiple beams; the bare film was placed between the Rando phantom slices, cut flush to the phantom surface, and sealed with two layers of black electric insulation tape in the dark room. The Rando phantom slices containing the film were clamped tight to eliminate air gaps between the film and the phantom surfaces. The films were introduced into the Rando phantom between slices at four different levels namely, head, thorax, navel and pelvis level as shown in figure 4.5. The Rando phantom was positioned on top of a rotating platform that was placed at the treatment plane at 350 cm SSD as shown in figure 4.6. Six beam pairs were employed (the major contribution at any given point is from three). After each irradiation of a beam pair the phantom was rotated through 60 degrees. Although film was not used for absolute measurements we were able initially to relate a dose from the TLD, which was calibrated by placing several dosimeters at the calibration position. The 12 fields were applied and 200 MU was delivered per field. Six fields were delivered with a gantry angle of 104° and 106°, and the other six fields were at 76° and 74° for 4 and 6 MeV respectively. After irradiation, the films were taken out in the dark room and were processed at the same time with the dose calibration films. The radiation pattern on the films was a series of concentric rings. The films were scanned using a Wellhöfer WP102 Densitometer to determine the PDD and isodose curves.

For the cylindrical phantom the film was also introduced between two slabs of the phantom and sealed with black insulation tape and positioned at the treatment plane to obtain the beam data.

When six TSET beams are delivered in patient treatments, the dose delivered to any point on the patient surface will be larger than what would have resulted from a single beam due to the overlap of adjacent beams. The ratio of the dose delivered to the skin by the six-beam treatment to that delivered at d_{\max} by a single TSET beam given the same beam-on time was defined as the overlap factor (Cox et al, 1989 and Karzmark et al, 1988). An accurate determination of the overlap factor is important in TSET dosimetry as it

determines the beam-on time of the TSET beams for a given prescribed skin dose. The overlap factor for this technique was measured at the level of the horizontal beam axis by using both radiographic film and TLD. Once the overlap factor was determined, the MU needed to give a prescribed skin dose in the TSET treatment can be calculated. Using the calculated MU, doses to other anatomic locations, from six-beam TSET treatment, were measured using TLD on the Rando phantom.

For TLD measurements, the TLDs were taped to the surface of the Rando phantom at the level of the beam axis for the six-beam irradiation. To minimize the statistical uncertainty of TLD, three TLD chips were placed at each anatomic location. *In vivo* dose measurements using TLD were performed according to an established procedure or protocol in our department, which is described briefly below. A group of 25 LiF TLD chips were used. The TLD chips were stored in a holder containing an aluminum tray. Each TLD chip was numbered by writing on one side with a pencil. Before the dose measurements, the relative response of each TLD chip was quantified as follows: The TLD chips were annealed in the aluminum tray at 400°C for 1 h followed by 80°C heating for 16 h. The TLD chips were then irradiated to the same uniform dose in a VINTEN 623 irradiator containing two opposing sources of $\text{Sr}^{90}/\text{Y}^{90}$ of 37 MBq. After irradiation and a waiting period of at least 3 h, the responses of the TLD chips were measured with a TOLEDO 654 TLD reader. This process was repeated five times and the average response of each TLD was obtained. The relative response of each chip (or chip factor) was calculated as the quotient of the average response of the whole group to the average response of the individual TLD chips in the given cycle. The batch of TLD was then annealed and marked ready for dose measurement. For dose measurement, the relationship between absorbed dose and TLD response was determined by calibrating five TLD chips from the same batch in the 6 MeV electron beam of the Elekta Precise linear accelerator. The dose measured by a TLD chip for a patient is then calculated as the product of the dose conversion factor and the net TLD response corrected by the chip factor.

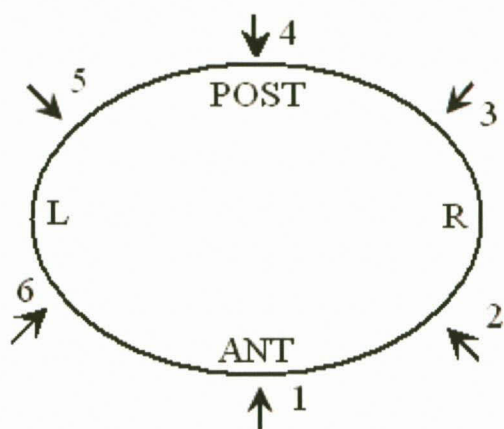
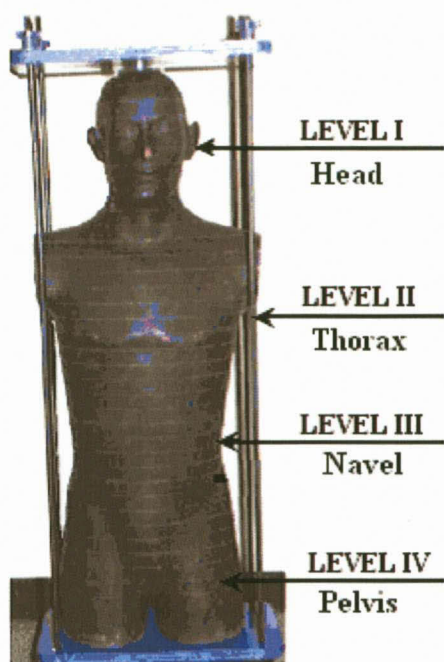


Figure 4.5. The positioning of the films at the different levels in the Rando phantom and orientation for the six-dual fields (top) and the cylindrical phantom (bottom).



Figure 4.6.a. The positioning of the Rando phantom at the treatment plane.

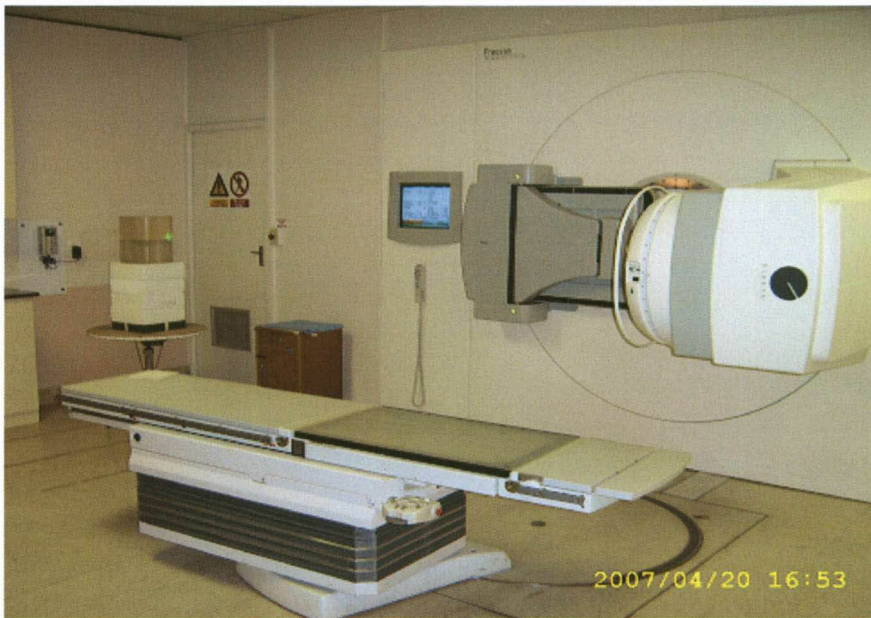


Figure 4.6.b. The positioning of the cylindrical phantom at the treatment plane.

4.3.4 Absolute dosimetry

A plane - parallel ionization chamber (Roos chamber) with plastic phantom has been used in this study (according to the AAPM report No. 23 recommendations) (AAPM, 1988) for measuring the depth dose distribution. The calibration depths were measured from the depth dose curves for the 4 and 6 MeV beams. The x-ray contamination was measured from the tail of the depth dose curves according to the accepted method (ICRU Report 35, 1984).

4.4 Monte Carlo simulation of the Elekta Precise accelerator

4.4.1 Modeling of the radiation head of an Elekta Precise linear accelerator

The Elekta Precise linear accelerator was used in this study. The construction details of the treatment head were provided by the manufacturer. Figure 4.7. shows a schematic of the TSET unit assumed in our EGS4/BEAM simulations of the main components of the Elekta Precise in the 4 and 6 MeV electron beam configuration mode.

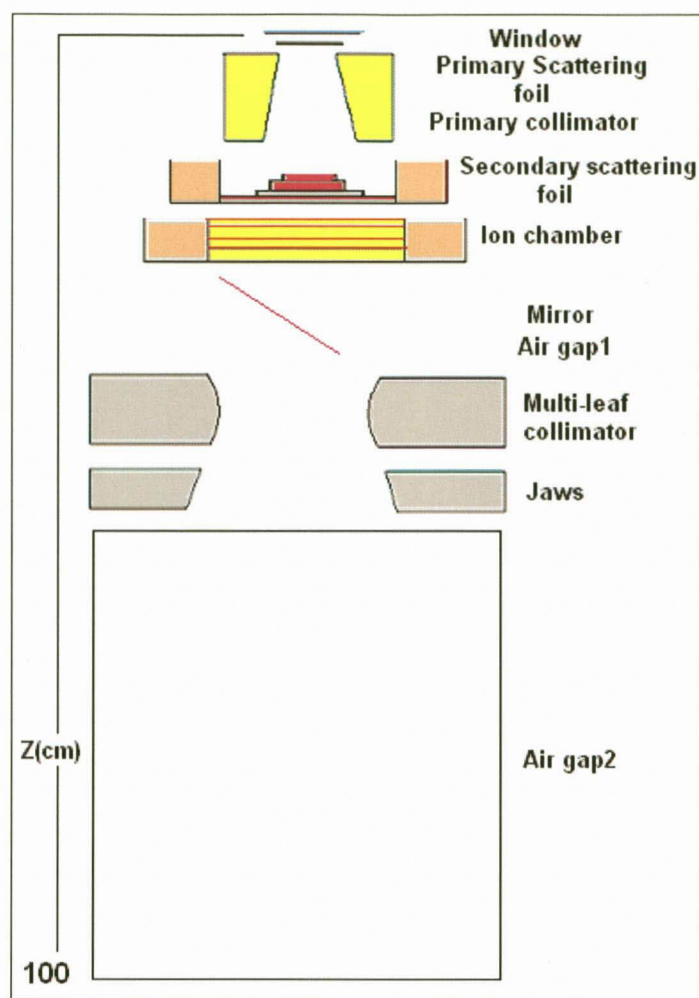


Figure 4.7. Schematic diagram (the physical geometry) of the main components of the Elekta Precise linear accelerator radiation head.

4.4.2 Monte Carlo simulation of the Elekta Precise linear accelerator

The EGS4/BEAMnrc code (version 2006) was used to simulate the output of the accelerator. The simulation was done on two PC computers: one a Pentium (IV), 2.41GHz processor with 14 Gbyte hard disk drive and 1.0 Gbyte of memory, and the other was a Celeron(R), 2.40 GHz processor with a 14 Gbyte hard disk drive and 512 Gbyte of memory.

Our EGS4/BEAM simulations consisted of two major stages (see figure 4.8); the first stage involved adjusting the primary electron beam parameters to match the beam data measured at 100cm SSD. In the second stage, these beam parameters were used to compute dose distributions at the treatment distance 350 cm SSD. Using the EGS4/BEAM code, two phase-space files were generated; one at the isocenter (100 cm SSD), and the other at the treatment plane (350 cm SSD). Each of the phase-space files contained spatial, spectral, and angular distributions of electrons, photons, and positrons.

In the first stage of the simulation, the accelerator head was simulated (from electron window up to the isocentre (100 cm SSD)). In the second stage transport of phase space particles from isocentre to the treatment plane (350 cm SSD) was simulated. This is more effective than combining everything in one simulation, because the radiation head simulation only has to be done once.

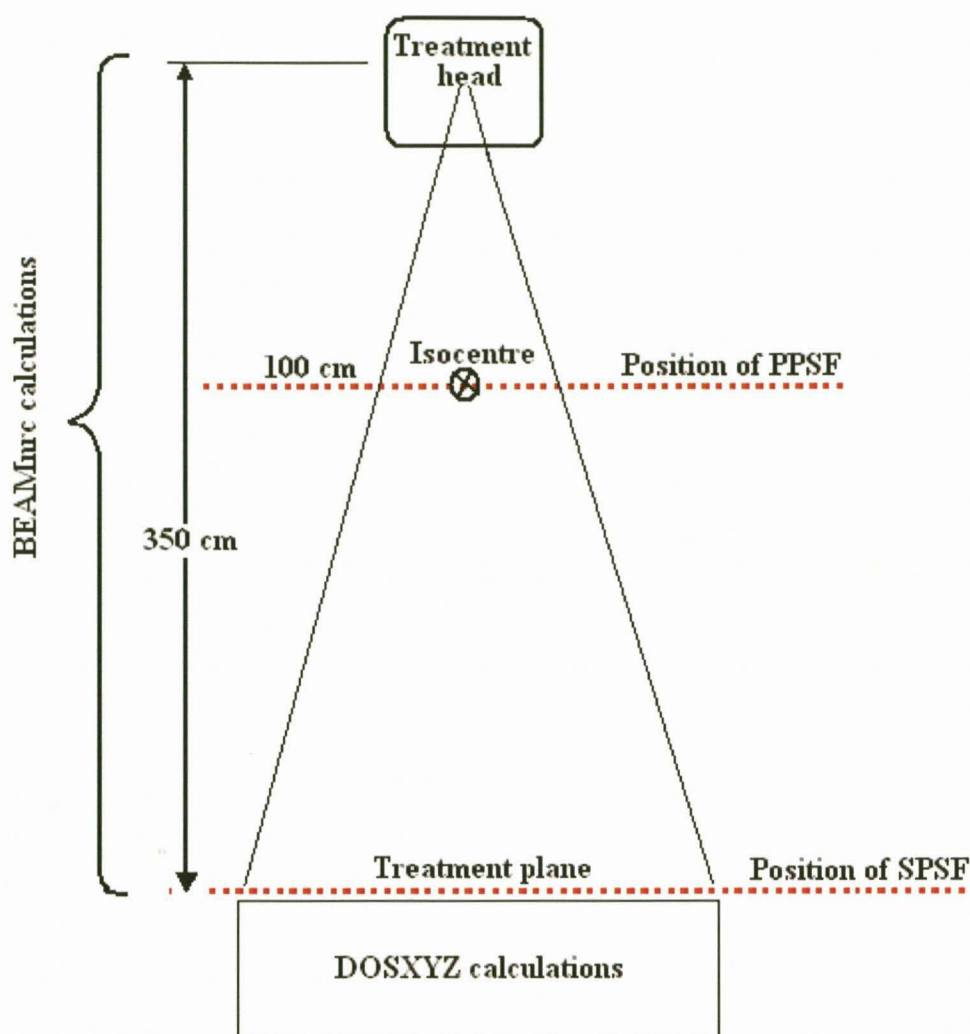


Figure 4.8. The flow of the BEAMnrc calculations

4.4.2.1 First stage of simulation

This stage involved modeling the head of the accelerator, from the electron exit window all the way down to the isocentre (100 cm SSD). Ten component modules (CMs) were used for the modeling and these are:

- CONESTAK used to model the electron window
- CONESTAK used to model the primary scattering foil
- CONESTAK used to model the primary collimator

- d) CONESTAK used to model the Secondary scattering foil
- e) CHAMBER used to model the ionization chamber
- f) MIRROR used to model the mirror
- g) SLABS used to model the air gap1
- h) MLCE used to model the MLC
- i) JAWS used to model the jaws
- j) SLABS used to model the air gap2

The **700icru** cross-section data for materials as stated in the PEGS4 data file were used in the modeling. Additional materials had to be added to the PEGS data file for modeling all components of the Elekta Precise accelerator correctly. Monoenergetic pencil beams of 4 and 6 MeV electrons were directed at the electron exit window. 100 million histories were used to generate the electron beams. Bremsstrahlung splitting and photon forcing were not used. The electron cut-off (ECUT) and photon cut-off (PCUT) values were set at 0.7 MeV and 0.01 MeV respectively in all CMs. The next subsections give brief descriptions of the individual CMs modeled.

a) The electron window

The “CONESTAK” CM was used for modeling the Electron window (Fig 4.9). The main function of the Electron window is to allow the accelerated electrons to exit from the accelerator wave-guide while maintaining the vacuum inside. The CM CONESTAK is used to simulate a stack of truncated cones (which can be cylinders). A cylindrical wall of arbitrary material surrounds the entire CM, just inside its outer cylindrical boundary. The radii of the cones must not decrease as the depth increases. The inner and outer conical regions of each layer have their materials specified separately. This CM can be also used to model scattering foils, primary collimators and many other components. This CM started at $Z = 0$ cm and this point also marked the origin of the coordinate system used in the modeling.

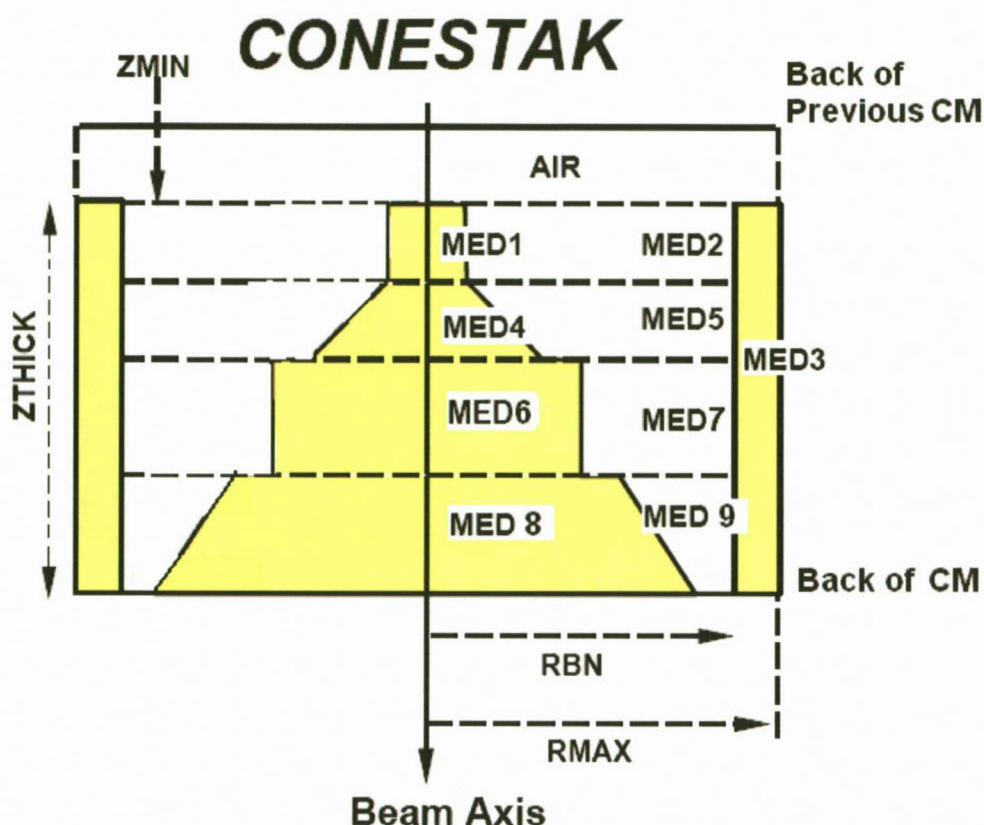


Figure 4.9. Component module CONESTAK with 4 layers of stacked coaxial truncated cones, one pair per layer, with a cylindrical wall surrounding (Adapted from Rogers et al, 2005).

b) The primary scattering foil

The “CONESTAK” CM was used for modeling the primary scattering foil. The main function of the primary scattering foil is to spread out the electron pencil beam striking it, as well as to get a relatively uniform electron fluence across the treatment field. This CM extended from $Z=1.01$ to 1.2 cm.

c) The primary collimator

The “CONESTAK” CM was used for modeling the primary collimator. The main function of the primary collimator is to confine the electron beam to a useful size. This

CM extended from $Z = 1.2$ to 11.6 cm. The CONESTAK was used because the primary collimator is cone shaped. The medium inside the cone is air.

d) The secondary scattering foil

The “CONESTAK” CM was used for modeling the secondary scattering foil. The main function of the secondary scattering foil is to create a much more uniform electron beam than can be produced with a single foil and to reduce the need to eliminate lower-energy scattered electrons from the electron applicator (Khan, 2003). This CM extended from $Z = 11.6$ to 15.0 cm.

e) The ionization chamber

The “CHAMBER” CM was used to model the ionization chamber (Fig 4.10). The chamber collects an ion current that is related to the dose output of the accelerator by a proper calibration. This CM is also used for modeling many other structures with cylindrical symmetry and centered on the beam axis. For the monitor chamber, both the front and back walls may have several layers of different materials. The side walls consist of three layers, a chamber wall, gap, and container wall. The central part of the chamber may consist of several air cavities separated by layers of other materials (serving as electrodes). This CM is also useful for central axis depth dose calculations in a phantom. Because there are fewer boundaries for the particles to cross in the side walls of this CM than in other cylindrical planar or voxel geometries, the computing efficiency can be greatly improved by using the electron range rejection technique (Rogers et al, 1995). This CM extended from $Z = 15$ to 17.3 cm.

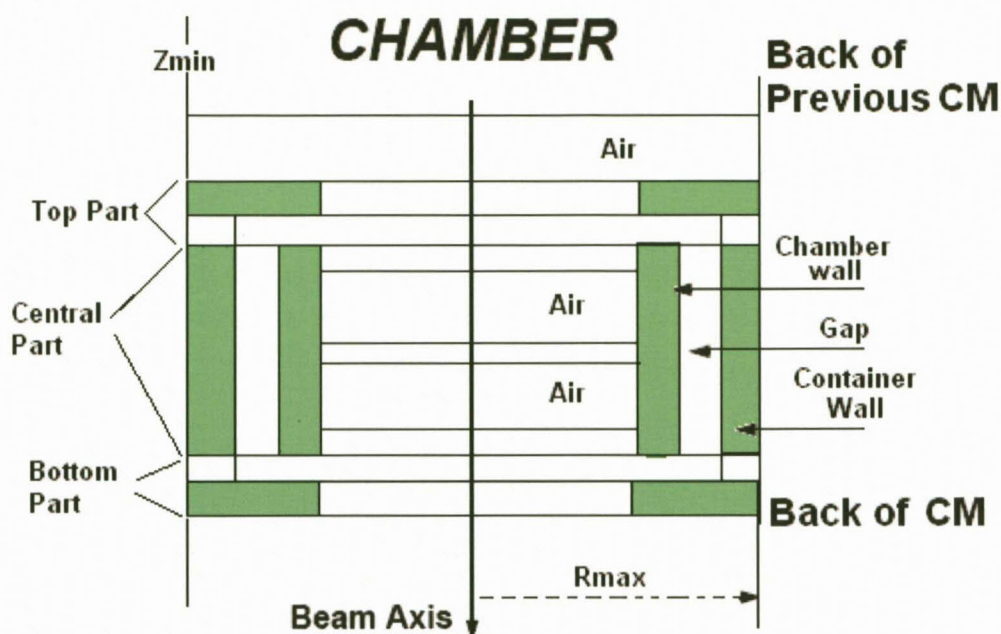


Figure 4.10. CHAMBER component module for an ionization chamber or any symmetric cylindrical- planar geometry (Adapted from Rogers et al, 2005).

f) The mirror

The "MIRROR" CM was used to simulate the mirrors in the accelerator (Fig 4.11). The main function is to reflect light from a light source for field localization during patient positioning (Khan, 2003). MIRROR CM can have an arbitrary angle with respect to the Z-axis. The number of layers and their thicknesses and materials in the mirror can be arbitrary. The mirror is surrounded by air. The MIRROR outer boundary is a square centered on the beam axis. This CM extended from $Z = 17.3$ to 26.85 cm.

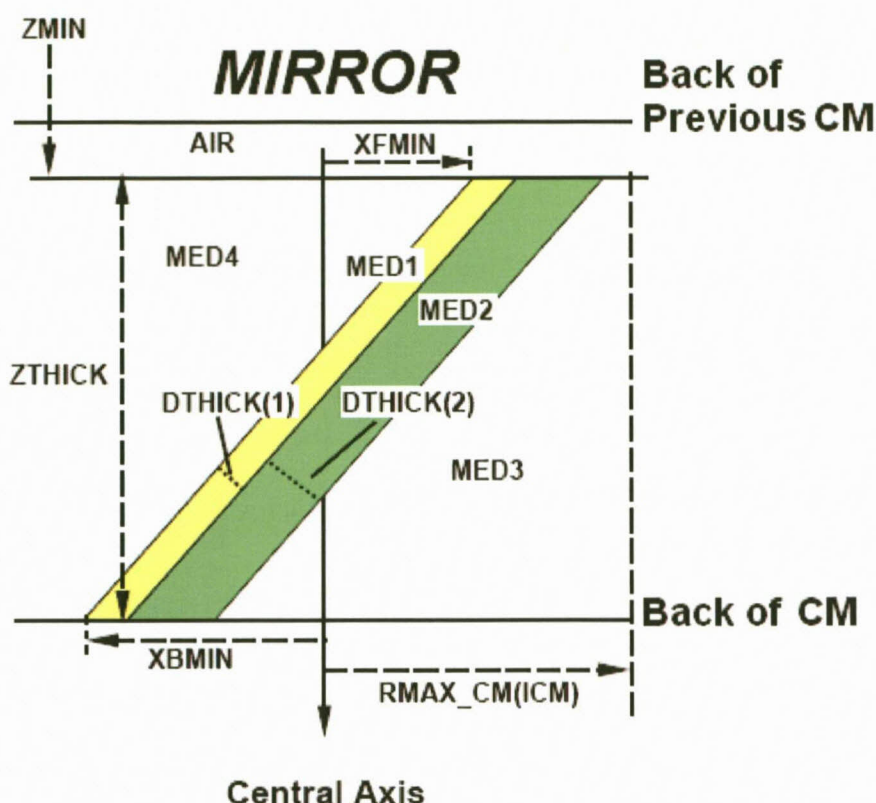


Figure 4.11. The MIRROR component module with layers of materials which are perpendicular to the z-axis, but rotated about a line parallel to the y-axis and truncated by two planes perpendicular to the z-axis (Adapted from Rogers et al, 2005).

g) The air gap between mirror and multi-leaf collimator

The “SLAB” CM was used to model the air gap between mirror and multi-leaf collimator (Fig 4.12). SLABS CM is also used for multiple slabs of arbitrary thickness and material, which are perpendicular to the z-axis. One single slab is a special case for SLABS. SLABS has square symmetry about the beam axis. This is because SLABS is often used to model the bremsstrahlung target in photon accelerators. The outer boundary is a square. The air gap extended from $Z = 26.85$ to $Z = 29.8$ cm, that is, a thickness of 2.95 cm.

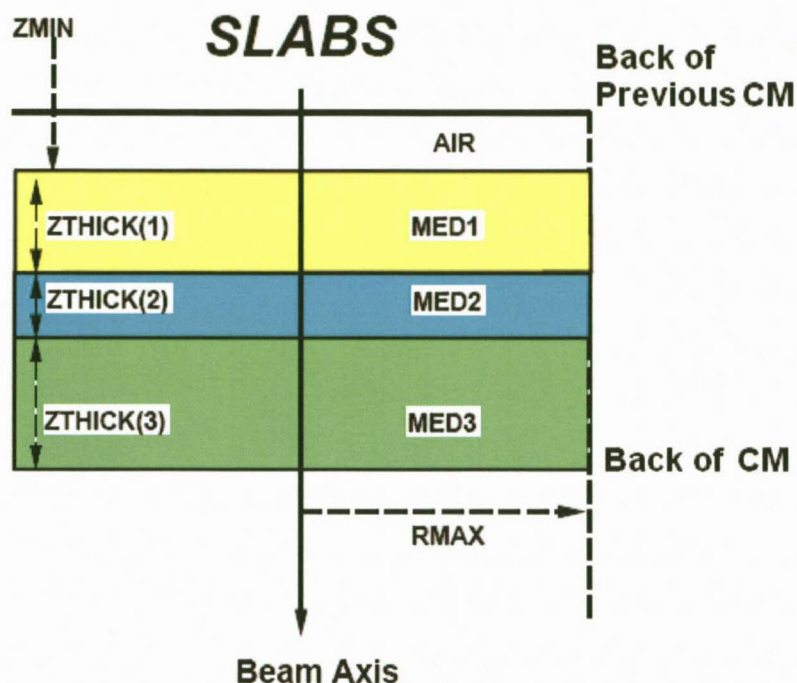


Figure 4.12. The SLAB component module with multiple slabs of arbitrary thickness and materials (Adapted from Rogers et al, 2005).

h) The multi-leaf collimator

The MLC was modeled for completeness, although the magnitude of its effect could not be estimated in advance.

The “MLCE” CM was used to model the multi-leaf collimators specific for Elekta machines (Fig 4.13). MLCE was designed as a variation of VARMLC (for Varian MLC) specifically for modeling Elekta MLC’s. The tongue-and-groove in VARMLC has been replaced by interlocking steps. Also, unlike VARMLC, all leaves are identical and the sides of the leaves are focused (always to $Z=0$) by tilting each leaf about an axis that runs down the centre of its top surface. The entire leaf bank can also be tilted for off-axis focusing. This CM extended from $Z = 29.8$ to 37.3 cm.

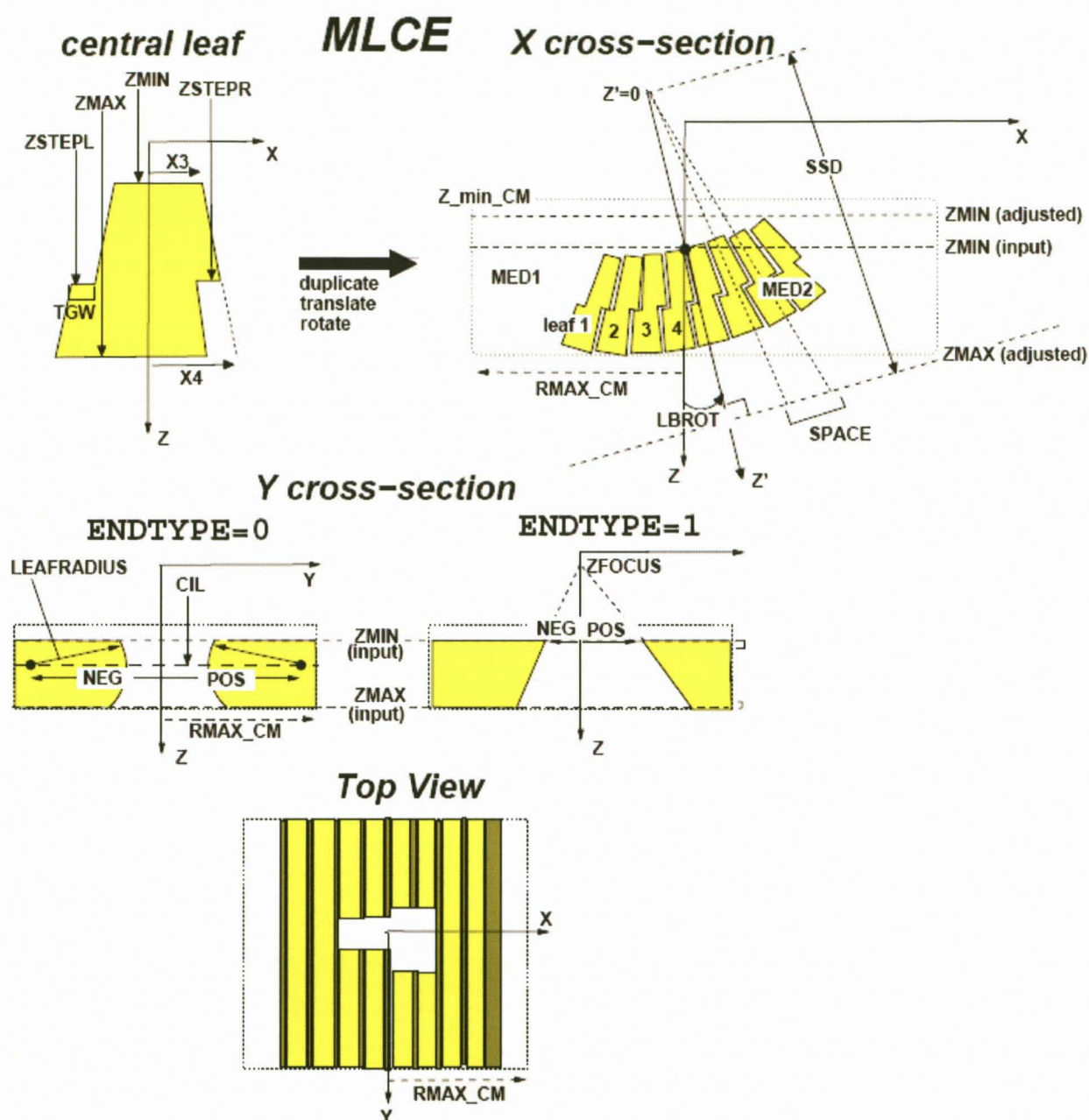


Figure 4.13. The CM MLCE which was used to simulate the multi-leaf collimator, with different cross-sections in X, Y (Adapted from Rogers et al, 2005).

i) The jaws

The “JAWS” CM was used for modeling the secondary adjustable jaws (Fig 4.14), whose main function is to collimate and define the field size at the isocenter (Khan, 2003). The accelerator jaws consist of upper (Y-direction) jaws and the lower (X-direction) jaws. The positive and negative lateral coordinates at the jaws positions were adjusted such that a square field size of 40x40 cm² could be obtained (at the isocenter). This CM extended from Z =37.3 to 50.9 cm.

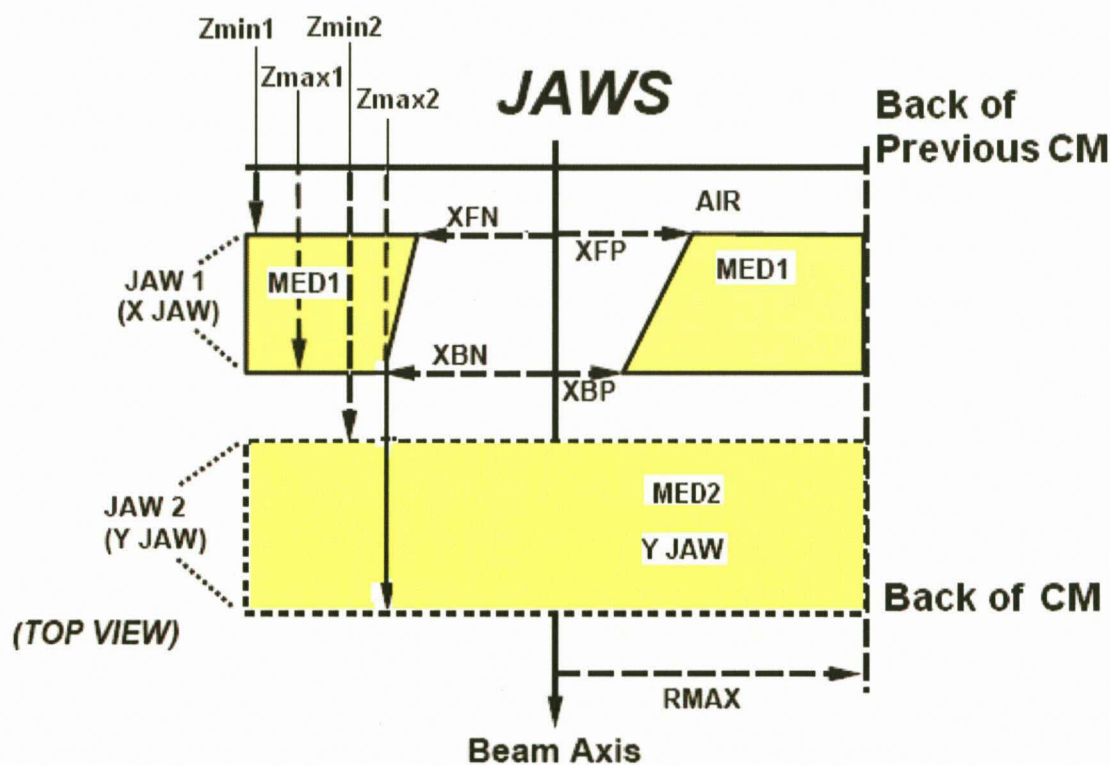


Figure 4.14. The JAWS component module for a case of paired x and y jaws which can be symmetric (hence the need to specify the XFP, XBN, etc., front and back x values in the positive and negative directions). The distances to the top and bottom surfaces of each pair of jaws are given relative to the z reference plane (z=0). The CM can model multiple sets of x or y jaws and and/or wedges (Adapted from Rogers et al, 2005).

j) The air gap between the jaws and the isocentre

The “SLAB” CM was used to model the air gap between the jaws up to the isocenter plane cm. This air gap extended from $Z = 59.9$ to $Z = 100$ cm, that is a thickness of 40.1 cm. In other words the PPSF was created at $Z = 100$ cm at isocentre.

These CMs involved the first simulation stage of the accelerator, and at this stage of simulation about 1×10^8 histories were run. To avoid the discrepancies in the simulation, histories were divided into ten batches in order to be run individually and after that the PSFs generated from each batch were combined together to get the total number.

Each batch consists of about 10 million histories. For 4 MeV each batch scored about 3.4×10^5 particles in the phase space file. The CPU time for the batch (10 million histories) was 1.26 hour, which gives the rate of 7.9×10^6 histories per hour. For 6 MeV each batch scored about 5.2×10^5 particles in the phase space file. The CPU time for the batch (10 million histories) was 1.38 hour that gives the rate of 7.2×10^6 histories per hour. Simulation for the total phase space files for the 4 and 6 MeV energies typically took 12-14 h and 13-16 h CPU time on our 2.4GHz Windows based computers. More details about simulation are shown in the results chapter.

Each of the PSFs was used as source file for the DOSXYZ program to obtain the beam data in the water phantom. Also the same PSFs were used as sources for simulation of the second stage to obtain the dose distribution for the CT based models using the CTCREATE program.

4.4.2.2 Second stage of simulation

In this stage the output of the accelerator was modeled from the previous scoring plane that was located at the isocenter, which is at $Z = 100$ cm, up to 350 cm SSD. This consists of an air slab with a thickness of 250 cm. Only one CM (SLAB) was used to model this air gap.

The primary PSFs collected in the first stage were used as the source input for this stage. Bremsstrahlung splitting, Russian roulette or photon forcing were not used. The values for ECUT and PCUT as used in the first stage were maintained (0.7 MeV and 0.01 MeV respectively). The simulation in this stage resulted in a short simulation time compared with the first stage, because just the air gap component module was modeled.

4.4.3 Analysis of the phase space file

The obtained PSFs from the simulation of the Elekta Precise linear accelerator at a distance of 100 cm from the electron exit window, and at the treatment plane at 350 cm SSD were analyzed using the BEAMDP program (Ma and Rogers, 2005). The electron fluence, energy fluence, spectral distributions and angular distributions were obtained in this study. More detailed discussion of the results are presented in chapter five, section (8.3).

4.4.4 Determining primary electron beam parameters

To find the parameters of the electron beam incident on the exit window, we followed published procedures by matching our calculated depth doses (PDDs) and cross-beam profiles to our measurements (Pavón et al, 2003 and Sung et al, 2005). We started using beam parameters from the scientific literature where the simulations of linear accelerators were modeled, and made adjustments until the best match was found (fine-tuning). We assumed the electrons incident on the exit window to be monoenergetic and also investigated parallel circular beams with different energies having Gaussian radial distributions of full width at half-maximum (FWHM) of 0.05 cm. The beam parameters that yielded the closest agreement between simulations and measurements were considered as the true beam parameters and used for all subsequent calculations.

4.4.5 DOSXYZ – Calculation of dose distribution in 3D phantoms

The DOSXYZ code was used for the calculation of the absorbed dose in a water phantom. This allowed calculation of percentage depth doses and cross beam profiles for the large field size for the comparison with measurements. The PSFs generated by the

BEAM program were used as source input files for the DOSXYZ code. The scoring plane for the PSFs was at the surface of the phantom.

4.4.5.1 The construction of the water phantom model

For MC calculation of the beam data two water phantom models were constructed: one at the isocentre and the other at the treatment plane. The isocentre (100 cm SSD) and the treatment plane (350 cm SSD) were made to coincide with the isocenter for the DOSXYZ simulation at $Z = 0$ on the surface of the water phantom for each. These phantoms were constructed in such a way that the **X** by **Y** by **Z** dimensions were $200 \times 100 \times 24 \text{ cm}^3$ and $400 \times 200 \times 24 \text{ cm}^3$ respectively. For the phantom at the isocentre; the X direction consisted of one region with boundaries in cm of $-100 \leq X \leq +100$. There were 200 sub-regions of equal widths, each 1.0 cm. Setting the voxel dimension to 1.0 cm. The Y-direction consisted of four regions; two regions represent the outer boundaries in cm of $-50 \leq Y \leq +50$ and the other two regions with equal widths of 0.5 cm for each. The Z-direction was made up of two regions with boundaries (in cm) of 0, 6, and 24 cm. There are 24 and 36 regions in the first and second region respectively. Their corresponding widths were 6 and 18 cm respectively. The depth increment in the first region was 0.25 cm and in the second region was 0.5 cm.

For the water phantom at the treatment plane the boundaries in the X and Y direction are changed, but the voxel dimensions are the same as the one at the isocentre. Figure 4.15 shows the schematic diagram of the water phantom used in DOSXYZ calculations.

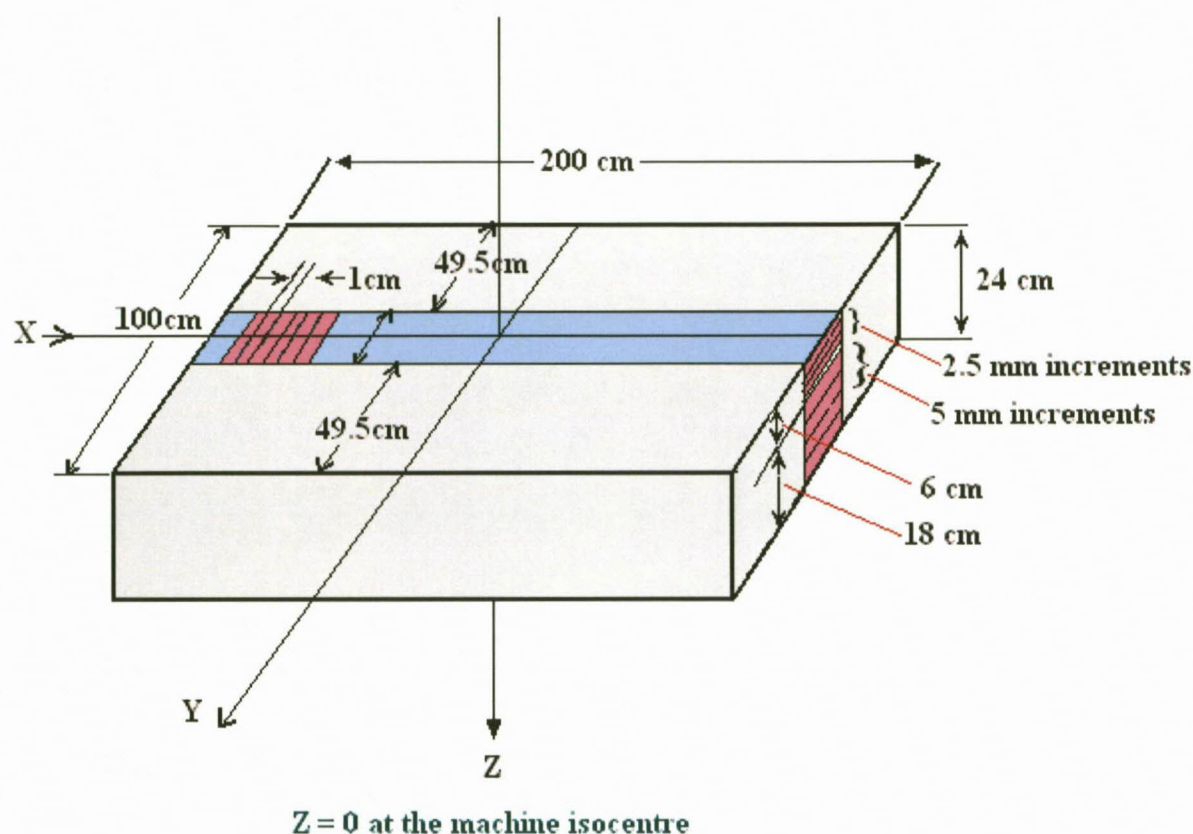


Figure 4.15. The 3D water phantom used for the beam data calculations.

4.4.5.2 Transport control parameters

The electron and photon energy cut-off (ECUT and PCUT) was set at 0.700 and 0.01 MeV respectively, and the **700icru** PEGS4 data file was used for the supply of cross section data for water and air media. The PRESTA algorithm was set “on” during simulations, because that proved to increase the history simulation rate quite effectively (Antolak et al, 2002). The source was a full PSF from stage one incident on the front face. The number of histories was chosen so as to reduce the percentage error to less than two percent in all voxels in the field. This required about 600 million histories and the simulation rate was in the order of 7.5×10^7 histories per hour on a 2.41 GHz Pentium IV PC.

4.4.5.3 Number of histories and uncertainty

As we mentioned previously in section 3.7, the standard deviation in any Monte Carlo process is inversely proportional to the square root of the number of histories used (Bielajew and Rogers, 1988) therefore:

$$\sigma = \frac{\kappa}{\sqrt{N}} \quad 4.1$$

Where σ is the standard deviation and N is the number of histories.

If we let the standard deviation σ_1 and σ_2 correspond to the number of histories N_1 and N_2 respectively, then equation 4.1 can be rewritten as

$$\sigma_1 = \frac{\kappa}{\sqrt{N_1}} \quad \text{and} \quad \sigma_2 = \frac{\kappa}{\sqrt{N_2}} \quad 4.2$$

Equation 4.2 can be simplified to

$$\frac{\sigma_1}{\sigma_2} = \sqrt{\frac{N_2}{N_1}} \quad 4.3$$

From equation 4.3, two observations can be made:

- To find the number of histories that are needed to reduce the standard deviation by 50%, we let σ_2 be equal to $\sigma_1 / 2$, and substituting in Equation 4.3:

$$\frac{\sigma_1}{\sigma_1/2} = \sqrt{\frac{N_2}{N_1}} \Leftrightarrow 2 = \sqrt{\frac{N_2}{N_1}} \Leftrightarrow N_2 = 4 N_1 \quad 4.4$$

Thus four times more histories are required to reduce the standard deviation by half.

-To find the number of histories that are needed to reduce the standard deviation to within 1%, given the standard deviation σ_1 found with the trial run of N_1 histories we let σ_2 be equal to 1% and substitute in the equation 4.3:

$$\frac{\sigma_1}{1} = \sqrt{\frac{N_2}{N_1}} \quad \Leftrightarrow \quad N_2 = N_1 \cdot \sigma_1^2 \quad 4.5$$

Thus the number of histories required to reduce the standard deviation to within 1% is equal to the initial number of histories multiplied by the square of the uncertainty.

From the above equations we can establish the appropriate number of histories to be used for the DOSXYZ program that will give a standard deviation which is within less than 2%. Several parameters were analyzed after simulation e.g. number of histories in simulation, histories simulation rate, CPU time, and computer memory space for each. Full descriptions of simulation parameters are discussed in the results in chapter five.

The output file generated by DOSXYZ consists of a 3D dose array. The file is an ASCII file that can be read and displayed after writing suitable computer programs. After running the DOSXYZ program, graphs of depth dose and cross beam profiles were plotted. These profile data were compared with similar data obtained by measurements.

4.5 Comparison of Monte Carlo and measured profile data

The calculated beam data using DOSXYZ MC code and that obtained by the film and ionization chamber measurements were compared to each other. The PDDs were measured on the central axis for the two energies and by both methods. In order to obtain percentage errors less than 2%, the data were sampled in increments of 0.25 cm for the MC simulations up to a depth of 24 cm. The ion chamber measurements were done in increments of 0.15 cm, corresponding to the thickness of the available polystyrene sheets, up to a depth of 20 cm. Measurements were also performed using EDR2 film. The

measured depth doses data were then normalized to 100% at d_{\max} for both. MC and ion chamber and the corresponding data were plotted on the same graph for comparison. The data for cross plane profiles were also sampled across the central axis with increments of 0.5 cm for MC and 1.0 cm for the chamber. In both cases the data were obtained at the maximum depths of each associated energy. All data were normalized to 100% relative to central axis dose, for both the MC method and chamber measurements. Corresponding data were then plotted on the same graph for comparison (see the results).

4.6 Monte Carlo simulations on Rando phantom

4.6.1 CT based simulations

In order to compare the film dose distributions with the MC dose distributions, CT scans of a Rando phantom were made on a Siemens Somatom HiQ-S CT scanner. To get adequate spatial resolution of the dose distribution, which occurs mostly in a few mm below the skin surface, the slice dimension was $0.1 \times 0.1 \times 1.0 \text{ cm}^3$, and there were 95 slices. All the CT slices making up the whole Rando phantom were transferred to a 2.41 GHz Pentium IV PC on which the simulations were carried out.

4.6.2 CT Based Phantoms / CTCREATE

4.6.2.1 Data input

As discussed in section (3.11), the CT based Phantoms/ctcreate program is a DOSXYZ option that allows calculation of dose distributions in CT data sets. CTCREATE can be used to convert CT data from certain formats, including the CADPLAN format, which was used here. In the CADPLAN format, each CT slice is stored as a separate file. To read the slices in CTCREATE all the slices have to be listed in one file (in order of increasing or decreasing Z) containing the full names of the files that make up the CT slices.

4.6.2.2 Conversion of CT number to density in CT Based Phantom/ CTCREATE

The input beam data for patient models usually consist of a set of CT slices with the patient information expressed in terms of CT numbers. The conversion of these CT numbers into material properties is one of the main factors that determine the accuracy of the patient dose calculations (Du Plessis, 1999). Thus, before the data can be used directly for dose computation they have to be converted to electron densities relative to that of water.

For a patient model to be used in the DOSXYZ MC code, each voxel (volume element) has to be associated with a specific material entry in a PEGS4 cross-section file with a specific name and physical density (Walters et al, 2005). The PEGS4 data file contains the relevant cross section data for each material in the patient model. In the BEAM/DOSXYZ MC codes, a number of materials were used for the conversion of each voxel's CT number into electron density. The **700icru** cross-section data for materials in the PEGS4 data was used in the simulation.

Figure 4.16 shows the ramp used for converting CT values of the materials to density in CTCREATE. The density is assigned using linear interpolation between the material's density limits (Walters et al, 2005), using the equation:

$$\rho_{i,j,k} = MD.LB_{i_mat} + \left(\frac{MD.UB_{i_mat} - MD.LB_{i_mat}}{MCT.UB_{i_mat} - MCT.LB_{i_mat} - 1} \right) * (MCT.UB_{i_mat} - CT_{i,j,k}) \quad 4.6$$

Where:

- MD.LB is material density lower bound
- MD.UB is material density upper bound
- MCT.UB is material CT upper bound

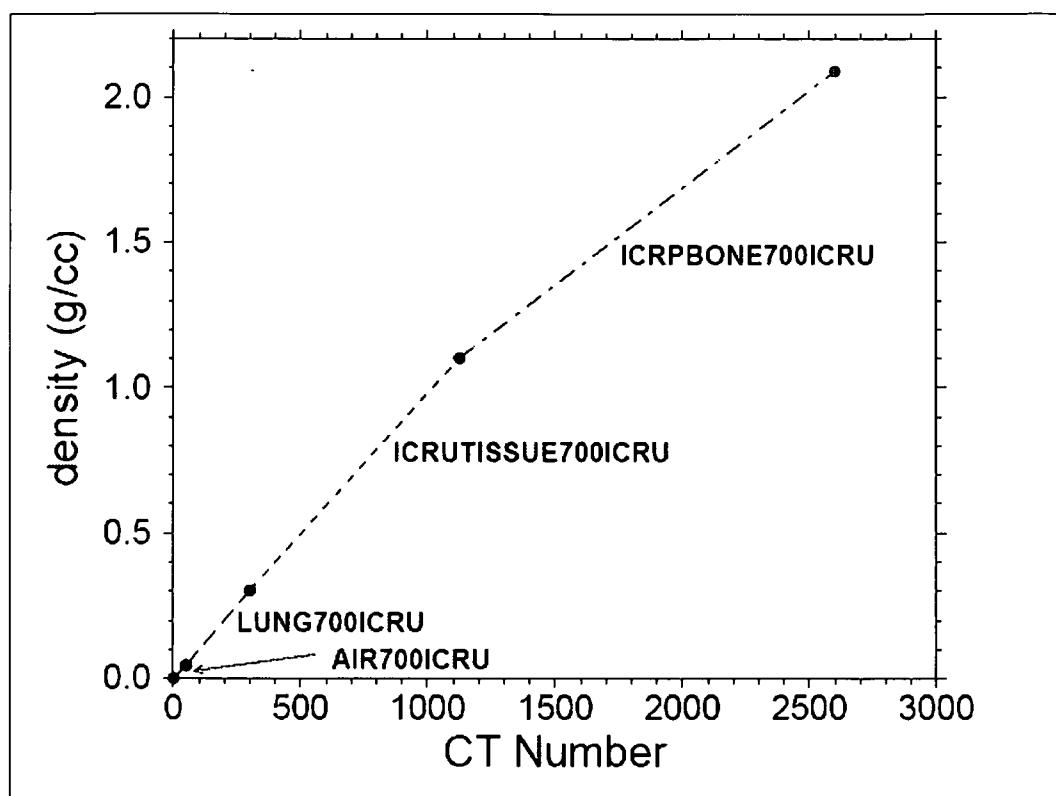


Figure 4.16: The default ramp for converting CT values to material and density in CTCREATE. (Adapted from Walters, 2005).

After running of the CT phantom/CTCREATE program, the CT phantom information is written into a file X.egs4phant, where X is the file name of the CT data set. DOSXYZ was run on these CT phantom files using any appropriate phase space file from the BEAM code as the source input file.

4.7 Comparison of measured and Monte Carlo dose distributions

4.7.1 Film registration

The method used for calculation of the film dose distribution was described in “Multiple field measurements” in section (4.3.3). The EDR2 films were introduced into four different slice levels along the length of the Rando phantom; Level I: head, level II: thorax, Level III: navel and Level IV: pelvis level as shown in figure (4.4). These films were scanned using the Wellhöfer WP102 densitometer to determine the isodose distributions. The output-scanned data of the films were stored in a 2D array with a scan spacing 2 mm in the cross-plane direction for each level. The dose matrices consist of arrays of different dimensions for each slice. These dose array files were converted to ASCII files in order to be read and displayed on a PC.

4.7.2 DOSXYZ dose distributions

For the MC dose distribution of this technique the whole Rando phantom was irradiated using six dual fields in one session using a single beam source option of DOSXYZ. This dose distribution was analyzed for the different slices at the levels of the Rando phantom that corresponded with the film positions during the actual irradiation. The dose distribution from the DOSXYZ output file is a floating-point array of i_{\max} by j_{\max} by k_{\max} values, where i_{\max} , j_{\max} and k_{\max} are the number of voxels in the X, Y and Z direction. The voxel size was always set to 1.0 cm in the Z direction since the CT slices were also acquired at 1.0 cm intervals and for the x and y directions it was set to 0.1 cm. Each time the dose distributions were analyzed at one particular slice of interest and thus the dose distribution is an array of i_{\max} by j_{\max} values. A program was written in IDL (www.itlvis.com) to display the dose distributions.

4.7.3 The CT image

The original CT image data are in an integer array of 256x256 voxels obtained from the CADPLAN HP Unix work station. Thus, to be read and displayed on a PC the bytes had

to be swapped. For the comparison of the DOSXYZ and film results, the dose distributions were displayed (overlaid) on the CT image.

4.7.4 Normalization of the dose distributions

For comparison to be meaningful, the normalization in both the film data and DOSXYZ should be the same. The film dose was normalized at the calibration point, which is located near to the skin at the navel level of the Rando phantom (according to the AAPM TG-32 protocol recommendation). The average dose in 9 voxels was calculated at that calibration point and then the complete dose distribution was normalized relative to that average dose. A program was written in IDL to read, normalize and display the dose distributions. Thus the DOSXYZ dose distributions had to be normalized in a similar way to the film data.

5 RESULTS AND DISCUSSION

5.1 Introduction

In the previous chapter the methods used for carrying out the experimental procedures and the MC simulation of the Elekta Precise accelerator and calculation of the dose distributions with MC methods were presented. In this chapter the results that were obtained for the experimental measurements and the MC simulation are given.

5.2 HDRE - special procedures mode

The operating parameters including linear accelerator dose and dose rate with the collimator setting at its maximum for the HDRE mode were investigated. The HDRE mode provides an adequately high dose rate with 4 and 6 MeV electrons at the patient treatment plane located at several meters distance e.g. 3 – 3.5 m. This was investigated through several measurements of the output of the machine at different distances as shown in figures 5.1.a, 5.1.b and table 5.1.

We define the output factor of the machine in the high dose rate mode as follows:

$$OF_{HDRE} = \frac{(D_{SSD})_{HDRE}}{(D_{95})_{Normal-dose-rate}} \quad 5.1$$

Where $(D_{SSD})_{HDRE}$ is the dose measured at 350 cm SSD in HDRE mode, for a single dual field.

$(D_{95})_{Normal-dose-rate}$ is the dose measured at 95 cm SSD, using 10x10 cm² applicator at normal dose rate.

Table 5.1 shows the results of OF measurements for the two energies at 100 and 350 cm SSD. It is clear from the results that the dose rate at 350 cm SSD is comparable with the dose rate at 100 cm SSD in normal mode ($\pm 86\%$ for 4 MeV, $\pm 77\%$ for 6 MeV).

Figures 5.1.a and 5.1.b show the output factor as a function of the distance for 4 and 6 MeV respectively. The solid lines represent a power function fit to the data points. The dose rate of the machine in HDRE mode at the isocentre is approximately ten times that in the normal treatment mode (Precise operators manual, 2003). Also the graph shows that the output of the machine decreases at a lower rate at extended distances and there is a relatively small difference in the output factor values between distances of 3 to 3.5 m. This is an advantage in implementing a TSET technique because of the reduced influence of variation of SSD at the patient skin surface.

Energy	OF (350 cm SSD)	OF (100 cm SSD)
4 MeV	(0.862 ± 0.004)	(0.898 ± 0.003)
6 MeV	(0.767 ± 0.010)	(0.907 ± 0.001)

Table 5.1. Output factors (OFs) for 4 MeV and 6 MeV measured at 350 cm SSD and at 100 cm SSD with the HDRE applicator. OFs are expressed relative to the dose at d_{max} at 95 cm SSD with a 10x10 applicator at normal dose rate (the set-up for normal beam calibration).

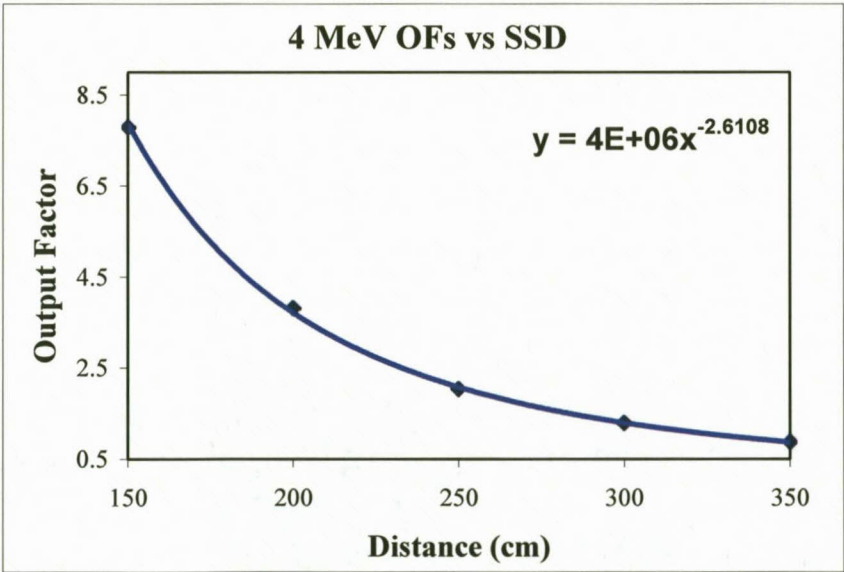


Figure 5.1.a. Variation of output factor with SSD for 4 MeV.

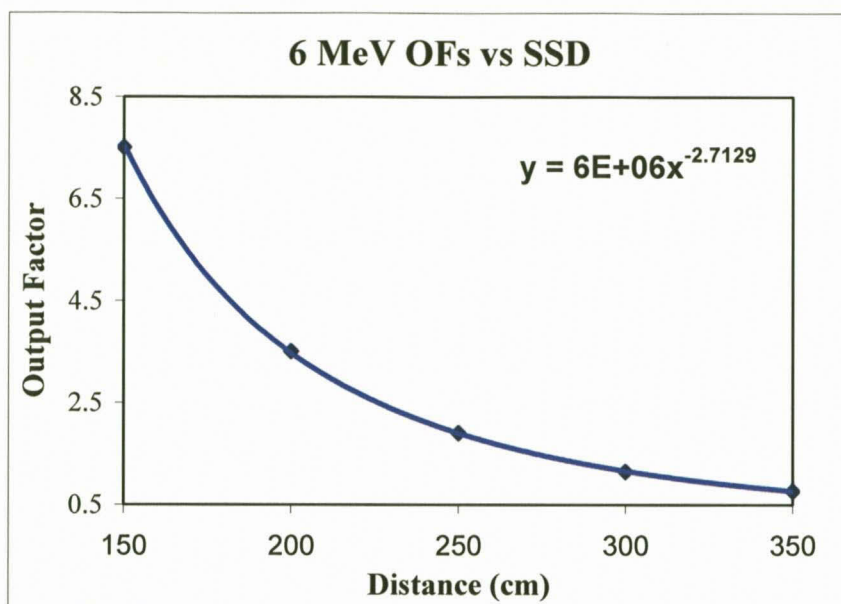


Figure 5.1.b. Variation of output factor with SSD for 6 MeV

5.3 Single field depth dose measurements

The percentage depth doses for a single vertical beam were measured at the machine isocentre (100 cm SSD) with gantry angle 0° and for a single horizontal beam at the treatment plane (350 cm SSD) with the gantry angle 90° , using both the ionization chamber in a polystyrene phantom and with Kodak EDR2 film. Figures 5.2 and 5.3 show the measured percentage depth dose curves.

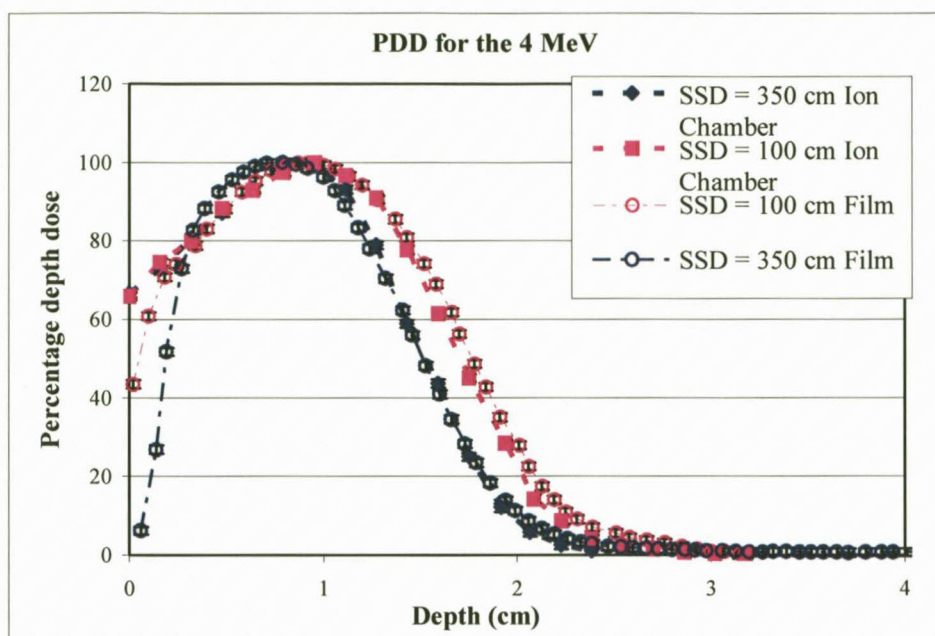


Figure 5.2: Percentage depth dose curves measured with ionization chamber and EDR2 film at SSD = 100 cm and SSD = 350 cm for the 4 MeV electrons.

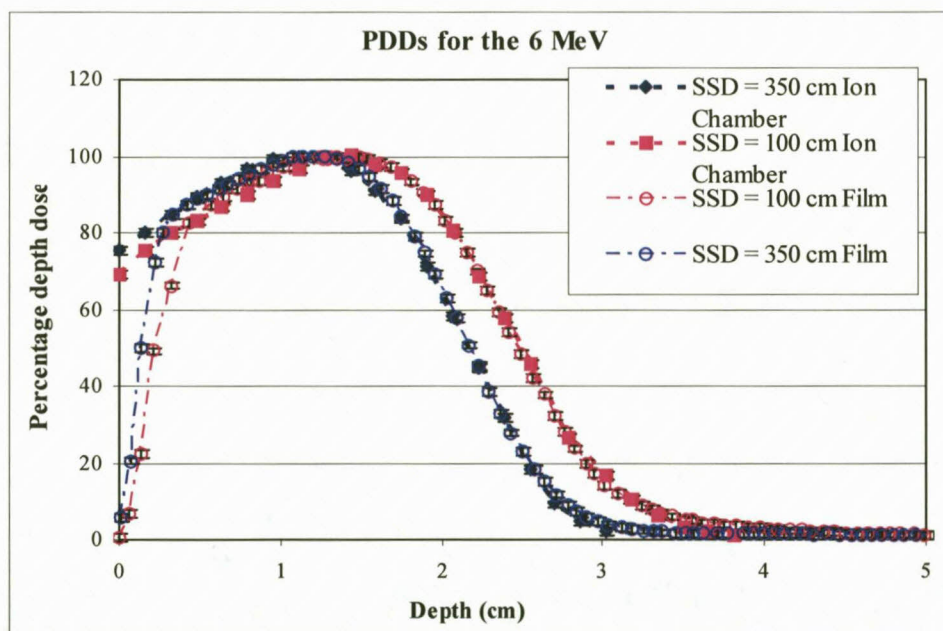


Figure 5.3: Percentage depth dose curves measured with ionization chamber and EDR2 film at SSD = 100 cm and SSD = 350 cm for the 6 MeV electrons.

The peak of the dose distribution moves to shallower depths as the SSD increases due to the divergence of the beam and energy loss in air. The ion chamber measured values of d_{\max} agree quite well with the film data. For the ion chamber measurements the surface dose increases with increasing SSD for 6 MeV, but for 4 MeV the surface dose is almost constant. The precision of the measured data with the ion chamber is within about 1 mm. This corresponds to about 3% change in dose.

For the film measurements the characteristic curve for Kodak EDR2 film is shown in Figure 5.4. Figures 5.2 and 5.3 show the central axis EDR2 film percentage depth dose compared to ion chamber percentage depth dose data for 4 and 6 MeV electron energies respectively. The entrance dose starts from a depth greater than zero because of the 4 mm aperture diameter of the film densitometer detector.

Tables 5.5 and 5.6 (page 136) show a numerical comparison of the beam parameters for the two energies shown in figures 5.2 and 5.3. As expected there is excellent agreement in the R_{50} and R_p depth for the ion chamber and film data. For comparison the difference in d_{\max} , R_{50} and R_p between the ion chamber and the film is less than 1 mm.

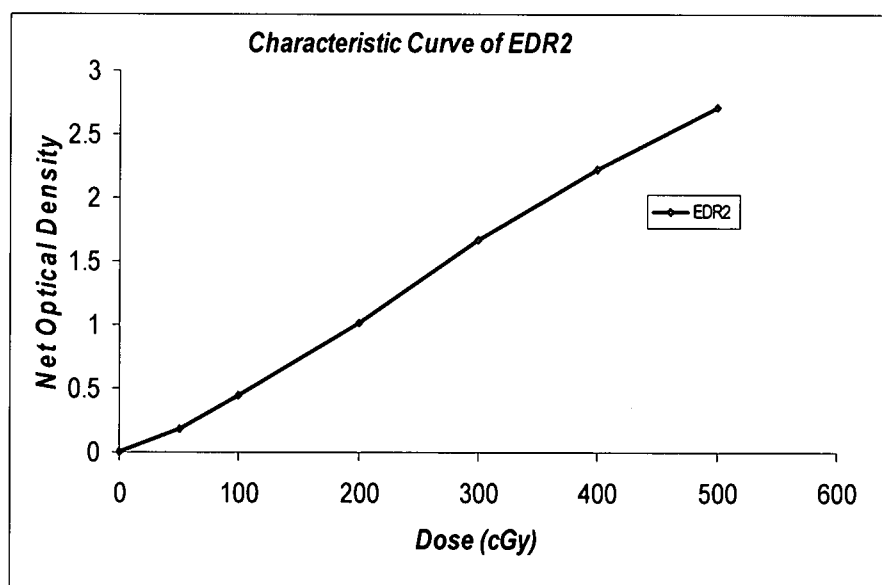


Figure 5.4. Characteristic curve of the EDR2 Film. The curve shows the approximate linear relative dose response for Kodak EDR2 film. The film will saturate in a direct exposure of approximately 700 cGy.

5.4 Single field profile measurements

Figures 5.5 and 5.6 show the measured single beam profile at the isocentre (100 cm SSD) and at the treatment plane (350 cm SSD) for the 4 and 6 MeV.

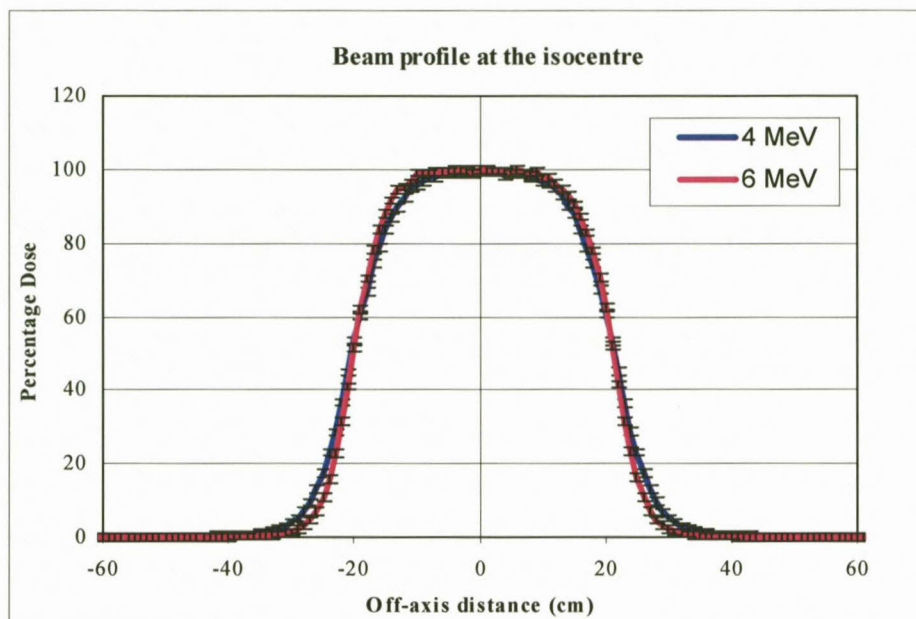


Figure 5.5. Beam profiles measured in a solid water phantom in the horizontal direction at the isocentre (100 cm SSD) for 4 and 6 MeV energies at a depth of d_{\max} .

The beam profiles for both energies at 100 SSD have a good uniformity compared to other published results (Peters et al, 1995, and Sung et al, 2005). This is probably due to the dual scattering foil design of the Elekta Precise machine. The beam profiles at 100 SSD of the 6 MeV beam have a better uniformity than those of 4 MeV due to less scattering in air of the higher energy (6 MeV) compared to lower energy (4 MeV). For the TSET single beam profile (350 SSD) the measured 90% beam widths for 4 and 6 MeV energies are 65.1 ± 1.1 and 69.8 ± 1.6 cm respectively. For the 60% beam width there is little difference between 4 and 6 MeV energies.

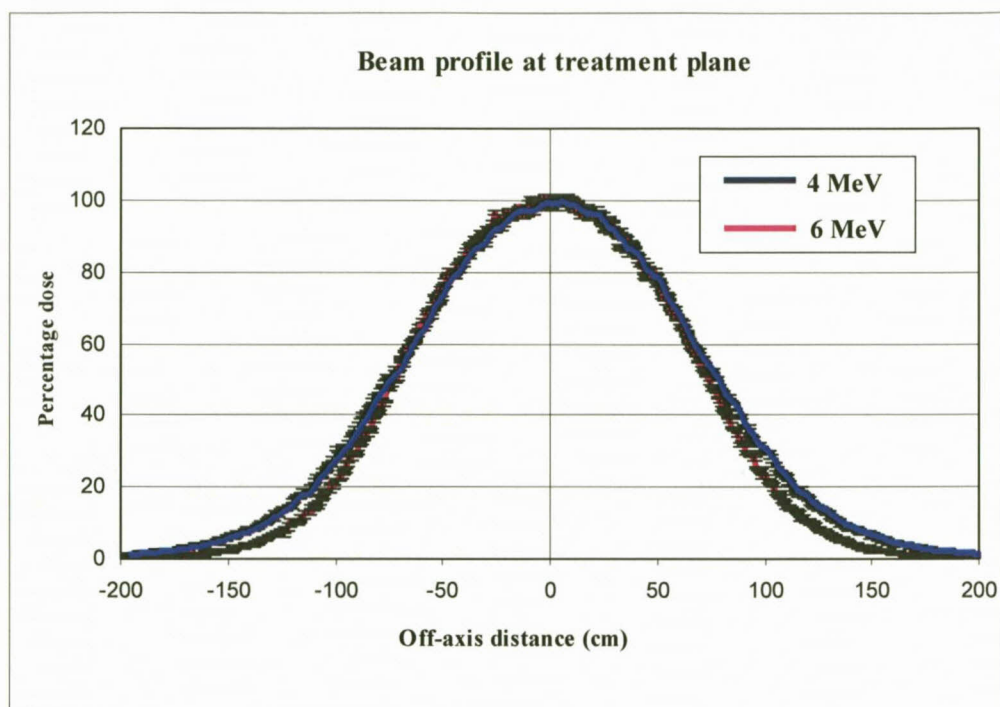


Figure 5.6 Beam profiles measured with ion chamber in the horizontal direction at the treatment plane (350 cm SSD) for 4 and 6 MeV energies at a depth of d_{\max} .

5.5 Multiple field measurements

5.5.1 Depth doses and beam parameters

Figures 5.7 and 5.8 show depth doses curves measured in solid water for six dual fields and for a single dual field for 4 and 6 MeV respectively.

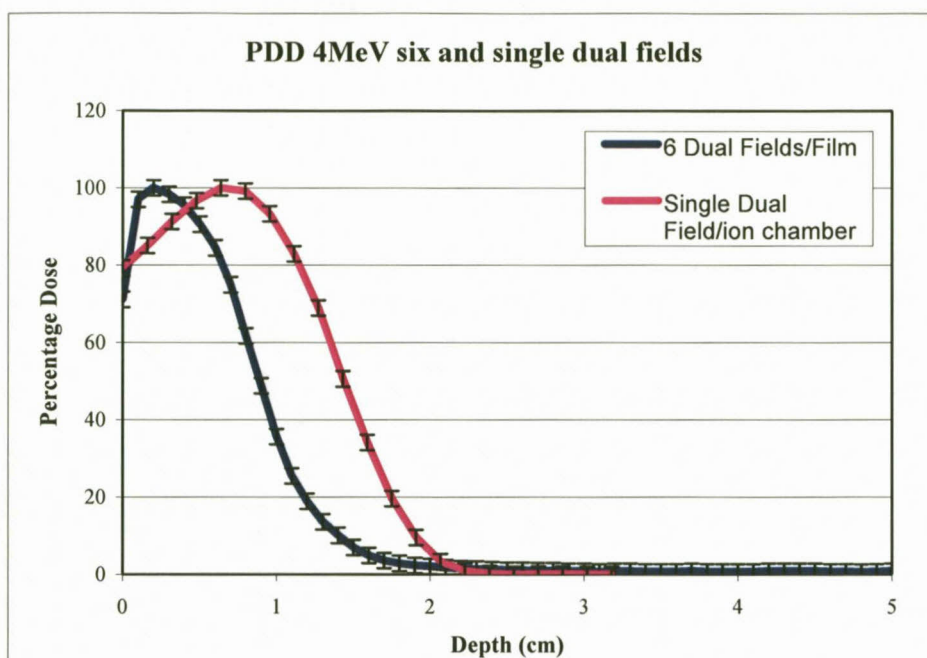


Figure 5.7. 4 MeV electron depth doses. The depth dose obtained with ion chamber for single dual field compared with the depth dose obtained with film in solid water phantom that is obtained with six- dual fields.

The corrected depth doses in Solid Water for the two different energies as shown in the figures are obtained with the derived mean energies at the surface of the phantom. These curves correspond to the combined effect of two angulated beams (14° and 16° on both sides of the horizontal axis for 4 and 6 MeV respectively. These angles were calculated from Monte Carlo). The results of the single dual fields were used to determine the position of dose maximum (the calibration depth) for the absolute calibration. This was found to be 6 and 11 mm for 4 and 6 MeV energies respectively. The d_{\max} values for the six dual fields were found to be 2 and 3 mm and the R_{80} values were found at 7 mm and 9 mm for 4 and 6 MeV respectively.

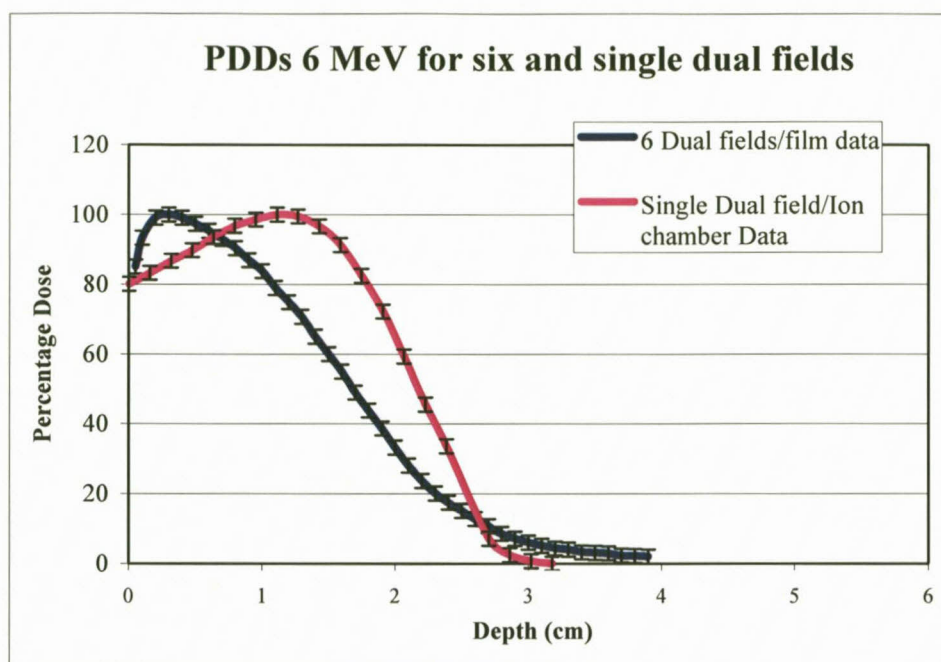


Figure 5.8. 6 MeV electron depth doses. The depth dose obtained with ion chamber for single dual field compared with the depth dose obtained with film in solid water phantom that is obtained with six- dual fields.

For the TLD measurements, both the cylindrical and the Rando phantom were used to verify the required monitor units. TLD dosimeters were taped to the surface of the phantoms with adequate buildup added for 4 and 6 MeV at d_{max} . For the Rando phantom the difference between TLD results and prescribed dose was about 4% as well as for the cylindrical phantom the difference was about 3.5%.

Figures 5.9 and 5.10 show the variation of the electron beam parameters R_{max} , R_{80} and R_{50} for six dual fields for 4 and 6 MeV respectively. The average values of the parameters were determined from PDD curves measured at 10 degree intervals around the circumference of the film, perpendicular to the surface. The average values are represented by solid lines, the error in the average values represented by the dashed lines and the percentage standard deviation are shown next to the brackets for each parameter.

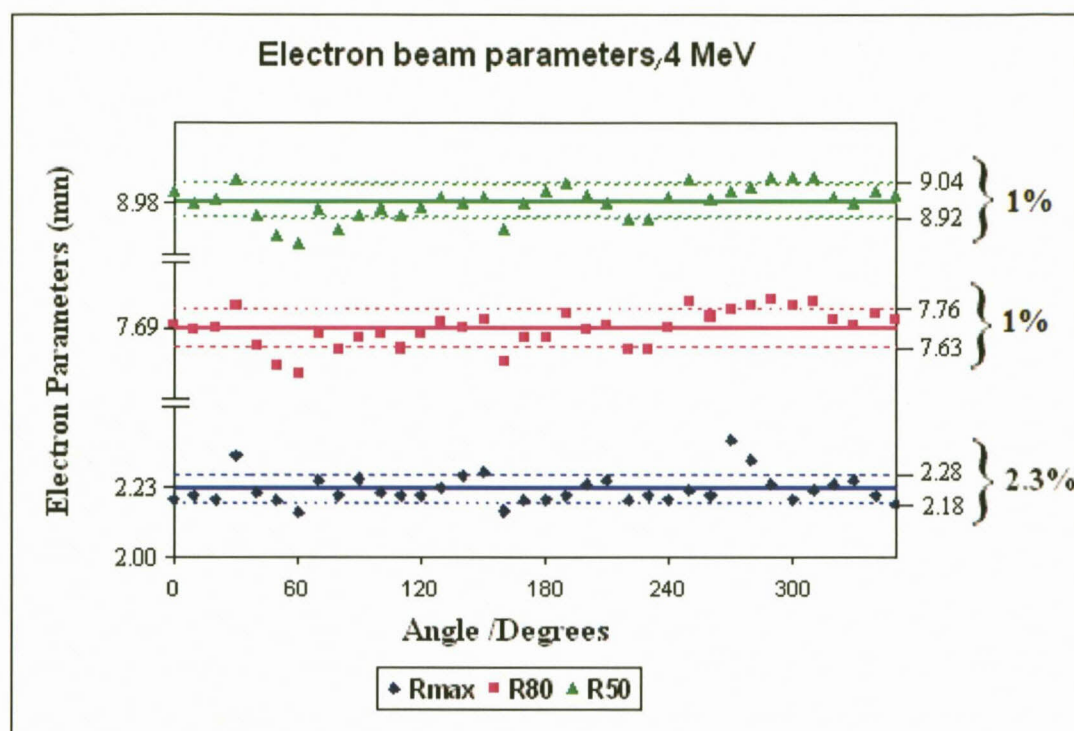


Figure 5.9: Variation of the electron beam parameters around the circumference of the cylindrical phantom obtained from the film measurements for 4 MeV for six dual fields.

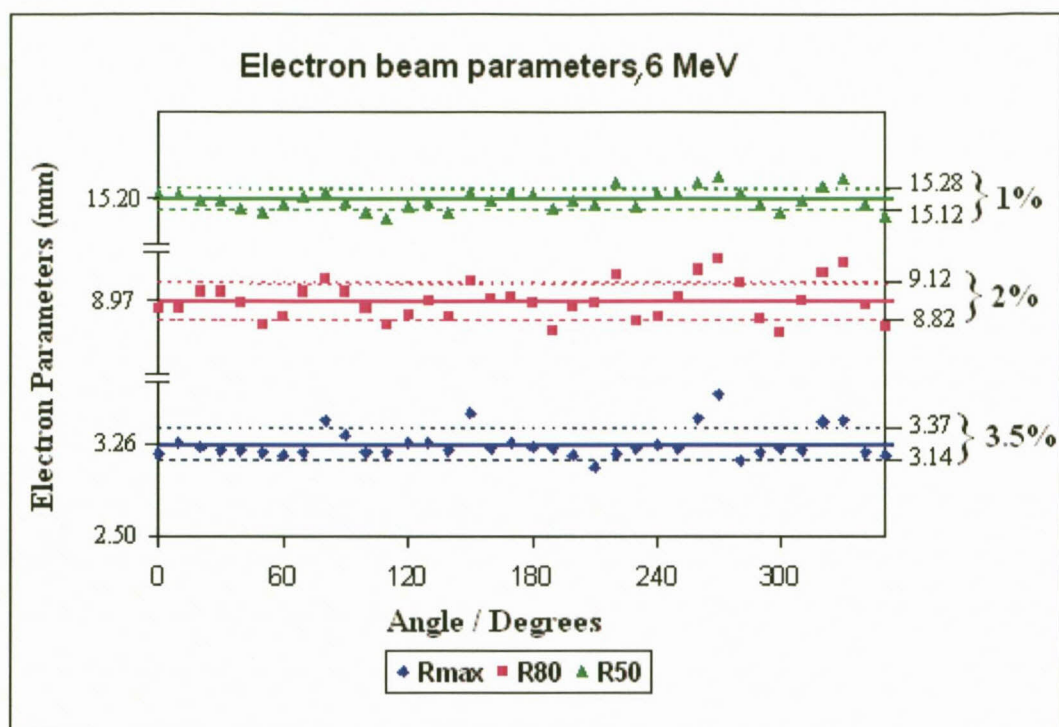


Figure 5.10: Variation of the electron beam parameters around the circumference of the cylindrical phantom obtained from the film measurements for 6 MeV for six dual fields.

5.5.2 Ratio of average skin dose to calibration dose: The overlap factor (OV)

The overlap factor was calculated using calibrated TLDs around the outer surface of the cylindrical phantom and also using film. The dosimeters were irradiated with six dual fields at 60° intervals. The average dose was determined for all the TLD chips.

The overlap factor was also calculated for the Rando phantom using TLD. The following table shows overlap factors, (OV) measured with the different phantoms and dosimeters. The overlap factor values are in agreement with the literature values (Turner et al, 1995, AAPM, 1988).

Method	Overlap factor	
	4 MeV	6 MeV
Cylindrical phantom (TLD)	(2.5±0.3)	(2.4±0.1)
Cylindrical phantom (Film)	(2.3±0.03)	(2.4±0.03)
Rando Phantom (TLD)	(2.88±0.2)	(2.68±0.2)

Table 5.2. The overlap factor.

5.6 Absolute dose measurement

The calibration depths were 6 mm and 10 mm for the 4 and 6 MeV respectively. These values correspond to the depth of maximum dose obtained from the depth dose curves in figures 5.7 and 5.8 for a single dual field (AAPM, 1988). The dose was measured with the parallel plate ion chamber (Roos chamber). The mean energy of the beam, \bar{E}_o , at the phantom surface (treatment plane) was determined by the half-value depth, R_{50} , for a single dual field using equation 2.20. The R_{50} values are 1.38 and 2.2 for 4 and 6 MeV, thus the mean energies are 3.2 and 5.1 MeV for the 4 and 6 MeV beams respectively.

5.7 X-ray contamination

AAPM, 1988 recommends an x-ray background of not more than 1%. The dual field technique reduces the total x-ray contamination at the centre because the main bremsstrahlung component is on the central axis of the beam. The x-ray contamination was measured from the tail of the percentage depth dose curves and it was found to be 0.9% and 1.3% for the 4 and 6 MeV electron beam energies respectively.

5.8 Monte Carlo Simulation

5.8.1 Simulation geometry of the Elekta Precise linear accelerator

In this study the Elekta Precise linear accelerator model was built and compiled with the EGS4/BEAMnrc MC code. A graphical representation of the geometry of the Monte Carlo model for the Elekta Precise linear accelerator as produced by BEAMnrc is shown in figure 5.11 below.

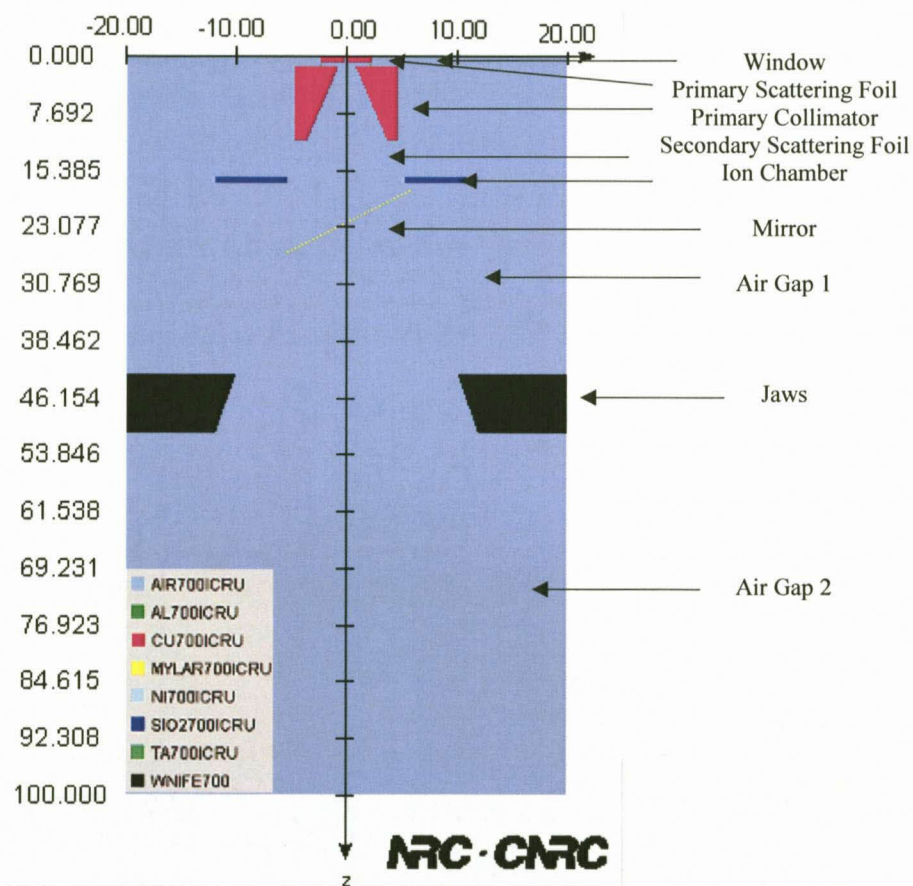


Figure 5.11. The output of simulation geometry of the Elekta Precise treatment head.

5.8.2 Monte Carlo simulation of the Elekta Precise linear accelerator

The BEAMnrc simulation consisted of two major stages; in the first stage we obtained the primary phase space file (PPSF), where the scoring plane was at the isocentre (100 cm SSD). In this stage the beam simulation parameters were adjusted for a good match to the beam data measured at 100 cm SSD. In the second stage, the PPSF was used as source input for obtaining the secondary phase space file (SPSF) which was used subsequently as an input source to compute dose distributions at the treatment plane (350 cm SSD).

BEAMnrc calculates uncertainties of its results by dividing the total number of histories into 10 equal batches and determining the average value and standard deviation from the results of the ten batches. In order to obtain uncertainties below 2% it was found necessary to run 1×10^8 histories for the first stage of simulation. The PSFs generated from each batch were combined together to get the total number. The primary phase space files occupied 0.929 and 1.5 Gbyte of disk space for 4 and 6 MeV respectively. The secondary phase space files that were collected at the treatment plane occupied 2.0 and 2.2 Gbyte of disk space for 4 and 6 MeV respectively. Details of the simulation are shown in Table 5.3.

Energy	Scoring plane	No of Particles in PSF	No of incident Histories/Million	CPU time for Simulation	Simulation rate (histories/hr)
4 MeV	100 cm SSD	8.0×10^7	100	12.61 hr	7.9×10^6
	350 cm SSD	1.0×10^7	100	3.24 hr	3.1×10^7
6 MeV	100 cm SSD	8.0×10^7	100	13.81 hr	7.2×10^6
	350 cm SSD	5.0×10^7	100	4.65 hr	2.2×10^7

Table 5.3. Details of the simulations to acquire the PPSFs and SPSFs.

Results from the above table can be summarized as follows:

- 1) The number of histories utilized in all the simulation stages were the same. (To obtain uncertainties below 2%).
- 2) The number of particles in the PPSFs (at the isocentre scoring plane) was the same for both energies. The number of particles in the SPSFs (At the treatment plane) was slightly larger for 6 MeV than for 4 MeV, due to more scattering and energy loss in air for 4 MeV electrons.
- 3) Simulation time for the PPSFs was longer than for the SPSFs at the isocentre because of the simulation of all head components of the accelerator comparing with a very short simulation time at the treatment plane because only one component module (the air slab) had to be simulated.
- 4) The simulation rates for the two energies for the same scoring plane are almost the same.

5.8.3 Analysis of the phase space files

By using the BEAMDP program (Ma and Rogers, 2005) the characteristics of the electron beams were determined from the different phase space files at the isocentre (100 cm SSD) and at the treatment plane (350 cm SSD). The following figures show the electron fluence variations with position, energy fluence variations with position, spectral distributions and angular distributions.

5.8.3.1 Fluence variation with position

The planar fluence for a square field with minimum and maximum dimensions of -100 , $+100$ cm for both the X and Y directions for the PPSFs and -200 , $+200$ cm for both the X and Y directions for the SPSFs was calculated. The number of bins was set to 100. The figures below show the planar fluence distribution along the x-direction. The planar fluence is displayed for all particles, for electrons only and for photons only. The planar fluence has a maximum at the central axis and then decreases with increase of the distance from the central axis.

Figures 5.12 and 5.13 show the planar fluence at the isocentre (100 cm SSD) for 4 and 6 MeV respectively. In these graphs the highest peaks include all the particles, peaks in the middle represent the electrons only and the smallest peaks show the photons.

Figures 5.14 and 5.15 represent the planar fluence at the treatment plane (350 cm SSD) for 4 and 6 MeV respectively. These planar fluence graphs are slightly more uniform at the field center and start to decrease when we move further away from the central axis.

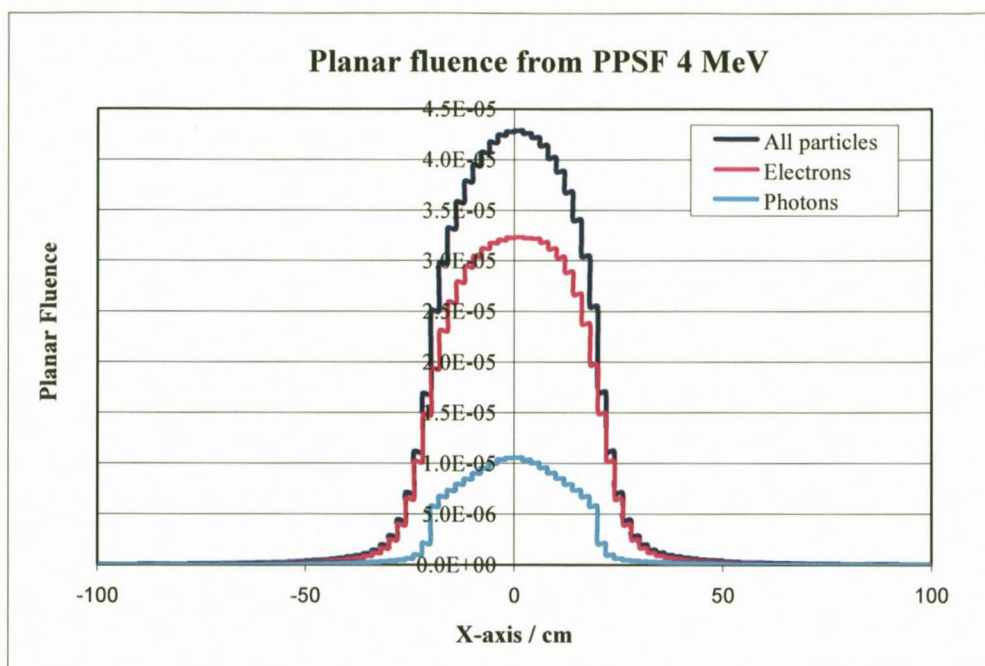


Figure 5.12 Fluence distributions in the x-direction in the plane of the PPSF for 4 MeV at 100 cm SSD.

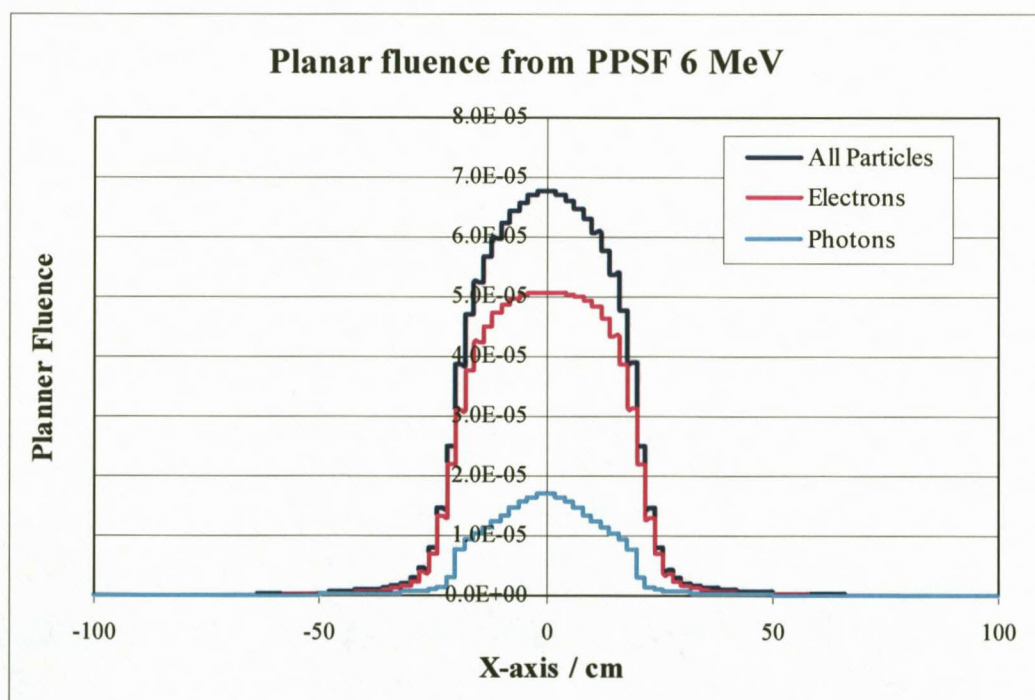


Figure 5.13. Fluence distributions in the x-direction in the plane of the PPSF for 6 MeV at 100 cm SSD.

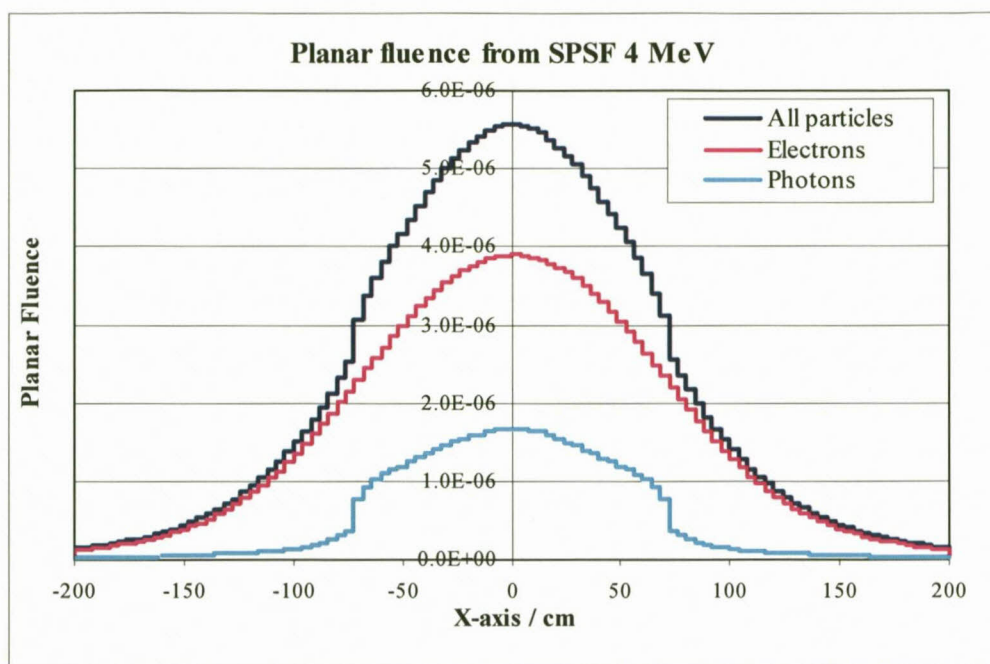


Figure 5.14. Planar fluence distribution in the x-direction in the plane of the PPSF for 4 MeV at 350 cm SSD.

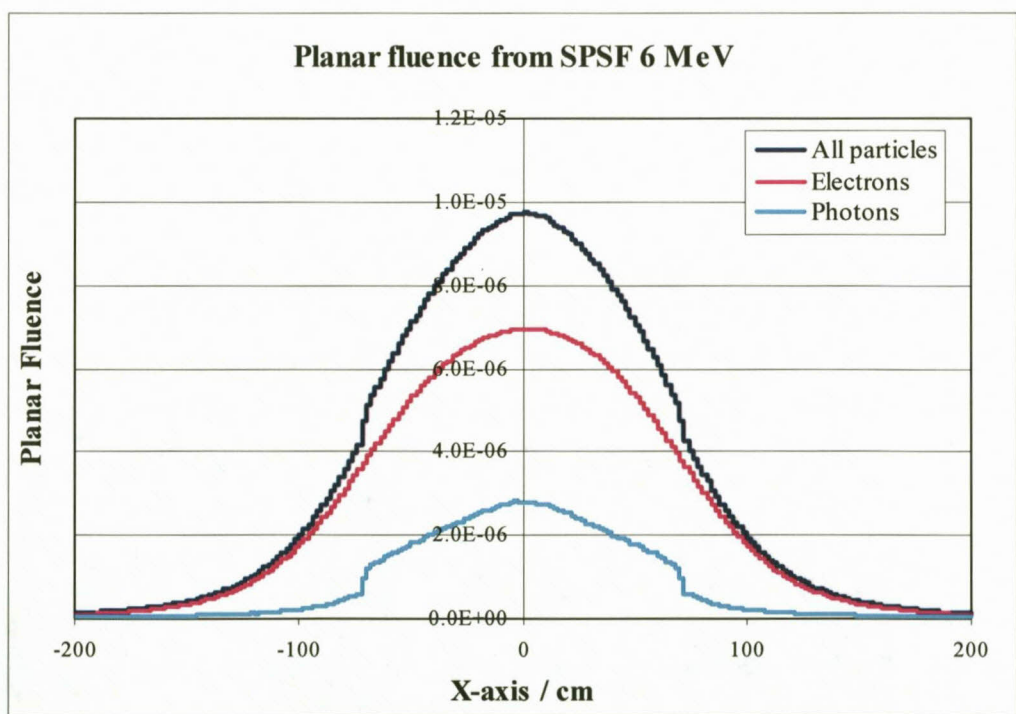


Figure 5.15. Fluence distribution in the x-direction in the plane of the PPSF for 6 MeV at 350 cm SSD.

5.8.3.2 Energy fluence variations with position

The planar energy fluence for a square field with minimum and maximum dimensions of $-100, +100$ cm for both the X and Y directions respectively is shown in Figures 5.16 and 5.17 for 4 and 6 MeV at the isocentre. Figures 5.18. and 5.19 show the energy fluence at the treatment plane for both 4 and 6 MeV respectively.

It can be seen that in all cases the photon energy fluence is only a small fraction of the total energy fluence.

Because the dose is proportional to the photon energy fluence $\left(D_{\text{photon}} \propto \Psi \cdot \left(\bar{\mu}_{\text{en}} / \rho \right) \right)$, this explains the small contribution of photons to the total depth dose curves shown in figures 5.31 and 5.32 (pages 126, 127).

For the electrons the absorbed dose to medium is related to the particle fluence

$$\left(D_{\text{elec}} \propto \Phi \left(\bar{S}_{\text{col}} / \rho \right) \right).$$

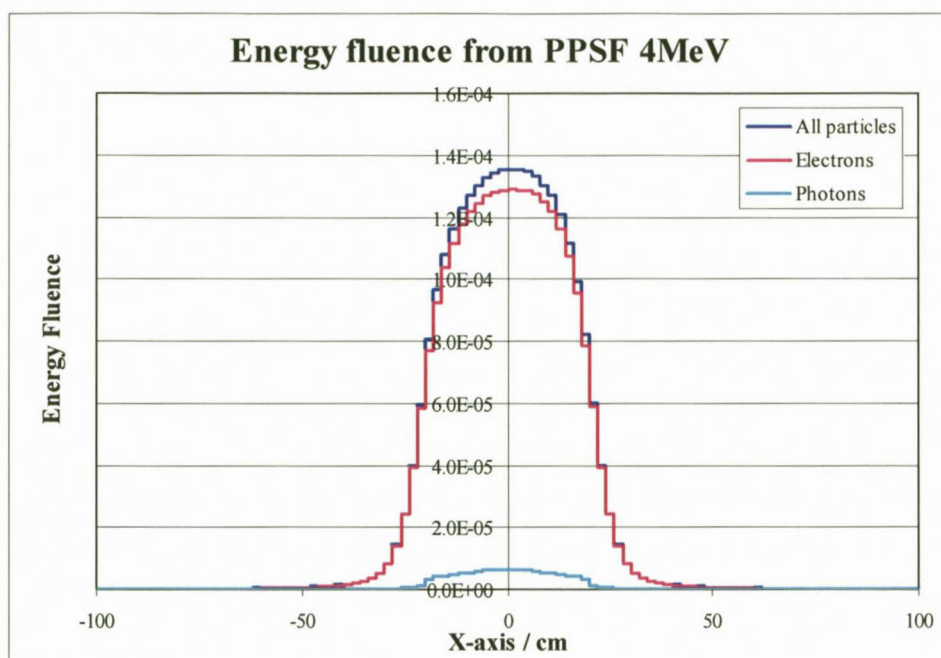


Figure 5.16. Energy fluence distribution in the x-direction in the plane of the PPSF for 4 MeV at 100 cm SSD.

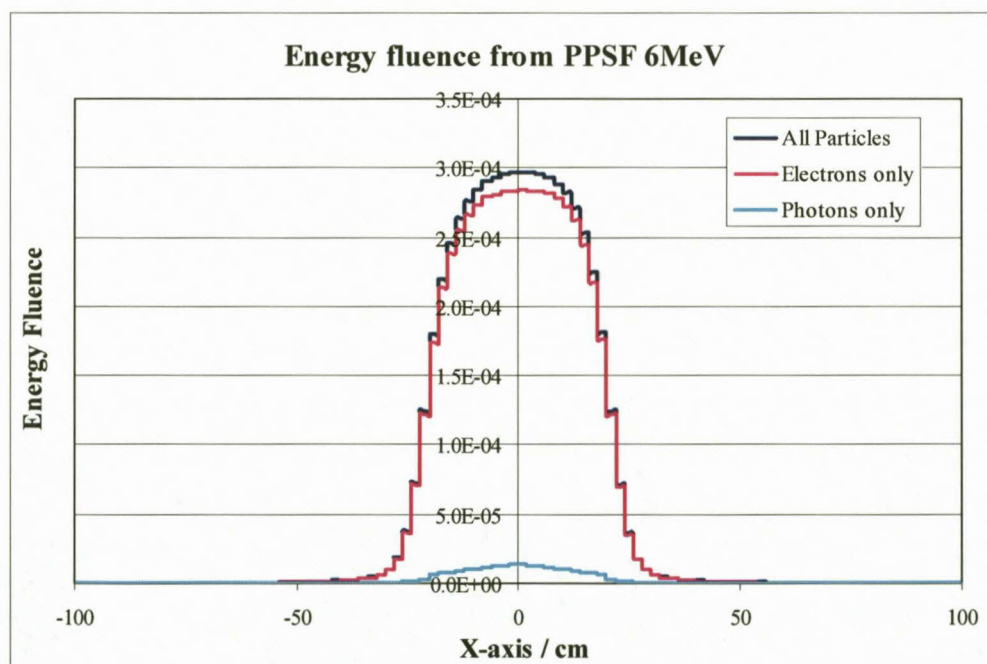


Figure 5.17. Energy fluence distribution in the x-direction in the plane of the PPSF for 6 MeV at 100 cm SSD.

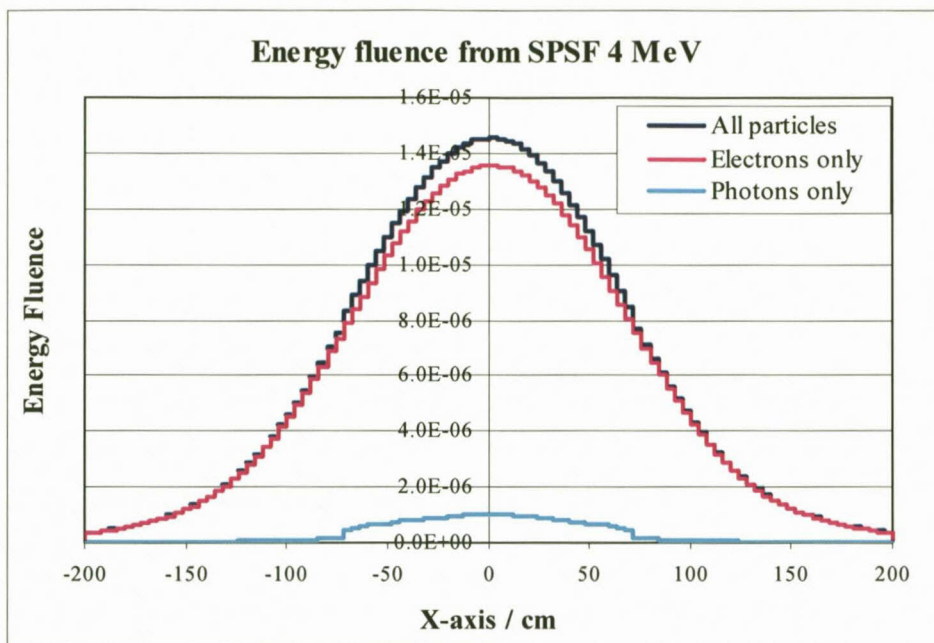


Figure 5.18. Energy fluence distribution in the x-direction in the plane of the SPSF for 4 MeV at 350 cm SSD.

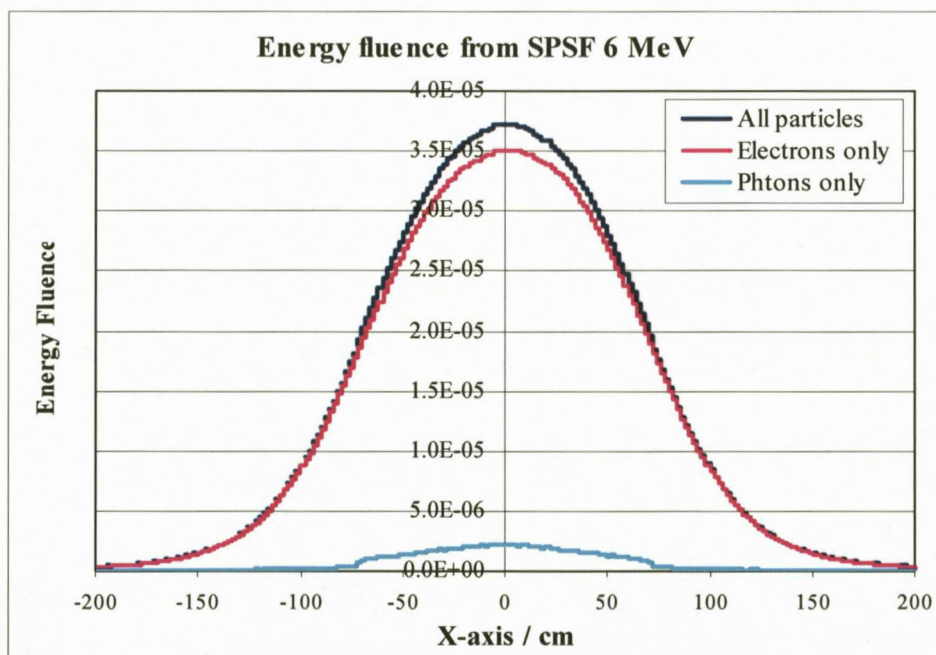


Figure 5.19. Energy fluence distribution in the x-direction in the plane of the SPSF for 6 MeV at 350 cm SSD.

5.8.3.3 Spectral distribution

The spectral distribution gives the total number of particles scored in each energy bin within a specified energy range. The spectral distribution at SSD = 100 cm and at SSD = 350 cm for monoenergetic incident electron beams are shown in figures 5.20 to 5.23. It can be noted that the spectra have two main peaks that are indicated for all particles (dark blue line) and electrons only (red lines). These two peaks are probably due to the geometry of the primary and secondary scattering foils respectively (Björk et al, 2002). The light blue line shows the contamination photon spectrum. It is evident that the photons have a low mean energy, which accounts for the small energy fluence in figures 5.16 to 5.19.

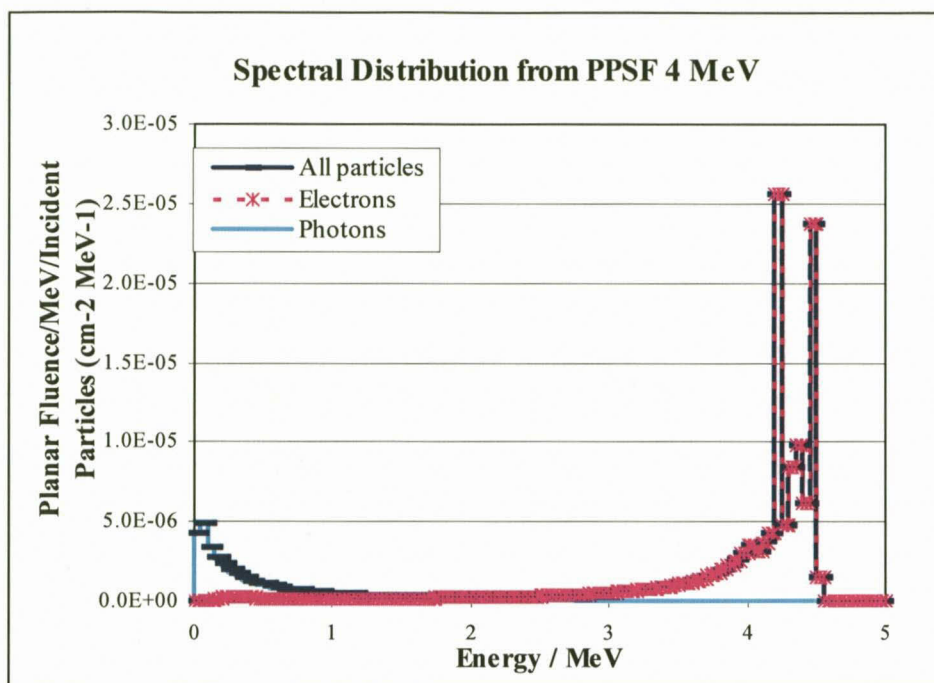


Figure 5.20. Spectral distribution of the PPSF for the 4 MeV at 100 cm SSD.

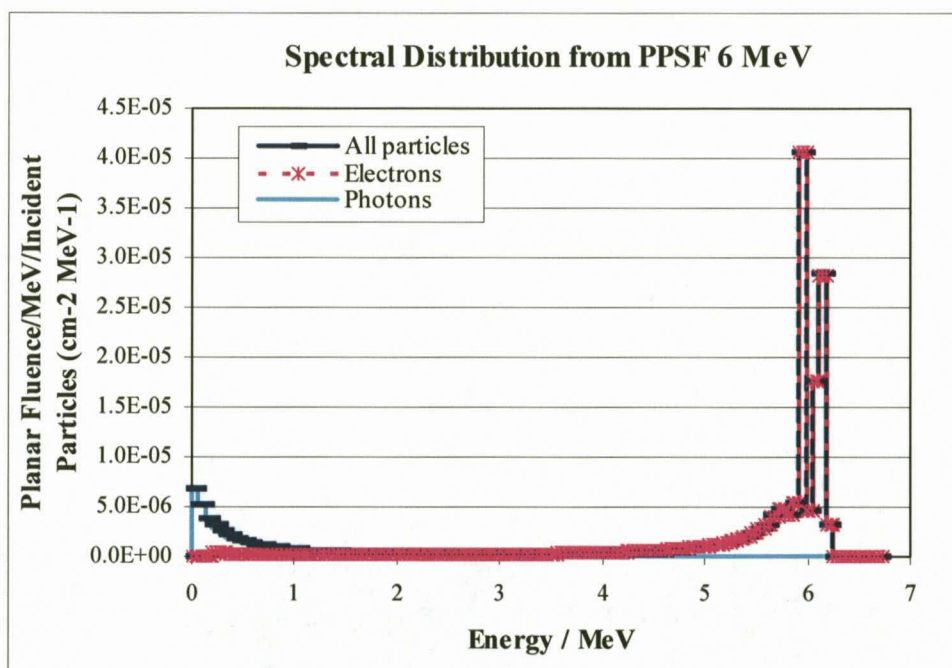


Figure 5.21. Spectral distribution of the PPSF for the 6 MeV at 100 cm SSD.

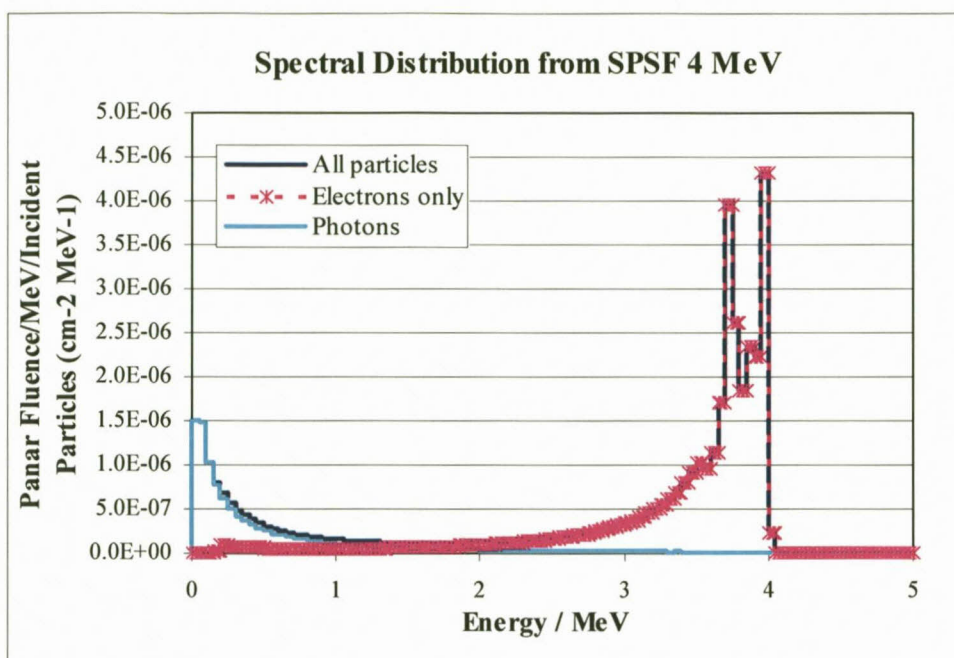


Figure 5.22. Spectral distribution of the SPSF for the 4 MeV at 350 cm SSD.

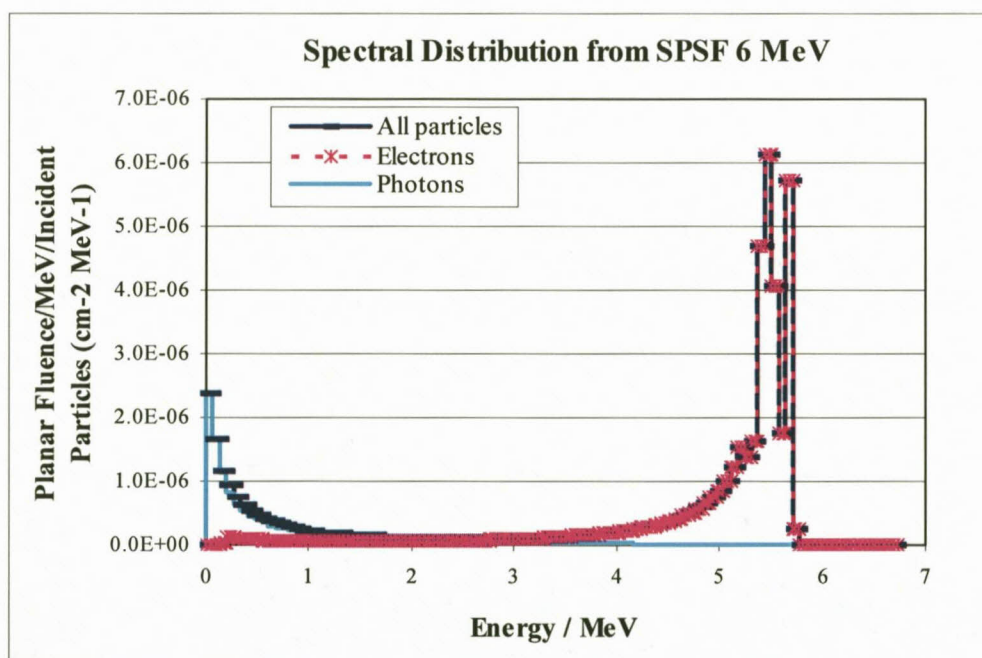


Figure 5.23. Spectral distribution of the SPSF for the 6 MeV at 350 cm SSD.

5.8.3.4 Angular distributions

Figures 5.24 to 5.27, show the angular distribution at SSD =100 cm and SSD = 350 cm for both energies. The number of bins was set to 100 and the angles range from 0° to 90° . All these figures contain graphs for all the particles (dark blue line), electrons only (red line) and photons only (light blue). For all of these graphs the number of particles at 0° is close to zero. The distributions peak at angles between 10° to 20° . The angular distribution is mainly affected by the passage of the electrons through the scattering foil system.

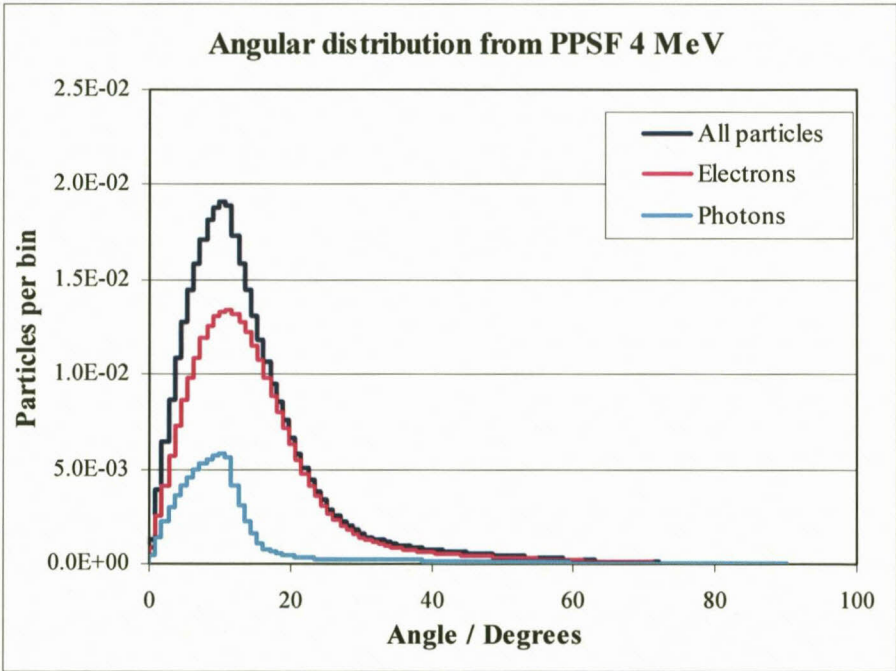


Figure 5.24. Angular distribution of the PPSF for 4 MeV at 100 cm SSD.

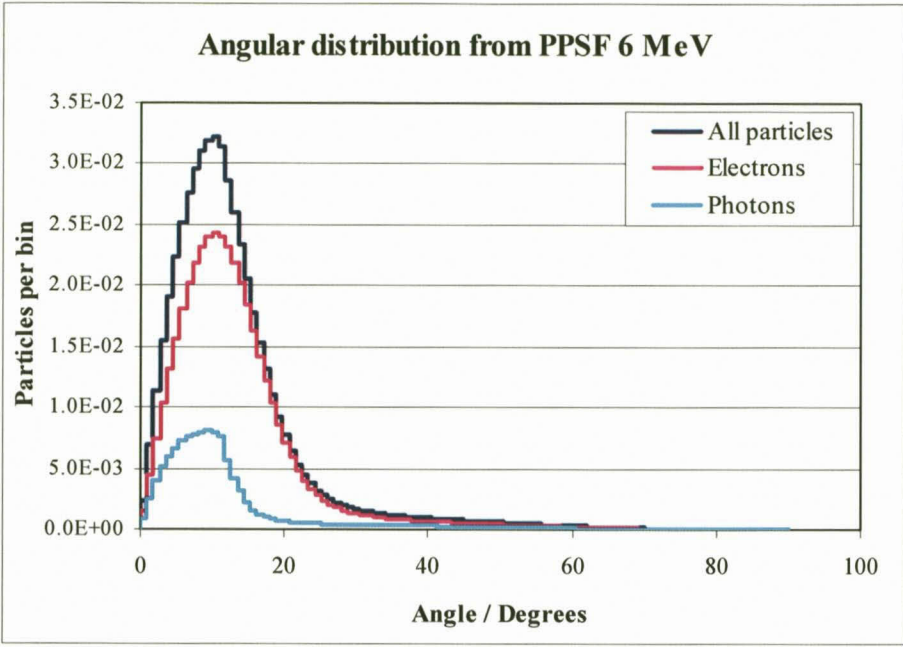


Figure 5.25. Angular distribution of the PPSF for 6 MeV at 100 cm SSD.

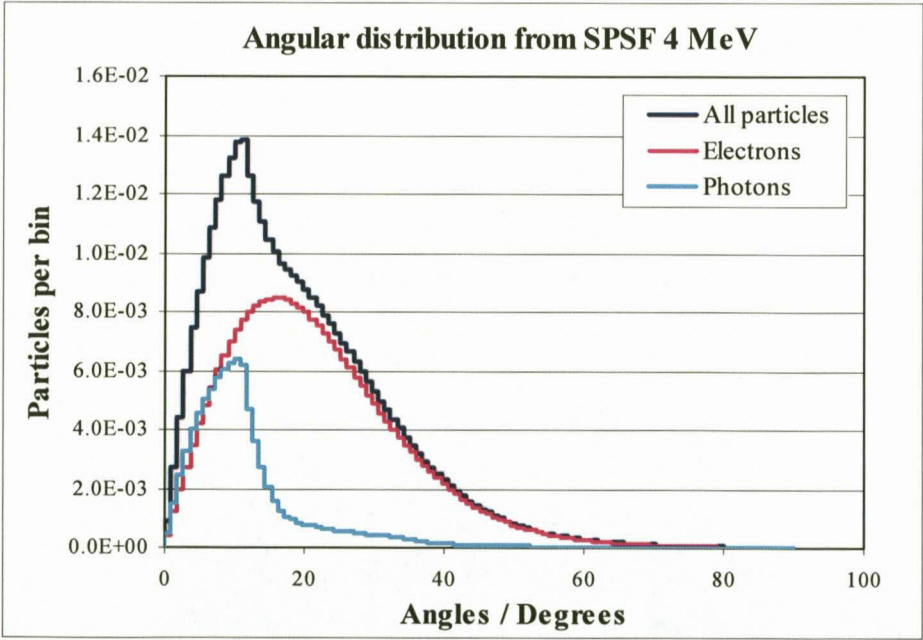


Figure 5.26. Angular distribution of the SPSF for 4 MeV at 350 cm SSD.

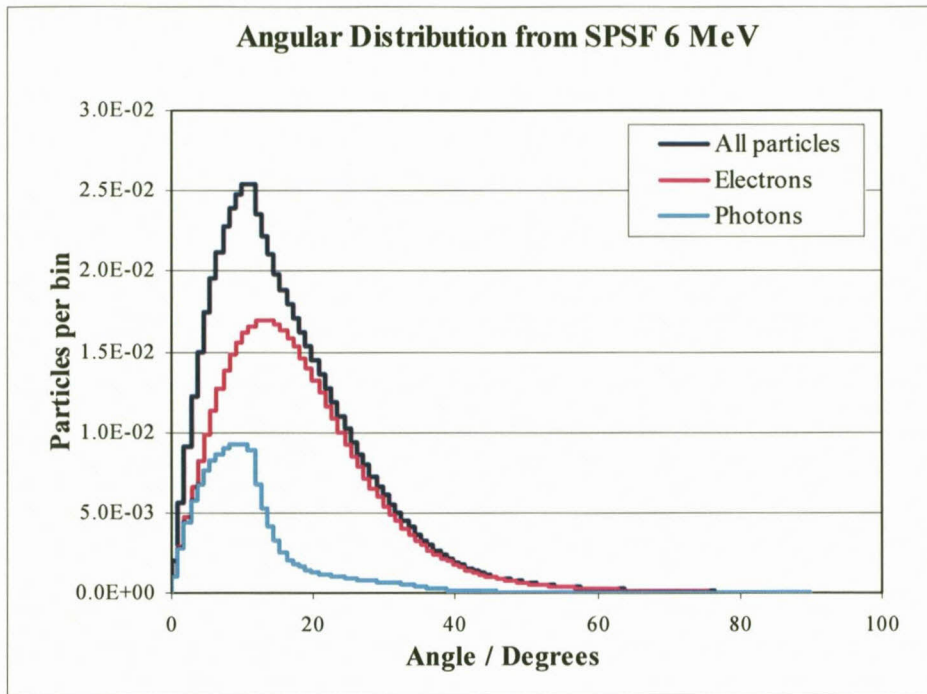


Figure 5.27. Spectral distribution of the SPSF for 6 MeV at 350 cm SSD.

5.8.4. Validation of the Monte Carlo model

The parameters characterizing the electron beam incident on the exit window were found by matching our calculated beam data (percentage depth doses and cross-beam profiles) to our measurements in the water phantom at the isocentre (100 cm SSD). For the measured beam data of 4 and 6 MeV energies we found the best match (fine-tuning) for the calculated beam data by using 5 and 6.72 MeV energies respectively. Also we used parallel circular beams having Gaussian radial distributions with full width at half-maximum of 0.05 cm. The electron source was considered monoenergetic in both cases. The MC beam models were then evaluated at the treatment plane by comparing the calculated PDDs and profiles with measurements as explained in chapter 4. Dose distributions in the Rando phantom were also compared.

5.8.5 Calculation of the beam data in a water phantom with the DOSXYZ code

The phase space files created in the first stage of the simulation for the 4 and 6 MeV at the two scoring planes were used to calculate percentage depth dose and cross-plane profiles in a water phantom using the DOSXYZ program.

The number of histories to be used for each scoring plane for each energy was determined by carrying out trial simulations as mentioned before in chapter 4 (section 4.4.5.2). Simulations were done with two different phantoms, using 200 and 600 million histories for the phantoms at the isocentre and at the treatment plane respectively. This resulted in an uncertainty below 2% for both scoring planes. Table 5.4 and figures 5.28 to 5.31 show the results and comparison of the depth doses and beam profiles for the two scoring planes.

Energy	Scoring Plane	No of Particles in PSF	No of incident Histories/Million	CPU time for Simulation	Simulation rate (histories/hr)
4 MeV	100 cm SSD	3.4×10^7	400	5.63 hr	7.1×10^7
	350 cm SSD	7.7×10^7	600	8.28 hr	7.2×10^7
6 MeV	100 cm SSD	5.2×10^7	200	13.43 hr	1.5×10^7
	350 cm SSD	7.7×10^7	400	25.52 hr	1.6×10^7

Table 5.4 Details of the calculations of the beam data from the PPSFs and SPSFs.

The results in table 5.4 show that the simulation time for 4 MeV is much shorter than for 6 MeV. That is mainly due to the difference in the specifications of the PCs that were used in the simulation.

Figures 5.29 and 5.30 show the PDDs at SSD = 100 cm and at SSD = 350 cm for 4 and 6 MeV for a single horizontal beam. In both figures notice that the depth dose curves start from 0.25 cm because of the first pixel size 0.25 cm that was constructed in the water phantom. Also the depth dose curve moves towards the surface as we move to the extended distance. The uncertainty of the simulation is less than 2%.

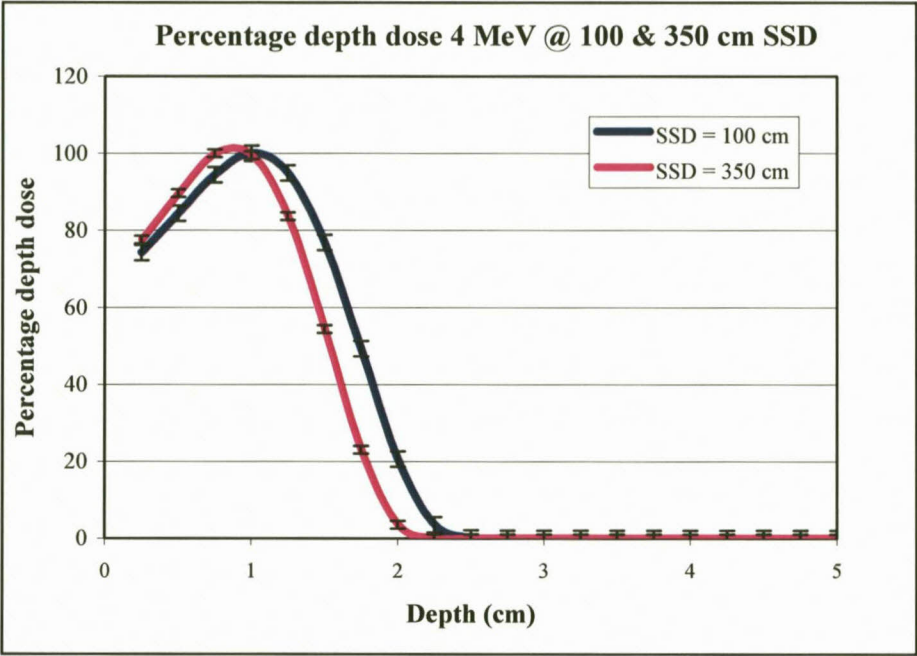


Figure (5.28): Calculated percentage depth dose curves at SSD = 100 cm and SSD = 350 cm for the 4 MeV electrons.

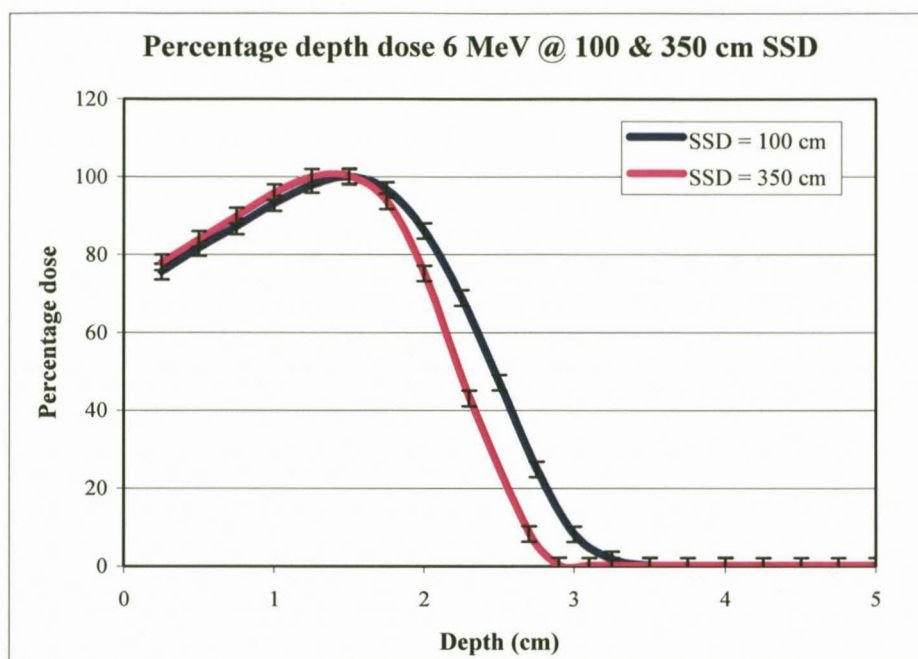


Figure (5.29): Calculated percentage depth dose curves at SSD = 100 cm and SSD = 350 cm for the 6 MeV electrons.

Figures 5.30 and 5.31 below show the depth dose curves for the 4 and 6 MeV energies at the isocentre (100 cm SSD) for all the particles, for electrons only and for photons only. This was done by selecting only one type of particle from the PSFs used as source for the DOSXYZ program. Both figures indicate that the PDD curves for all particles (blue line) and electrons are almost the same. The contribution of the photons for the total depth dose curve is very small. These results can be explained by the small energy fluence of the photons as discussed in section 5.8.3.2.

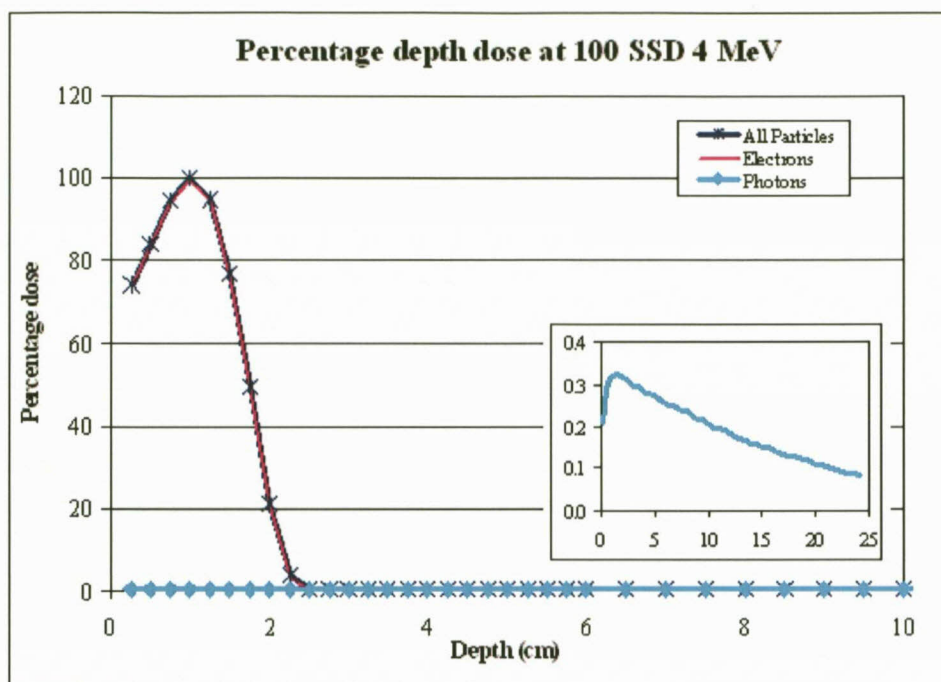


Figure (5.30): Comparison of calculated percentage depth dose curves at SSD = 100 for all the particles, electrons only and photons only for 4 MeV.

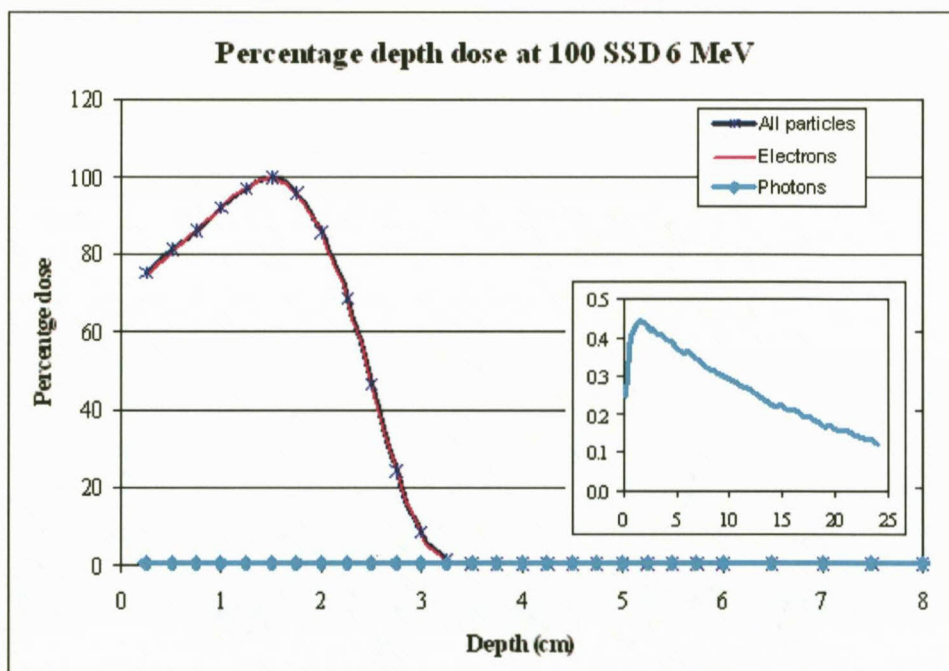


Figure (5.31): Comparison of calculated percentage depth dose curves at SSD = 100 for all the particles in phase, electrons only and photons only for 6 MeV.

Figures 5.32 and 5.33 show the beam profiles at isocentre and at the treatment plane for both 4 and 6 MeV. The beam profiles of the two energies appear similar, as was also found for measurements (figure. 5.5). The same applies to the profiles at the treatment plane (Figures 5.33 and 5.6).

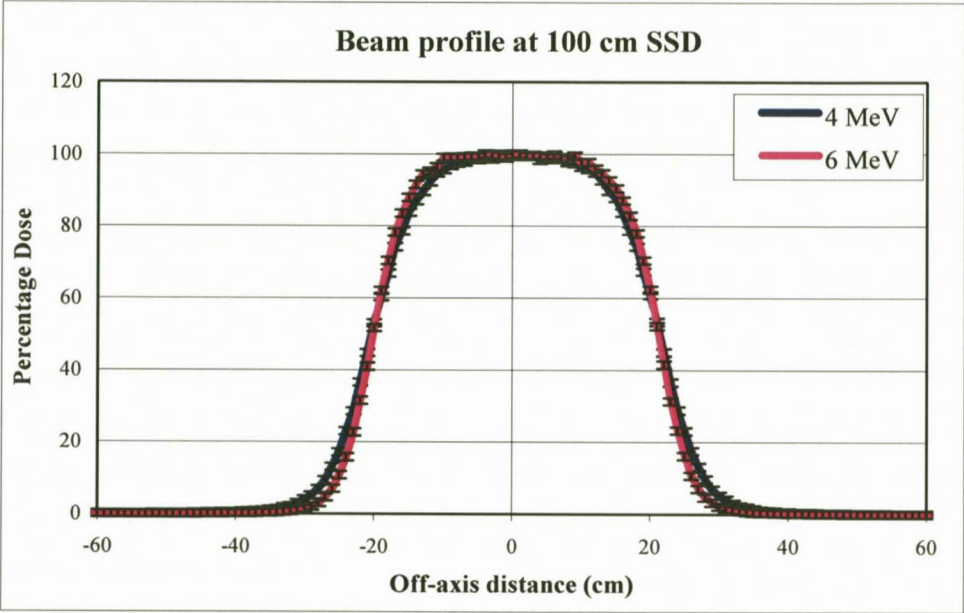


Figure 5.32. Beam profiles at isocentre (100 cm SSD) for 4 and 6 MeV energies at a depth of d_{max} .

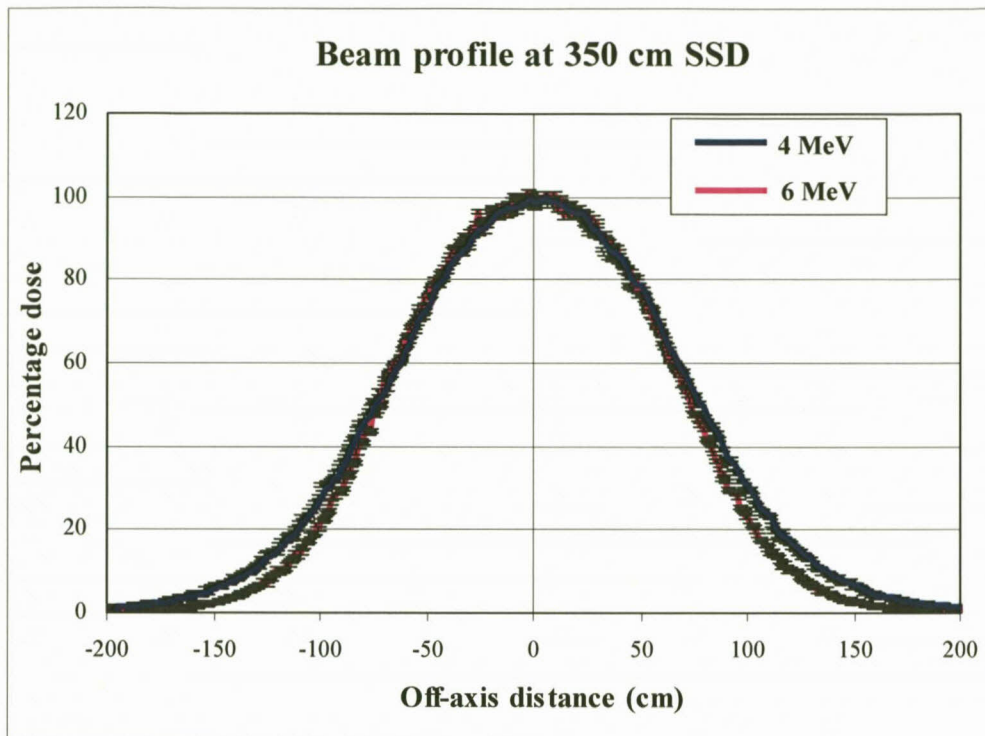


Figure 5.33. Beam profiles at the treatment plane (350 cm SSD) for 4 and 6 MeV energies at a depth of d_{\max} .

5.8.6 Dual beam characteristics

Once the single beam parameters have been determined to be adequate, the next task is to find the optimum beam angles, which is very much like matching beams in conventional treatment planning. The objective is to find the appropriate projection angle that gives a flat ($\pm 10\%$) profile over approximately 2 m (AAPM, 1988). For TSET beams, we are helped by the fact that the beams are very broad and there is no distinct beam edge. By using a range of angles between the central axes of two beams, the angle that gave the best uniformity of dose was determined. The calculated combined beam profiles for the optimum angles, are shown in Fig. 5.34 and 5.35. The optimum angle was found to be 14° for 4 MeV and 16° for the 6 MeV. The dose uniformity was $\pm 5\%$ for 4 MeV and $\pm 3\%$ for 6 MeV over the range of -100 to +100 cm.

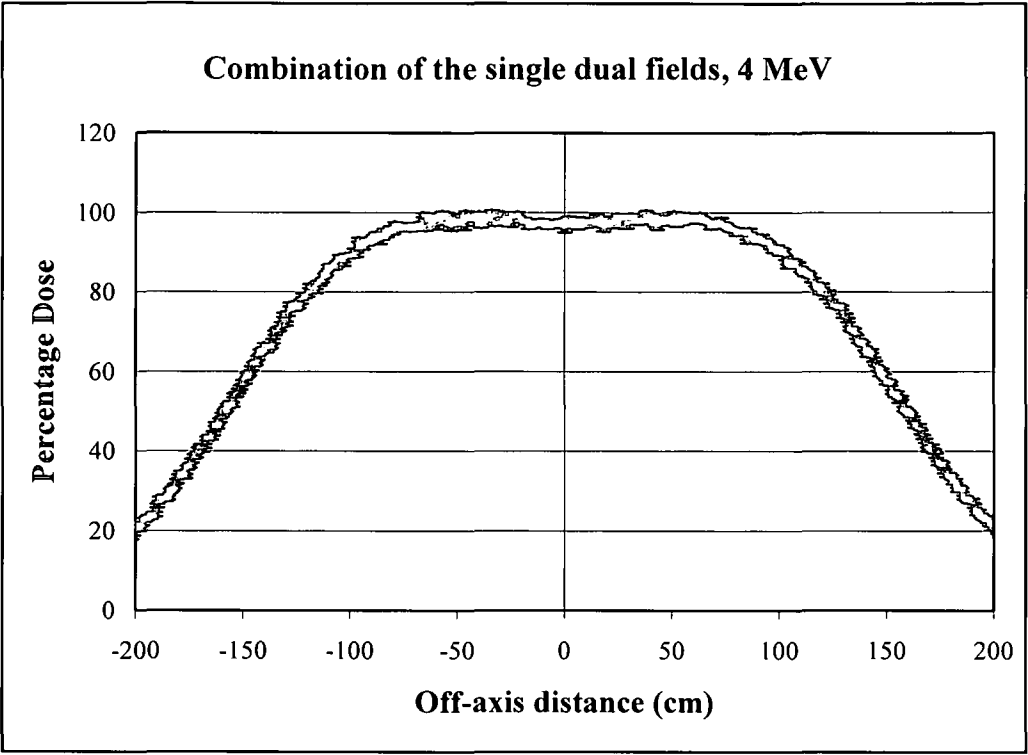


Figure 5.34. Beam profile for a pair of 14° angled fields at the treatment plane for 4 MeV.

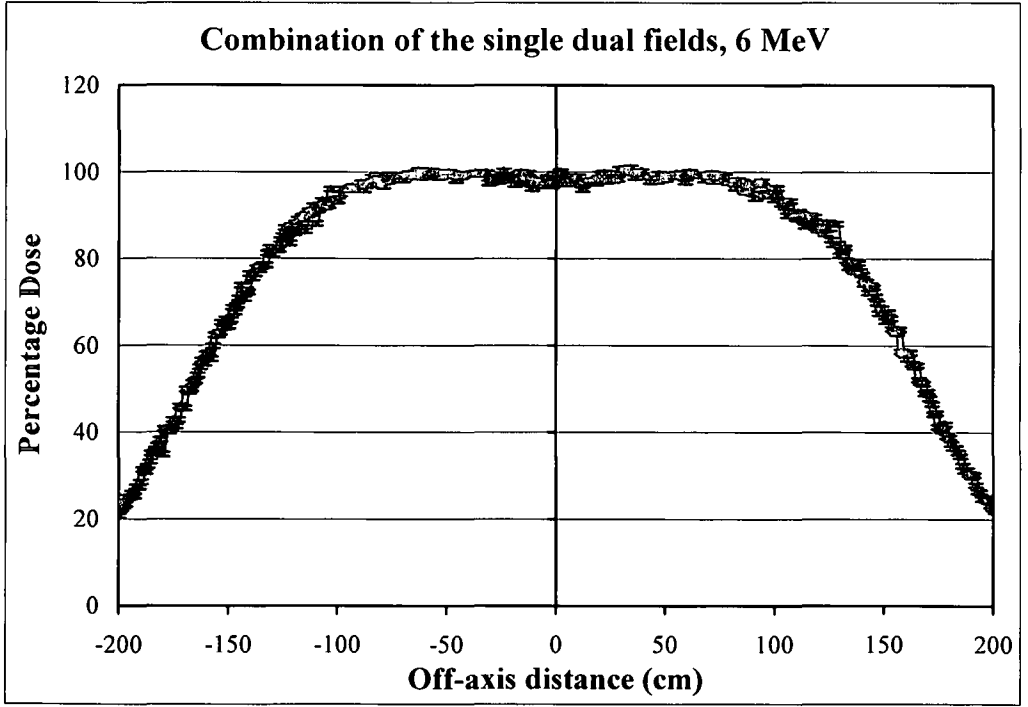


Figure 5.35 Beam profile for a pair of 16° angled fields at the treatment plane for 6 MeV.

5.8.7 Comparisons of PDDs obtained by Monte Carlo method and the Measurements

Figures 5.36 to 5.39 show a comparison of percentage depth dose curves obtained by the MC method and ionization chamber and film measurement. Both MC and measurements data were normalized to 100% at d_{max} . Both methods are in good agreement.

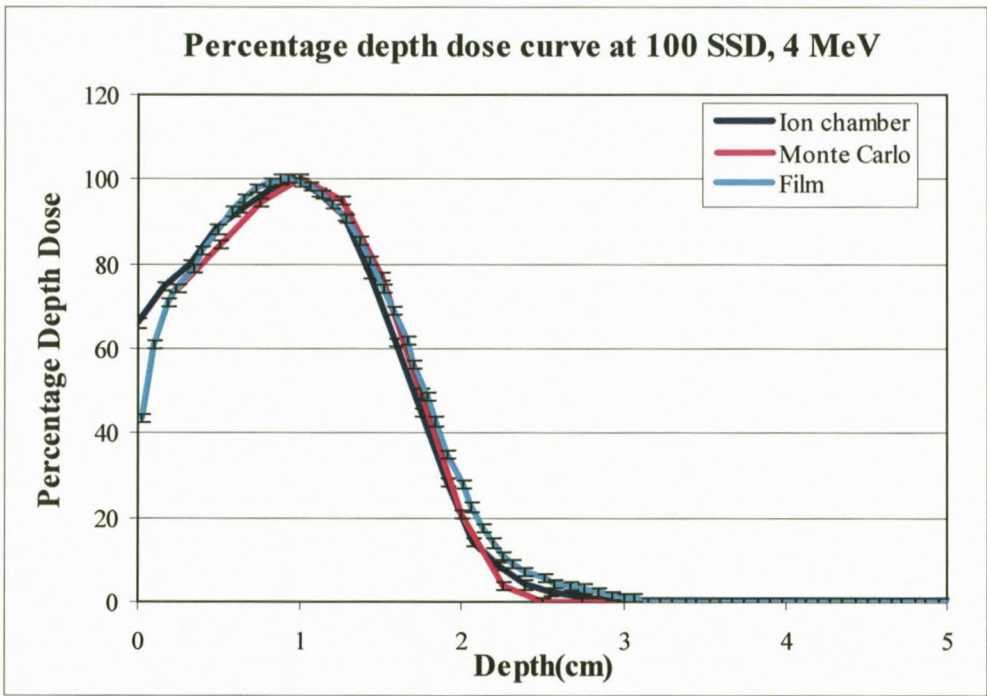


Figure 5.36: Percentage depth dose curves for calculated and measured data at SSD = 100 cm for 4 MeV.

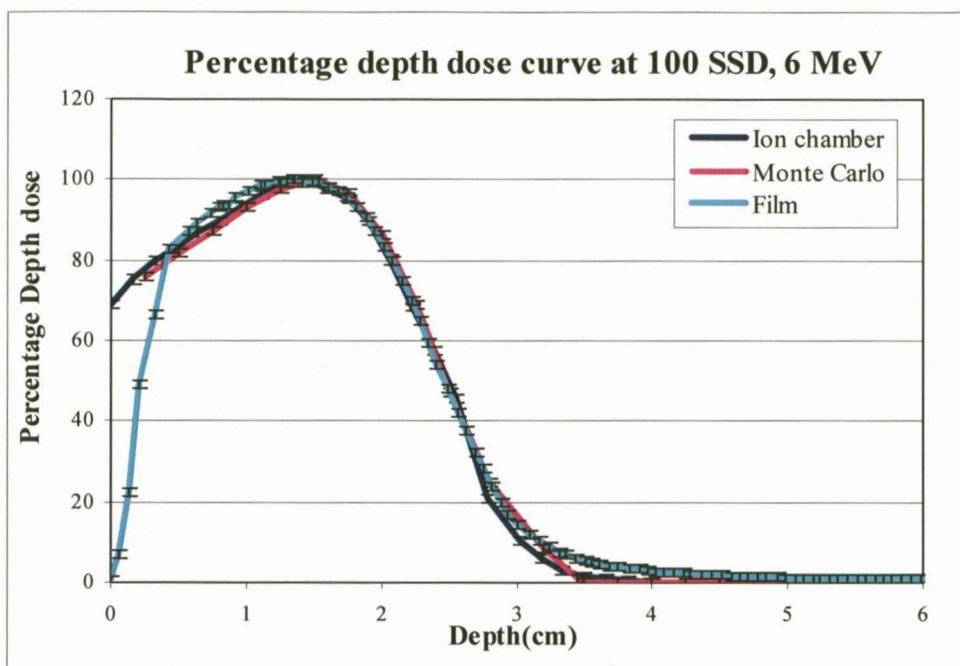


Figure 5.37: Percentage depth dose curves for calculated and measured data at SSD = 100 cm for 6 MeV.

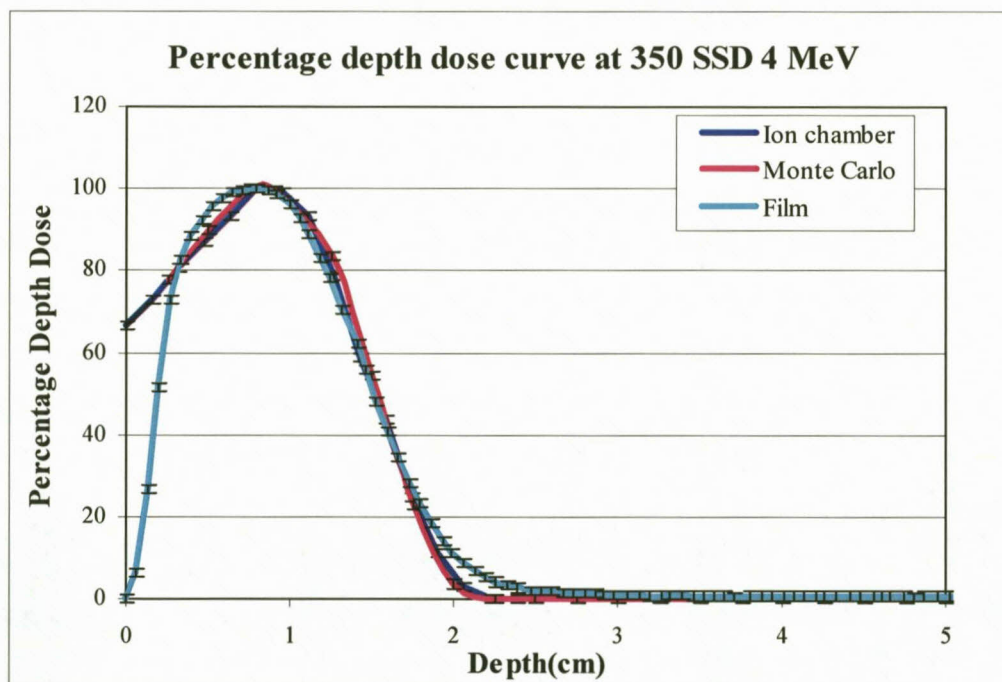


Figure 5.38: Percentage depth dose curves for calculated and measured data at SSD = 350 cm for 4 MeV.

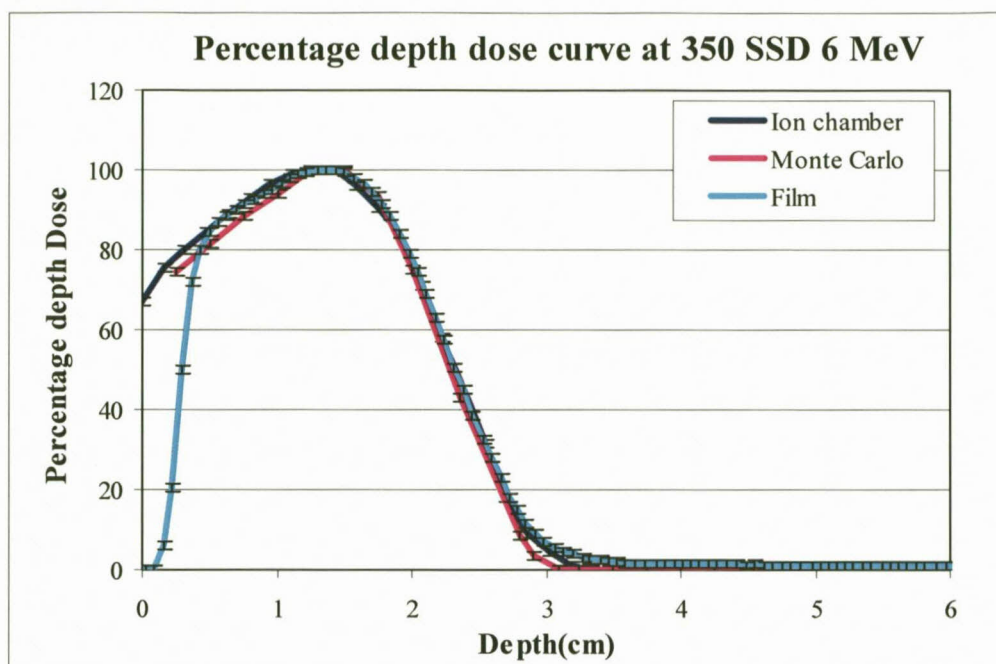


Figure 5.39: Percentage depth dose curves for calculated and measured data at SSD = 350 cm for was 6 MeV.

Figures 5.36 and 5.37 show the depth doses at 100 cm SSD for the $40 \times 40 \text{ cm}^2$ field for 4 and 6 MeV respectively. The statistical uncertainties in the MC data are less than $\pm 2\%$. The calculated values of d_{max} , R_{50} , and R_p , agree with measured data within about 1 mm.

The percentage depth doses at the treatment plane are shown in figures 5.38 and 5.39. Depth dose agreement between MC and measurements are within about 1 mm. The values of d_{max} , R_{50} and R_p again agree well. For 4 MeV the average d_{max} is shifted about 2 mm from 0.95 to 0.78 cm, for the PDD curve at the isocentre compared to that at the treatment plane. For the 6 MeV the average d_{max} shifted from 1.44 to 1.36 cm when comparing the PDDs at the isocentre with that at the treatment plane. The above obtained results are consistent with other results reported in the literature (Sung et al, 2005).

Detector	4 MeV			6 MeV		
	d_{\max}	R_{50}	R_p	d_{\max}	R_{50}	R_p
Ion Chamber	0.96	1.71	2.23	1.43	2.48	3.22
Film	0.92	1.75	2.33	1.41	2.45	3.15
MC	0.98	1.74	2.25	1.48	2.47	3.13
Average	0.94	1.73	2.28	1.42	2.465	3.185
St.Dev	0.03	0.03	0.07	0.01	0.02	0.05
Difference	0.04	0.01	0.03	0.06	0.01	0.06

Table 5.5. PDD parameters at 100 cm SSD. All values in cm.

Detector	4 MeV			6 MeV		
	d_{\max}	R_{50}	R_p	d_{\max}	R_{50}	R_p
Ion Chamber	0.78	1.53	2.01	1.36	2.33	2.94
Film	0.79	1.52	2.1	1.34	2.32	2.95
MC	0.75	1.54	2.01	1.37	2.29	2.88
Average	0.79	1.53	2.06	1.35	2.33	2.95
St.Dev	0.01	0.01	0.06	0.01	0.01	0.01
Difference	0.04	0.02	0.04	0.02	0.04	0.07

Table 5.6. PDD parameters at 350 cm SSD. All values in cm.

Tables 5.5 and 5.6 show measured and calculated characteristic parameters of the percentage depth dose curves for the two energies for 40x40 cm² at the isocentre (100 cm SSD) and the TSET beam at the treatment plane (350 cm SSD). These tables show a numerical comparison for the two electron energies for the PDDs that were shown in the above figures. As expected, there is excellent agreement in the R_{50} and R_p depths between the ion chamber data and MC data. In the comparison, the average depth indicated in the tables represents the average for measured data using ion chamber and film. The difference is noted between this average depth for the two measurements and MC.

5.8.8 Comparison of cross plane profiles obtained by Monte Carlo and the Measurements

Figures 5.40 to 5.43 show a comparison of beam profile curves obtained by the MC method and ionization chamber. Both MC and measurement data were determined at the depth of maximum dose (d_{\max}) and normalized to 100% at the central axis. Both methods are also in good agreement.

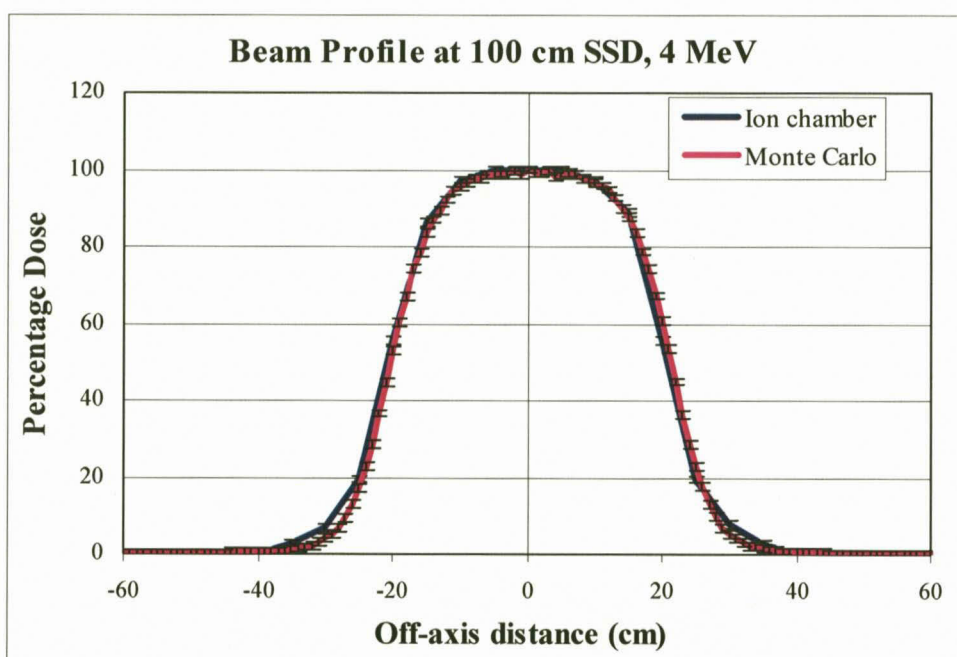


Figure 5.40. Beam profiles measured with ion chamber and calculated with MC at the isocentre (100 cm SSD) for 4 MeV at the depth of d_{\max} .

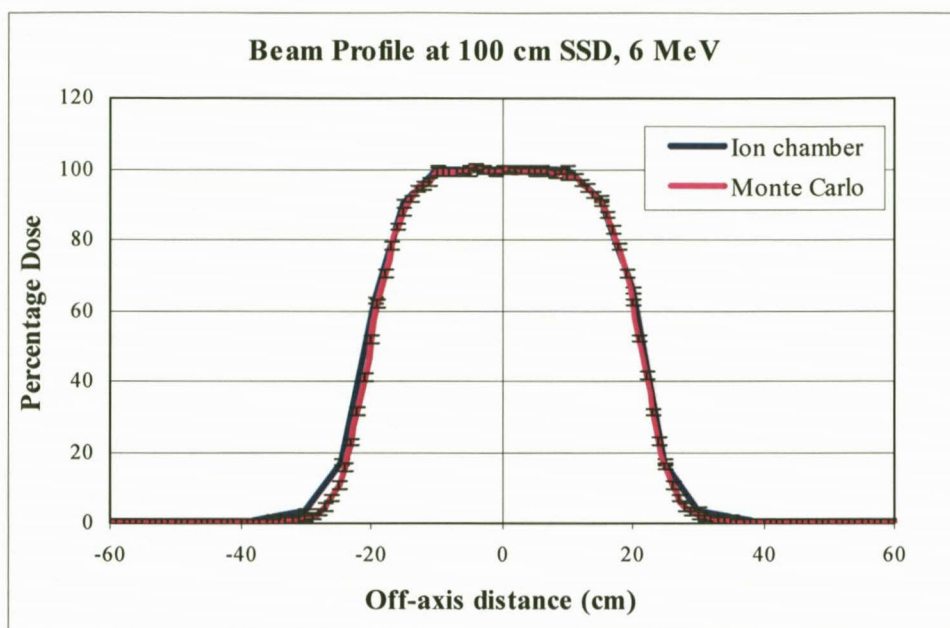


Figure 5.41. Beam profiles measured with ion chamber and calculated with MC at the isocentre (100 cm SSD) for 6 MeV at the depth of d_{\max} .

The computed beam profiles at the isocentre (100 cm SSD) agrees with measurement within statistical uncertainties of 2%. We also verified the above-determined beam parameters at the extended distance. The statistical uncertainties were less than $\pm 2\%$ near the beam. For the beam profiles at the treatment plane the agreement between MC and measurements was nearly as good as at 100 cm SSD.

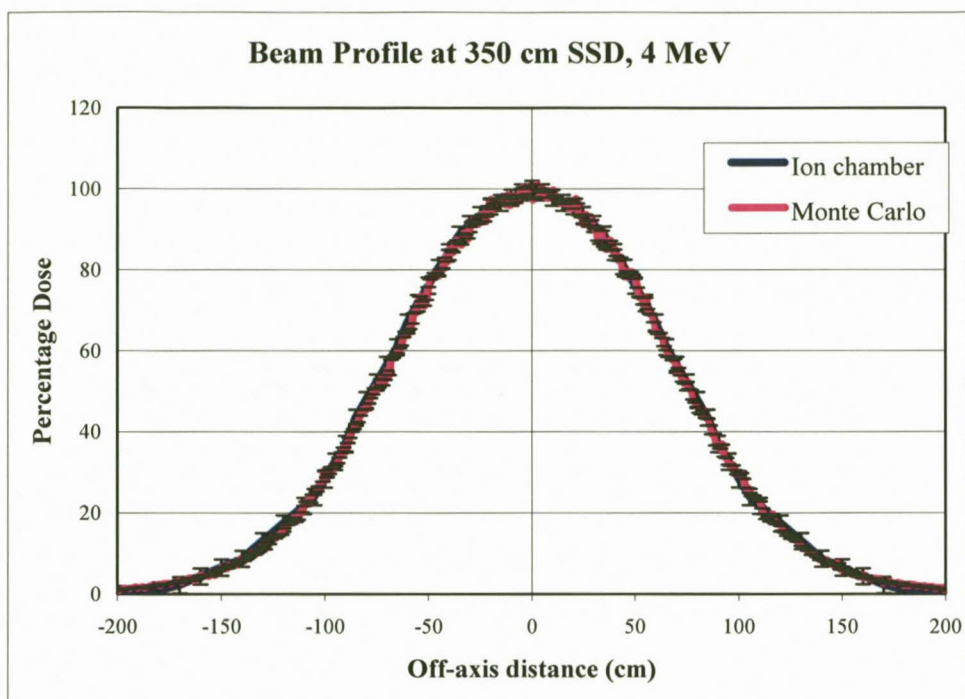


Figure 5.42. Beam profiles measured with ion chamber and calculated with MC at the treatment plane (350 cm SSD) for 4 MeV at the depth of d_{\max} .

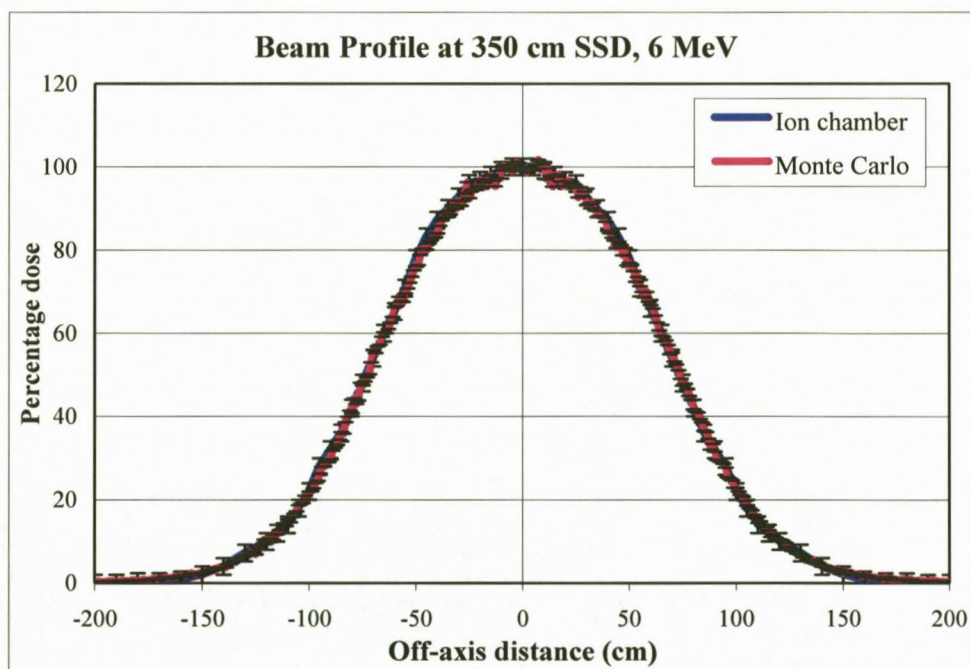


Figure 5.43. Beam profiles measured with ion chamber and calculated with MC at the treatment plane (350 cm SSD) for 6 MeV at the depth of d_{\max} .

5.8.9 Comparison between dose distributions in a Rando Phantom calculated by Monte Carlo and measured by film

5.8.9.1 Percentage depth doses

5.8.9.1.1 Introduction

Figures 5.44 to 5.51 show PDDs extracted from the complete six dual fields dose distribution at the levels mentioned before in chapter 4 (section 4.3.3), (Head, Thorax, Navel and Pelvis) in the Rando phantom. Each figure shows the PDDs measured by using EDR2 film and calculated using the MC method. The curves represent the PDD along the lines of intersection of the transverse planes at each level, and the plane containing the central axis of the two angled fields incident from the anterior of the phantom. The statistical uncertainties in dose are displayed on the curves.

5.8.9.1.2 Head level

The PDD curves at the head level are shown in figures 5.44 and 5.45 for 4 and 6 MeV energies respectively. The measured and calculated PDD curves for both energies show some disagreement. For the 4 MeV, the measured surface dose is less than that calculated by MC. This deviation is due to the 4mm aperture diameter of the film densitometer detector. The region above and below the 50 % depth shows some difference of the dose between MC and film dose. These discrepancies represent a difference of about 2 mm in depth.

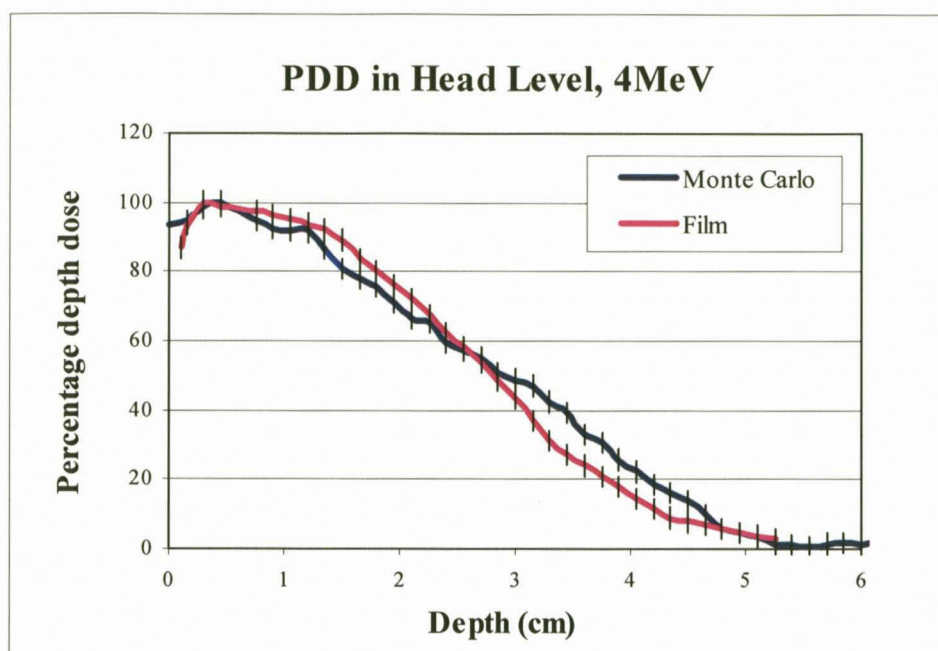


Figure 5.44. Percentage depth dose curves for 4 MeV, derived from the dose distribution (at the head level) resulting from the complete six dual-field irradiation of a Rando phantom. Curves represent dose along a line in the plane containing the two anterior fields, and perpendicular to the surface of the phantom.

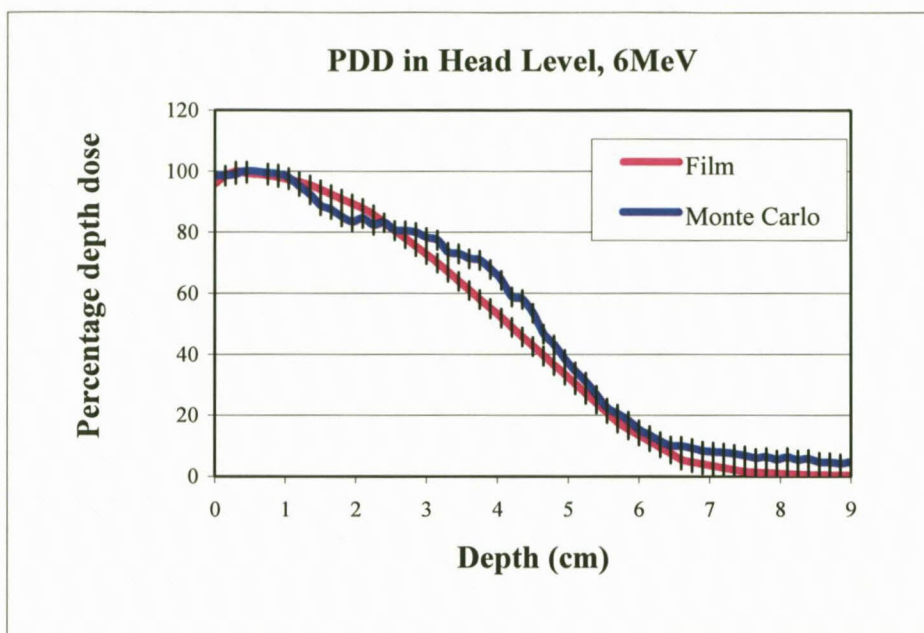


Figure 5.45. Percentage depth dose curves for 6 MeV, derived from the dose distribution (at the head level) resulting from the complete six dual-field irradiation of a Rando phantom. Curves represent dose along a line in the plane containing the two anterior fields, and perpendicular to the surface of the phantom.

For the 6 MeV there was a good correspondence between Film and MC from the depth of maximum up to a depth of 1 cm, and after that there are some differences.

5.8.9.1.3 Thorax level

The PDD curves at thorax level are shown in figures 5.46 and 5.47 for both energies. The film measured curves show a good correspondence with MC, particularly for the 4 MeV, except for the region at the surface where the film curve shows a lower value than the MC for the same reason as stated before (section 5.8.9.1.2). For the 6 MeV curves the difference beyond the d_{\max} depth are within 1 mm.

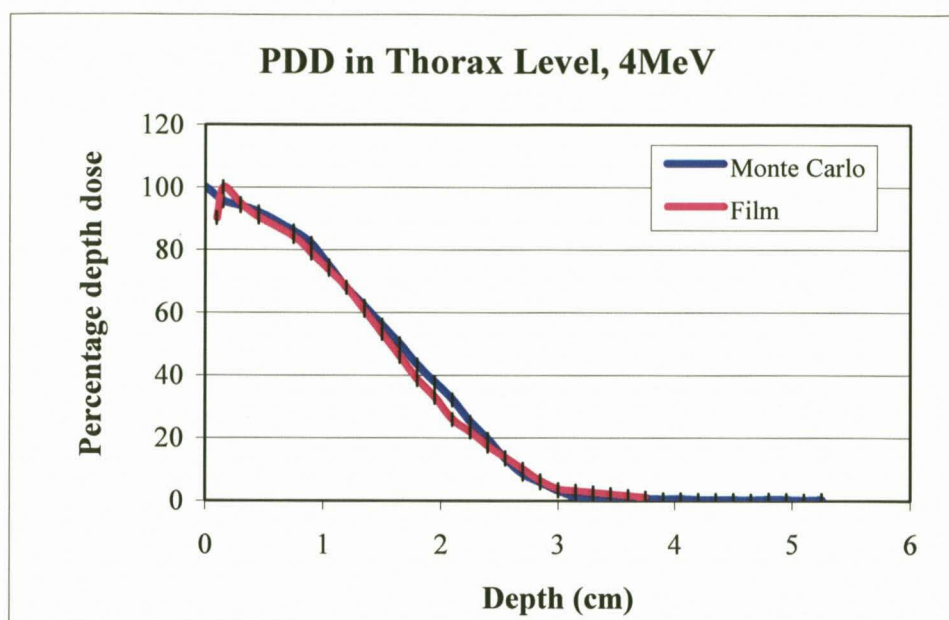


Figure 5.46. Percentage depth dose curves for 4 MeV, derived from the dose distribution (at the thorax level) resulting from the complete six dual-field irradiation of a Rando phantom. Curves represent dose along a line in the plane containing the two anterior fields, and perpendicular to the surface of the phantom.

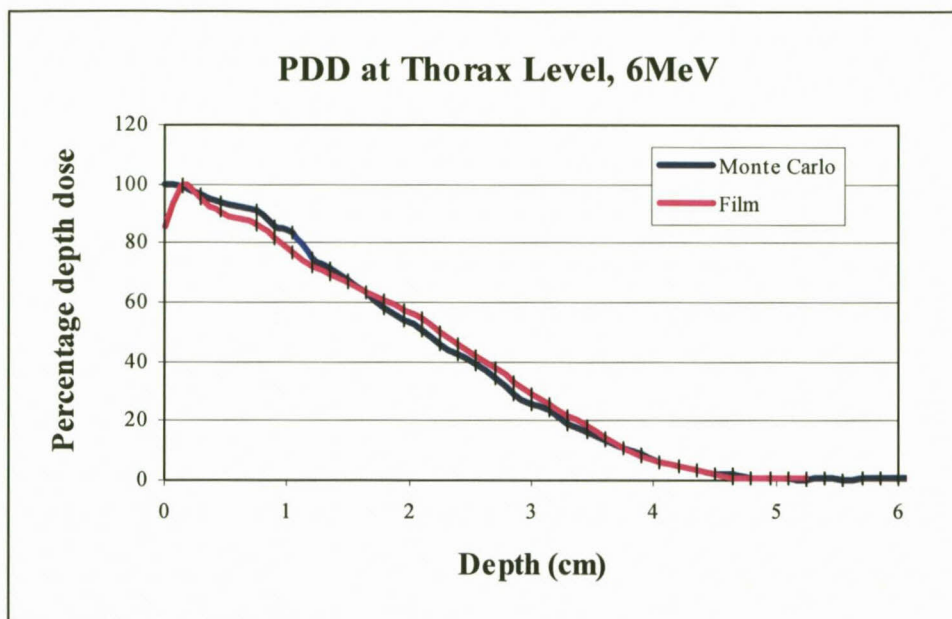


Figure 5.47. Percentage depth dose curves for 6 MeV, derived from the dose distribution (at the thorax level) resulting from the complete six dual-field irradiation of a Rando phantom. Curves represent dose along a line in the plane containing the two anterior fields, and perpendicular to the surface of the phantom.

5.8.9.1.4 Navel level

Figures 5.48 and 5.49 show the PDD curves in the navel plane for the 4 MeV. The film curve after d_{\max} is in good agreement with MC. The deviation at the depth greater than R80 may be due to experimental error in positioning the film for scanning. For the 6 MeV the film and MC methods are in good agreement with the exception of a small variation in a region around the depth of maximum dose (d_{\max}).

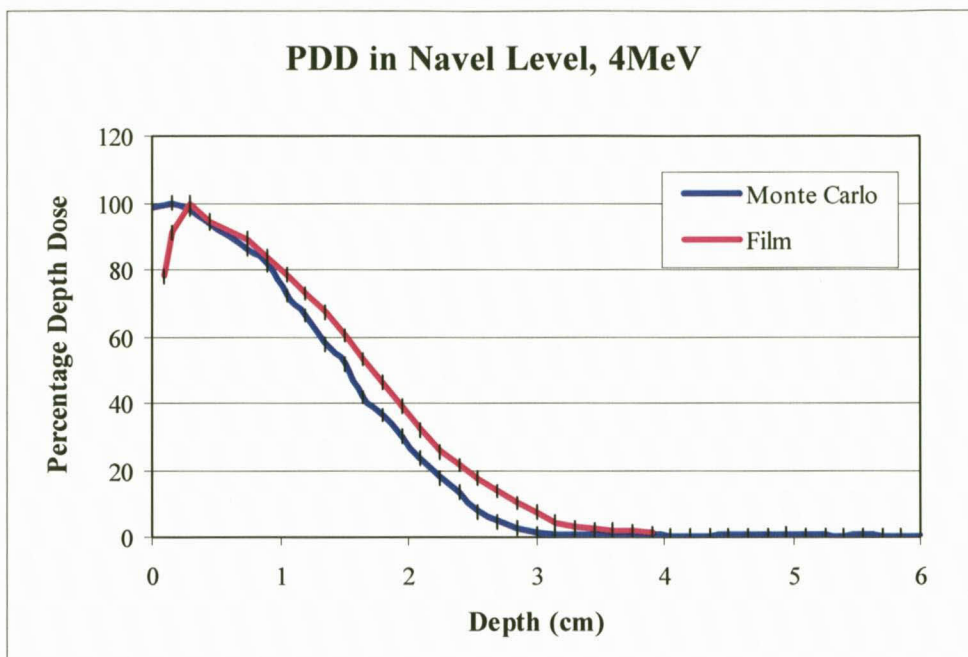


Figure 5.48. Percentage depth dose curves for 4 MeV, derived from the dose distribution (at the navel level) resulting from the complete six dual-field irradiation of a Rando phantom. Curves represent dose along a line in the plane containing the two anterior fields, and perpendicular to the surface of the phantom.

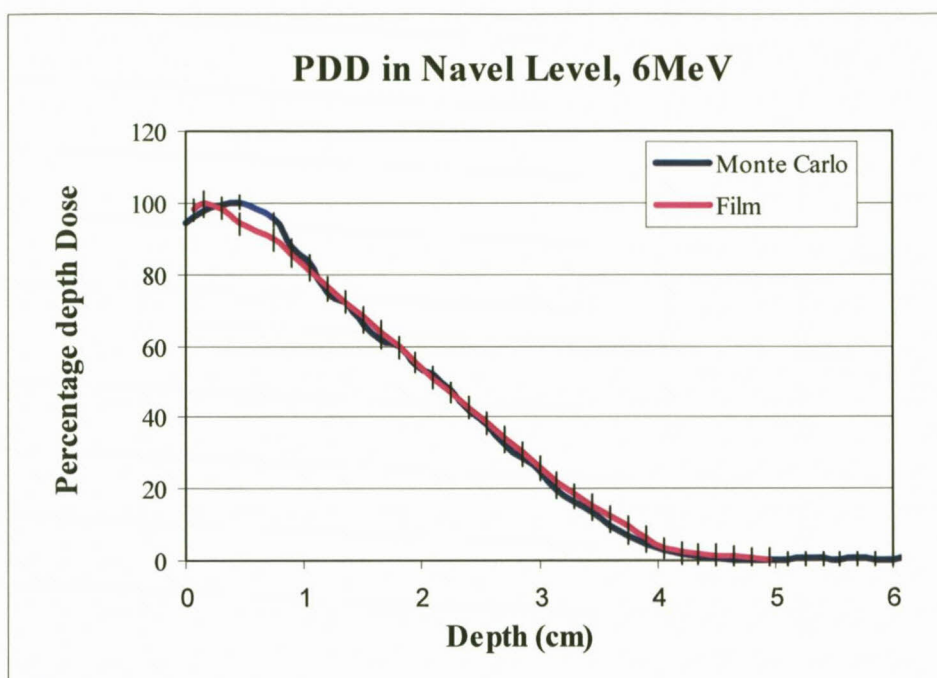


Figure 5.49. Percentage depth dose curves for 6 MeV, derived from the dose distribution (at the navel level) resulting from the complete six dual-field irradiation of a Rando phantom. Curves represent dose along a line in the plane containing the two anterior fields, are perpendicular to the surface of the phantom.

5.8.9.1.5 Pelvis level

For the pelvis case it is seen there that is a marked variation in depth dose curves for 4 MeV except in a region between 1 to 2 cm depths as shown in figure 5.50. The region close to the d_{\max} have a difference in dose of about 5 % and after that the two methods have the same depth doses until just before the depth of 30 % dose.

Figure 5.51 shows the PDD curves for the 6 MeV. There is reasonable agreement between the two curves with the maximum deviation in depth of 2 mm between the curves.

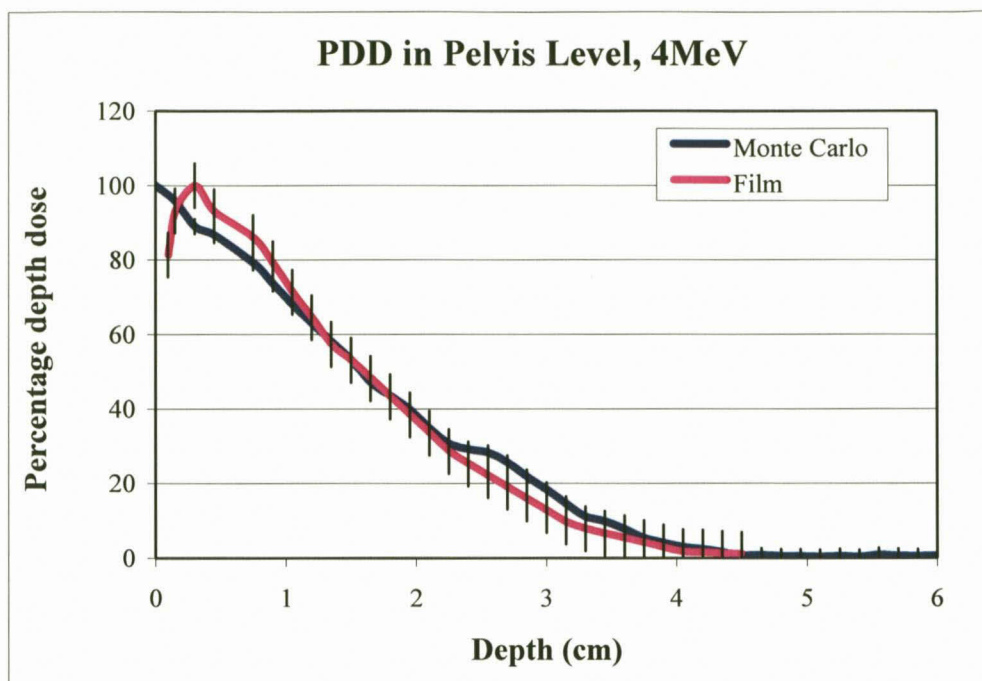


Figure 5.50. Percentage depth dose curves for 4 MeV, derived from the dose distribution (at the pelvis level) resulting from the complete six dual-field irradiation of a Rando phantom. Curves represent dose along a line in the plane containing the two anterior fields, and perpendicular to the surface of the phantom.

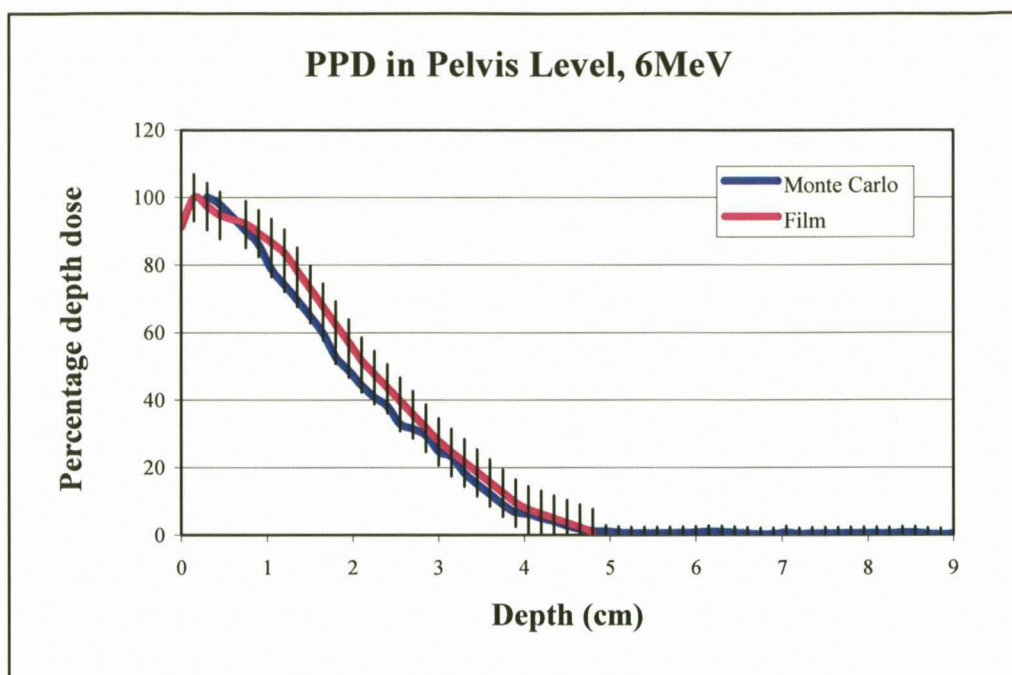


Figure 5.51. Percentage depth dose curves for 6 MeV, derived from the dose distribution (at the pelvis level) resulting from the complete six dual-field irradiation of a Rando phantom. Curves represent dose along a line in the plane containing the two anterior fields, and perpendicular to the surface of the phantom.

5.8.9.2 Isodose distributions

5.8.9.2.1 Introduction

To meet the objective of the study, dose distributions for the two energies 4 MeV and 6 MeV were calculated using the DOSXYZ code and compared with corresponding dose distributions obtained by film measurements. The number of histories used in the MC simulation was fixed for both energies. After carrying out trial simulations, it was found that 600 million histories were adequate to obtain a percentage error of about 2 percent. The 2-dimensional dose distributions for the head, thorax, navel and pelvis level are shown in figures 5.52 to 5.59. The PDD curves derived from these dose distributions gave an indication of how well film and MC methods agreed (see the previous section).

5.8.9.2.2 Head Level

Six dual-fields dose distributions for the different energies (4 and 6 MeV) were calculated using MC and measured with film methods. In all cases, the six pairs of dual fields were arranged with angles of incidence 60 degrees apart. For comparison of MC and film the dose to entire skin was normalized at the calibration point which is near to the skin surface at the navel level, at a depth of 2 and 3 mm for 4 and 6 MeV respectively.

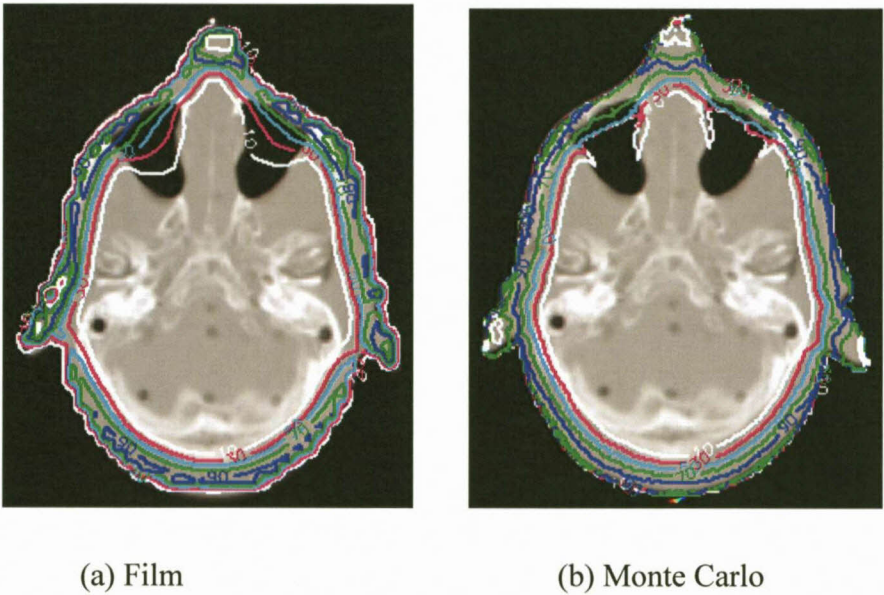


Figure 5.52: A comparison of dose distributions around the skin surface at the head level (normalized at the skin prescription point) for the film (a) and MC (b) for 4 MeV. The isodose lines are represented by 10 Percent = white, 30 percent = red, 50 percent = light blue, 70 percent = light green, 90 percent = dark blue and 100 percent = dark green.

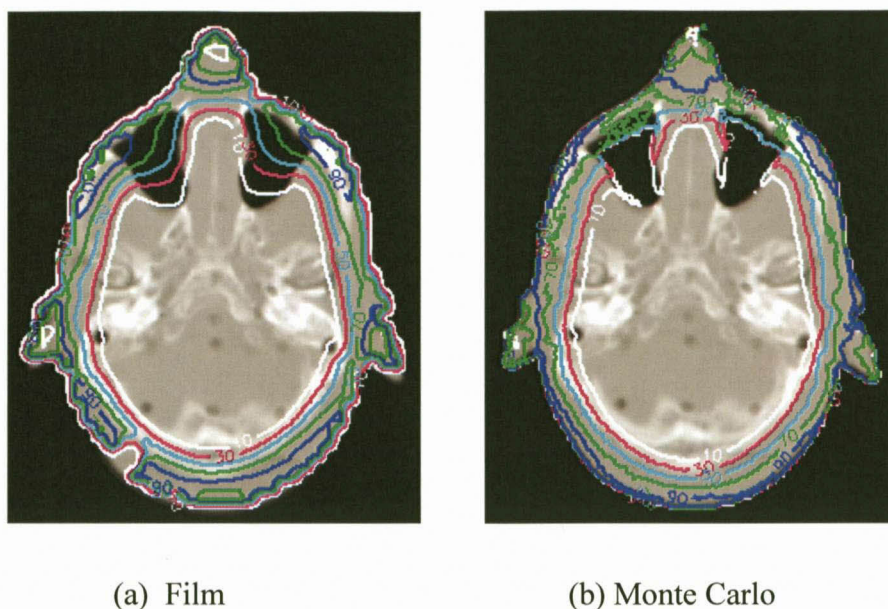


Figure 5.53: A comparison of dose distributions around the skin surface at head level (normalized at the skin prescription point) for the film (a) and MC (b) for 6 MeV. The isodose lines are represented by 10 Percent = white, 30 percent = red, 50 percent = light blue, 70 percent = light green, 90 percent = dark blue and 100 percent = dark green.

From Figure 5.52 notice that the dose distributions for the head level calculated with MC and with film appear very similar. The MC calculated dose shows slight deviations compared to the film, particularly in the area of the nasal cavity (in the vicinity of the 10% and 30 % isodose lines). These deviations in dose distributions are due to the fact that the MC method was configured not to calculate the dose in air cavities and it defaults to zero dose there. For both methods the doses at the surface fluctuate between 90 to 100 percent which is due to the effect of the overlapping beams from different angles of incidence (as explained in chapter4, section 4.3.3).

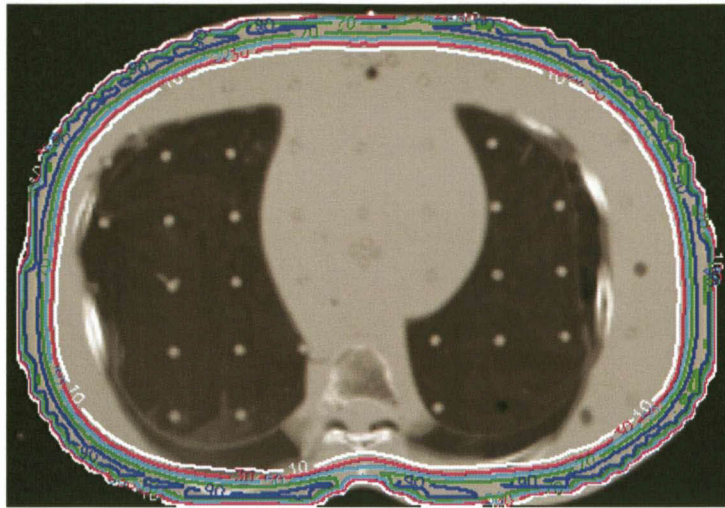
Also for both methods the dose distributions are higher in the areas that have sharp protrusions due to the larger degree of overlap and penetration of beams in those areas (e.g. nose and ear areas). There is a decrease in dose in the areas shielded by protrusions. In figure 5.53, the film dose distribution shows a discontinuity in isodose lines near the back of the head which is due to an artefact created during the film processing.

In general the film and MC dose distributions agree well. The dose distribution for the higher energy (6 MeV) clearly shows a greater depth of penetration in both the above figures.

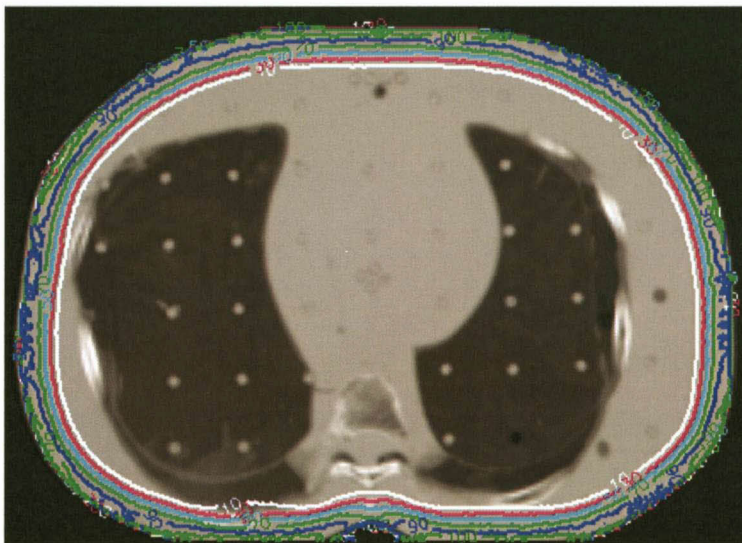
5.8.9.2.3 Thorax level

Figures 5.54 and 5.55 show the dose distributions at the thorax level for both MC and film at 4 and 6 MeV.

The dose distribution shows some hot spots in the direction of 60 degree beam incidence which results from the overlapping of the fields. Also we observe that the dose distribution penetrate small areas of the posterior part of the left lung as shown for both methods in particular in case of 6 MeV, that is due to larger penetration of this energy. The interesting feature here is that the film method tends to follow MC method in the isodose lines in that area of the lung and this is quite apparent at the higher energy as shown in figure 5.55.

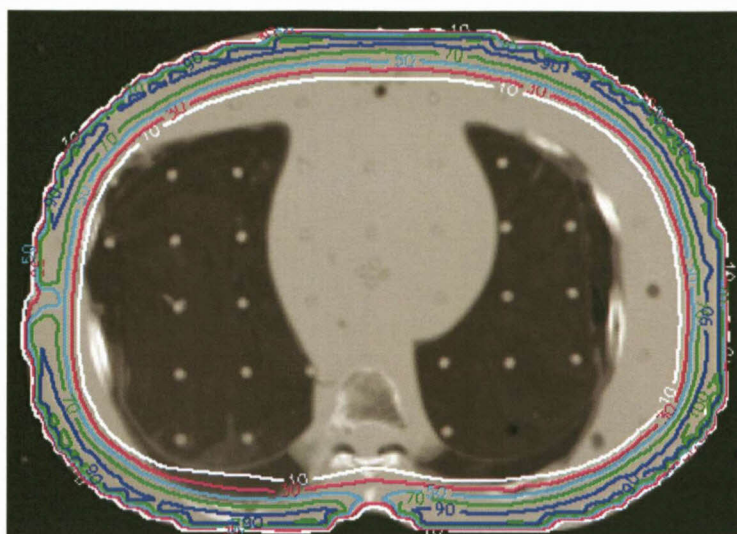


(a) Film

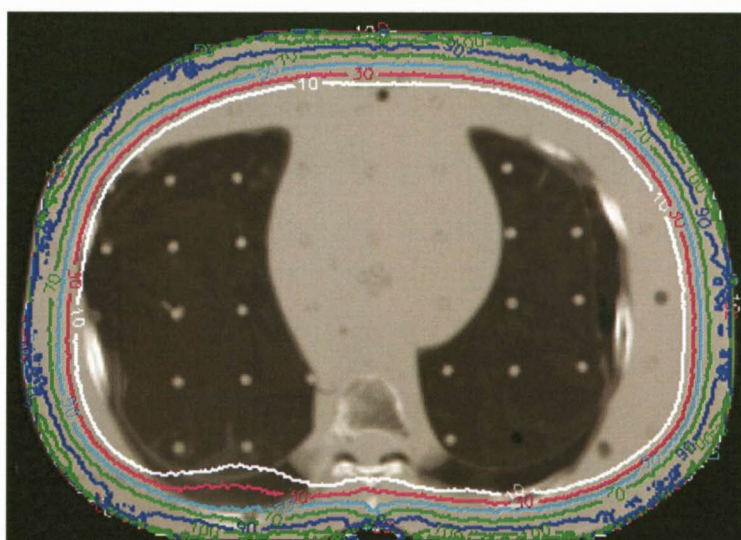


(b) Monte Carlo

Figure 5.54: A comparison of dose distributions around the skin surface at the thorax level (normalized at the skin prescription point) for the film (a) and MC DOSXYZ (b) for 4 MeV. The isodose lines are represented by 10 Percent = white, 30 percent = red, 50 percent = light blue, 70 percent = light green, 90 percent = dark blue and 100 percent = dark green.



(a) Film

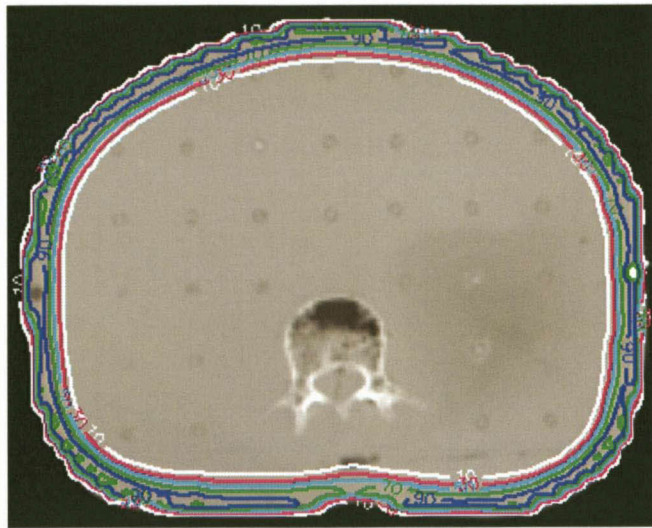


(b) Monte Carlo

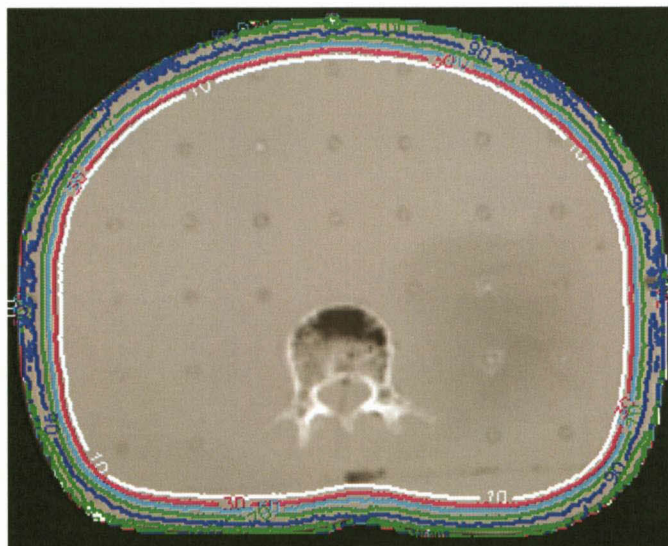
Figure 5.55: A comparison of dose distributions around the skin surface at the thorax level (normalized at the skin prescription point) for the film (a) and MC (b) for 6 MeV. The isodose lines are represented by 10 Percent = white, 30 percent = red, 50 percent = light blue, 70 percent = light green, 90 percent = dark blue and 100 percent = dark green.

5.8.9.2.4 Navel Level

The navel dose distributions are illustrated in figures 5.56 and 5.57. This is the plane where the dose distribution was normalized for the whole of the skin surface. The figures indicate that the dose distributions for the navel level at the skin surface calculated by MC and film are very similar. For 6 MeV the dose distributions have a deeper penetration depth.

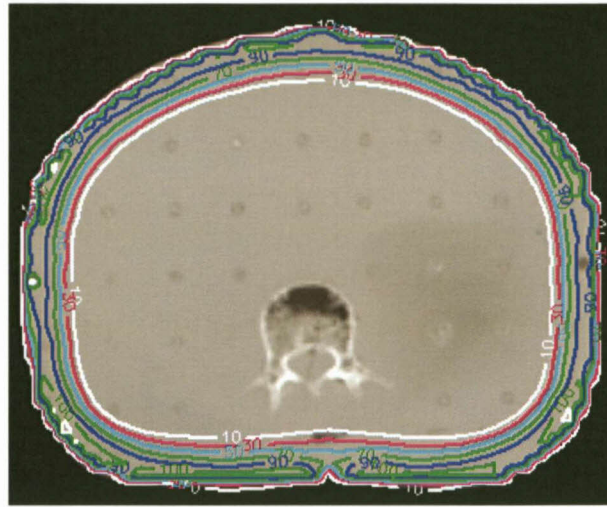


(a) Film

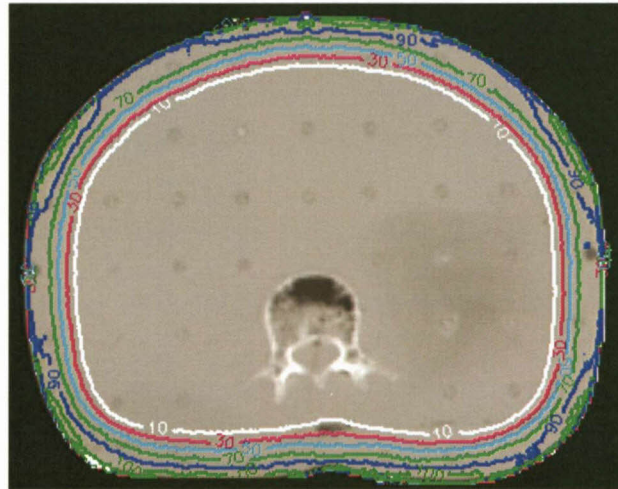


(b) Monte Carlo

Figure 5.56: A comparison of dose distributions around the skin surface at the navel level (normalized at the skin prescription point) for the film (a) and MC (b) for 4 MeV. The isodose lines are represented by 10 Percent = white, 30 percent = red, 50 percent = light blue, 70 percent = light green, 90 percent = dark blue and 100 percent = dark green.



(a) Film

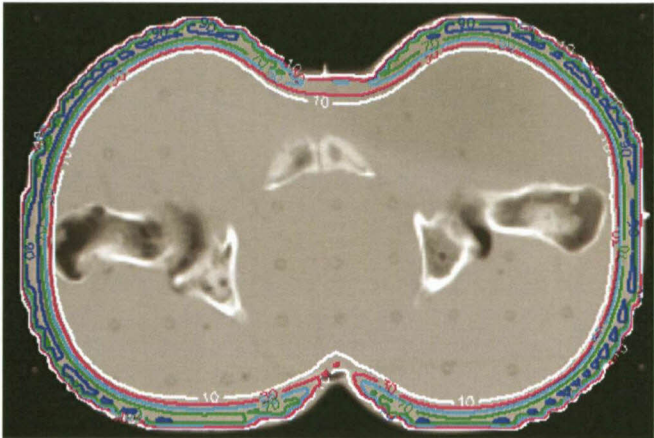


(b) Monte Carlo

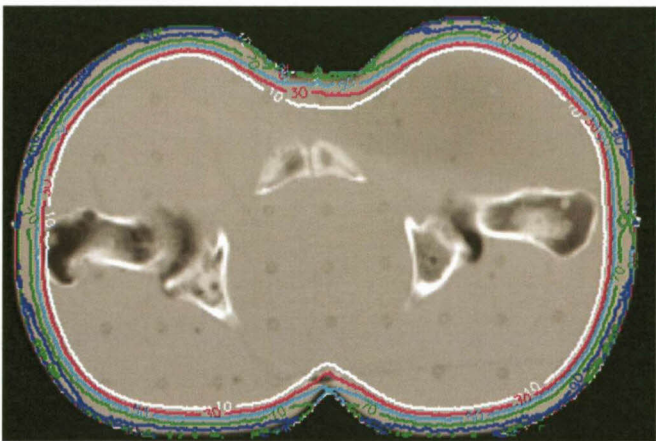
Figure 5.57: A comparison of dose distributions around the skin surface at the navel level (normalized at the skin prescription point) for the film (a) and MC (b) for 6 MeV. The isodose lines are represented by 10 Percent = white, 30 percent = red, 50 percent = light blue, 70 percent = light green, 90 percent = dark blue and 100 percent = dark green.

5.8.9.2.5 Pelvis level

Figures 5.58 and 5.59 show the dose distributions at the Pelvis level for both 4 and 6 MeV. The film dose distribution (a) show slight deviations compared to MC (b). This is indicated by the discontinuity in the isodose lines in the inner curvature regions at the pelvis surface. Otherwise the dose distributions are quite similar.

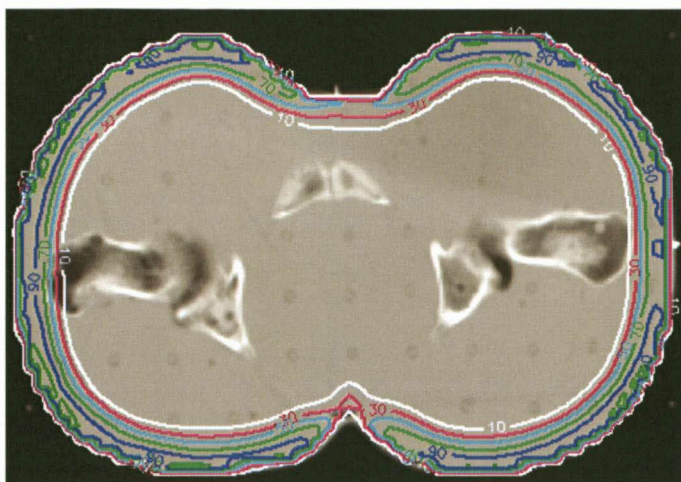


(a) Film

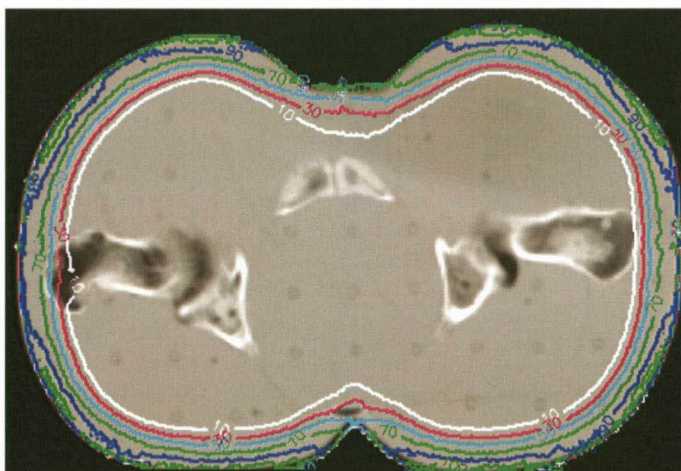


(b) Monte Carlo

Figure 5.58: A comparison of dose distributions around the skin surface at the pelvis level (normalized at the skin prescription point) for the film (a) and MC (b) for 4 MeV. The isodose lines are represented by 10 Percent = white, 30 percent = red, 50 percent = light blue, 70 percent = light green, 90 percent = dark blue and 100 percent = dark green.



(a) Film



(b) Monte Carlo

Figure 5.59: A comparison of dose distributions around the skin surface at the pelvis level (normalized at the skin prescription point) for the film (a) and MC (b) for 6 MeV. The isodose lines are represented by 10 Percent = white, 30 percent = red, 50 percent = light blue, 70 percent = light green, 90 percent = dark blue and 100 percent = dark green.

5.8.9.3 Statistical uncertainty analysis

The Monte Carlo calculation method is subject to statistical uncertainties due to the stochastic nature of the radiation transport process. The number of histories that is needed to reduce the uncertainties of a given number of histories by half is equal to 4 times the initial number of histories (see section 4.3.1). The statistical uncertainties in these MC dose distributions were about 2 percent. This was achieved by running a large enough number of histories. The statistical errors also depend on the actual voxel size of the CT phantom, which was determined by the scan setting of the CT scanner. These voxel sizes were $1.5 \times 1.5 \times 10 \text{ mm}^3$ for the whole phantom.

For the film dose distribution the statistical errors were 3, 2, 3, and 6 percent for the head, thorax, navel and pelvis respectively. The overall statistical error for the film data was calculated as follows: the average value to the dose at each point of three films was determined as well as the standard deviation at each point. A global standard deviation was then calculated as the average of the point standard deviations. This global standard deviation was indicated as the error bars in the percentage depth dose curves for film in the previous figures (section 5.8.9.1).

6 CONCLUSION AND RECOMMENDATIONS

The main purpose of this study was to commission and optimize a total skin electron therapy (TSET) technique for the treatment of mycosis fungoides with the Elekta Precise linear accelerator using the high dose rate electron (HDRE) mode that is installed on the machine. This was done through an extensive set of measurements and a large number of Monte Carlo simulations. It is generally accepted that MC simulation is the most accurate way to obtain detailed information about any radiation beam and its accompanying dose distributions. In this research the Monte Carlo beam models were validated by matching the simulated beam data at different scoring planes with corresponding measurements. From the previous chapters several conclusions can be made:

- 1) The HDRE mode is a useful facility providing reasonable dose output and field size, and acceptably low levels of x-ray contamination. The dose uniformity and dose rate at the treatment plane (at 350 cm SSD) meets the recommendation (AAPM No. 23) concerning beam flatness and x-ray contamination (less than 2%), and it considerably reduces the treatment time of TSET while retaining proper functioning of all accelerator dosimetry systems. Moreover the machine can be easily set up for treatment without additional technical support. Nevertheless the TSET with HDRE mode requires careful calibration and a well controlled procedure to carry out the treatment.
- 2) Use of a dual field technique produces acceptable beam uniformity over an area large enough to allow total skin electron therapy in the existing treatment room. This uniformity was achieved through optimization of the angles of incidence of the two beams forming the composite dual field in the vertical direction.
- 3) The absolute calibration of absorbed dose to the patient requires the measurement of the ratio "*skin dose to calibration point dose*". The value of this ratio (also called overlap factor) was found to vary between 2.4 and 2.9 for the different dosimeters used in this study. To assess the effective treatment depth and the degree of

bremsstrahlung contamination, it is necessary to measure the percentage depth dose curves for the complete treatment using all twelve fields on a cylindrical phantom. From the results it can be concluded that the depth of maximum dose (d_{\max}) is approximately 2 and 3 mm and the therapeutic range (R_{80}) is approximately 7 and 9 mm for the 4 and 6 MeV beam energies respectively. Therefore the depth doses (in cylindrical phantoms) from multiple beams can indicate to the clinician the effective treatment depth.

- 4) Monte Carlo simulation of a linear accelerator can provide information such as fluence, energy fluence, energy spectra and angular distributions of the radiation beam which is almost impossible to measure. The BEAMDP code allows this information to be acquired from the phase space files produced by BEAM at any scoring plane. This detailed information about the radiotherapy beam increased our understanding of the clinical beam characteristics especially for the TSET technique. Some investigators have used this information to improve accelerator design and improve accuracy of dosimetry (Pavón et al, 2003 and Sung et al, 2005).
- 5) The results have proven that the MC method can accurately reproduce the measurements in non-standard conditions such as the TSET technique by acquiring the large beam profiles in a $400 \times 200 \times 24 \text{ cm}^3$ phantom at the patient treatment plane. This confirms the suitability of the DOSXYZ Monte Carlo code for the calculation of the beam data in a 3D water phantom at extended SSD. The agreement between the MC calculated data and corresponding data obtained by measurements are remarkably good. Results agree within less than 2% except for the areas near the field edges at the treatment plane.
- 6) The Monte Carlo method can also be used to calculate dose distributions throughout a 3D volume constructed from CT slices. Dose distributions were generated with the DOSXYZ code at different levels in a CT based model of the Rando phantom from the twelve fields incident at the patient treatment plane. The results agree well with the film measurements done at the corresponding levels in the phantom, with

relatively small discrepancies at a few positions. This confirms the validity of the assumptions that dose distributions can be determined with acceptable accuracy anywhere in the 3D volume of a suitable patient model.

- 7) A large number of histories are required to achieve adequate statistical uncertainty in the dose distributions. Because of this the Monte Carlo simulation time was relatively long using the available computing facilities. For example a complete treatment using six dual fields took about 72 hours on a 2.41 GHz Pentium IV PC.
- 8) The dose distributions in phantom were found to comply with the guidelines described in the AAPM TG-23 protocol, showing the suitability of this technique for treatment of mycosis fungoides. This also shows the advantage of using MC as a treatment commissioning and optimization tool for TSET.

RECOMMENDATIONS:

- 1) The final delivered treatment dose will include the effect of the overlap factor. This relates the true average skin dose (due to beam overlap) to the calibration dose. It must be understood that this factor plays a very important role in the final patient treatment dose. Therefore the actual patient dose should be checked during treatment using TLD.
- 2) A detailed treatment protocol should be established for the clinical implementation of the TSET technique, dealing with: i) The equipment used in this technique, ii) The calibration and preparation of equipment immediately prior to TSET treatment and iii) The measurements of the actual dose delivered to the patient during the TSET procedure.

- 3) Although the MC calculations currently take a long time, the patient population requiring TSET is relatively small and one can use MC techniques to assess the dose distribution in this technique with current PC computer facilities.
- 4) The MC beam model developed in this research project for the 4 and 6 MeV electron beams of the Elekta Precise in HDRE mode makes it possible in principle to calculate the dose distributions for individual patients providing that a suitable anatomical model can be constructed for the patient in the actual treatment position. This could possibly be done by applying 3D optical reconstruction of the patient surface from multiple video frames acquired during a complete revolution of the treatment platform. This is currently being investigated as a possible follow up research project.

REFERENCES

AAPM, Task Group 21., 1983, "A protocol for the determination of absorbed dose from high-energy photon and electron beams", *Med Phys*; 10:741–771.

AAPM, Task Group 23., 1988, "Total skin electron therapy: technique and dosimetry. New York: American Institute of Physics.

Ali A.O., 2001, "Dosimetry of the electron beam", Thesis submitted for M.Med.Sc degree, University of the Free State.

Andreo P., 1991, "Monte Carlo techniques in medical radiation physics", *Phys. Med. Biol.* 36, 861 – 920.

Andrews J.R and Swain R.W., 1957, "The radiation therapy of human cancer with accelerated atomic particles", *Med. Ann. of Dist. of Col.* XXVI, 13-16.

Antolak J.A, Bieda M.R, and Hogstrom K.R., 2002. "Using Monte Carlo methods to commission electron beams: A feasibility study," *Med. Phys.* 29, 771-786.

Awusi K., 2000, "Using Monte Carlo Techniques to Evaluate the Dose Distributions from A Radiotherapy Treatment Planning System", Thesis submitted for M.Med.Sc degree, University of the Free State.

Beaulieu L et al., 2003, "Overview of Geant4 applications in medical physics", *Proceedings of IEEE-NSS*, Portland.

Berger M. J., 1963, "Monte Carlo Calculation of the penetration and diffusion of fast charged particles", in *Methods in Comput. Phys.*, edited by B. Alder, S. Fernbach, and M. Rotenberg, 1, 135 – 215, Academic, New York.

Berger M.J and Seltzer S.M., 1988 "Monte Carlo Transport of Electrons and Photons", eds. T.M. Jenkins, W.R. Nelson and A. Rindi (Plenum, New York).

Bieda M, Antolak J and Hogstrom. K., 2001, "The effect of scattering foil parameters on electron-beam Monte Carlo calculations", *Med. Phys.* 28 2527-34.

Bielajew A.F and Rogers D.W.O., 1988 "Variance reduction techniques", in 'Monte Carlo transport of electrons and photons, edited by M.Jenkins, R.Nelson and A.Rindi', 407 – 419, (Plenum press, New York and London.

Bjarngard B.E, Chen G.T.Y, Piontek R.W, and Svensson G.K., 1977, "Analysis of dose distributions in whole body superficial electron therapy", *Int. J. Radiat. Oncol. Biol. Phys.* 2:319-324.

Björk P, Nilsson P, and Knöös T., 2002, "Dosimetry characteristics of degraded electron beams investigated by Monte Carlo calculations in a setup for intraoperative radiation therapy", *Phys. Med. Biol.* 47 239-56.

Brahme A., 1984, "Dosimetric precision requirements in radiation therapy", *Acta Radiologica Oncology.* 23, 379 – 391.

Bushberg J.T, Serbert J.A, Leidholdt E.M and Boone J.M., 1994, "The essential physics of medical imaging" , (Williams and Wilkins, Baltimore, USA).

Chen Z, Alred G, Agostinelli, Lynnd, Wilson, Nather., 2004, "Matching the dosimetry characteristics of a dual-field Stanford technique to a customized single-field Stanford technique for total skin electron therapy", *Int. J. Radiation Oncology Biol. Phys.*, Vol. 59, No. 3, pp. 872-885.

Christina Z.J., 2005, "Monte Carlo simulation with Geant4 for verification of rotational total skin electron therapy (TSET)", Thesis submitted for Master of Science, Lund University, Sweden.

Cox R.S, Heck R.J, Fessenden P, Karzmark C.J, and Rust D.C., 1989, "Development of total skin electron therapy at two energies". *Int. J. Radiation Oncology Biol. Phys.*, 18:659–669.

Cunningham J.R., 1982, "Tissue inhomogeneity corrections in photon beam treatment planning", in Orton C.G (ed), *Progress in medical radiation physics*, 1, Plenum, New York.

- Ding X, Rogers D.W.O and Mackie T.D., 1995, "Calculation of stopping-power ratios using realistic clinical electron beams", *Med. Phys.* 22(5). 279-286.
- Du Plessis F.C.P., 1999, "Development of a Monte Carlo simulation method for the evaluation of dose distribution calculation of radiotherapy treatment planning system", Thesis submitted for M.Med.Sc degree, University of the Free State, (1999).
- Ekstrand K.E, Dixon R.L., 1982, "The problem of obliquely incident beams in electron-beam treatment planning", *Med. Phys.* 9:276-278.
- Faddegon B, Balogh J, Mackenzie R. and Scora D., 1988, "Clinical considerations of Monte Carlo for electron radiotherapy treatment planning", *Rad. Phys. Chem.* 53 217-27.
- Ferrari A, Sala P.R, Fassò A, Ranft J., 2005, "FLUKA: a multiple-particle transport code", CERN-2005-(10), INFN/TC 05/11, SLAC-R-773.
- Griffiths S and Short S., 1994, "Radiotherapy: principles to practice: A manual of quality in treatment delivery".
- Halbleib J.A, and Melhorn T.A., 1992, "ITS: The integrated TIGER series of Coupled Electron/Photon Monte Carlo Transport Codes", Sandia Report SAN84-0073, Sandia National Laboratories, Albuquerque, New Mexico.
- Haybittle J.L., 1957, "The protection of multicurie strontium-yttrium (90) sources", *Phys. Med. Biol.* 1:270-276.
- Holt J.P, Perry D.J., 1982, "Some physical considerations in whole skin electron beam therapy", *Med. Phys.* 9:769-776.
- Hoppe R.T, Fuks, Bagshaw Z. M.A., 1979, "Radiation therapy in the management of cutaneous T-cell lymphomas", *Cancer Treat. Rep.* 63:625-632.
- ICRU., 1984, "Radiation dosimetry: Electron beams with energies between 1 and 50 MeV", ICRU Report 35 (ICRU, Bethesda, U.S.A).
- ICRU., 1984 "Stopping powers for electrons and positrons", ICRU Report 37 (ICRU, Bethesda, U.S.A).

ICRU., 1987, "Use of computers in external beam radiotherapy procedures with high energy photons and electrons", ICRU Report 42 (ICRU, Bethesda USA).

IDL, ITT Visual Information Solutions, www.ittvis.com

Jette D., 1983, "The application of multiple scattering theory to therapeutic electron dosimetry", *Med Phys.* 10:141.

Johns H.E, and Cunningham J.R., 1983, "The Physics of Radiology", Charles C Thomas, Springfield, Illinois.

Karzmark C.J, Anderson J, Buffa A., 1988, "Total skin electron therapy: Technique and dosimetry", AAPM Report. New York: American Institute of Physics.

Kawrakow, I, Fippel M, and Friedrich K., 1996, "3D Electron Dose Calculation using a Voxel based Monte Carlo Algorithm", *Med. Phys.*, 23:445 – 457.

Khan F.M., 2003, "The physics of radiation therapy", Third Edition (Williams and Wilkins, Baltimore, USA)

Kumar P.P, Patel I.S., 1978, "Rotation technique for superficial total body electron beam irradiation", *J. Natl. Med. Assoc.* 70:507-509.

Kutcher G.J., 1992, "Quantitative plan evaluation", in Purdy J.A, (ed), "Advances in radiation oncology physics: Dosimetry, treatment planning and brachytherapy", American Association of Physicists in Medicine, Medical physics Monograph No 19, American Institute of Physics.

Lewis R.D, Ryde S.J.S, Hancock D.A and Evans C.J., 1999, "An MCNP- Based model of a linear accelerator x-ray beam", *Phys. Med, Biol.* (44), 1219-1230.

Lo TCM, Salzman FA, Moschella SL, Tolman EL Wright KA., 1979, "Whole body surface electron irradiation in the treatment of mycosis fungoides", *Radiology.* 130: 453-457.

Ma C-M and Jiang S.B., 1999, "Monte Carlo modeling of electron beams from medical accelerators", *Phys. Med. Biol.* 44 (12), 157 –187.

Ma C-M and Rogers D W O., 2005, "BEAMDP user manual". NRCC Report PIRS-0509(C)revA, (NRC, Ottawa, Canada).

Mackie T.R, 1990, "Application of Monte Carlo methods in radiotherapy dosimetry of ionizing radiation" Vol 3, eddited by K.Kase, B.Bjamgand and F.H.Attix, 541 - 620 (San Diego, CA academics)

Metcalfe P, Kron T, Hoban P., 1997"The physics of radiotherapy X-rays from linear accelerators", 1st edition (Medical Physics publishing, Wisconsin, USA)

Mohan R., 1988, "Monte Carlo simulation of radiation treatment machine heads" in 'Monte Carlo transport of electrons and photons, edited by M.Jenkins, R.Nelson and A.Rindi', 453 - 467, (Plenum press, New York and London).

Mohan R., 1997, "Monte Carlo dose calculation for radiation treatment planning", Med. 24 Phys.

Mohan B.B., 1999, "Lecture notes on: Introduction to clinical radiotherapy", (16150, Kubang Kerian, Kelantan, Malaysia).

Nahum A.E, 1988, "Overview of photon and electron Monte Carlo", in 'Monte Carlo transport of electrons and photons, edited by M.Jenkins, R.Nelson and A.Rindi', 3 – 21, (Plenum press, New York and London)

Nelson W. R, Jenkins M., and Rindi A., 1988, "Monte Carlo transport of electrons and photons", Plenum press, New York.

Pavón C, Sánchez-Doblado F, Leal A, Capote R, Lagares J.I, Perucha M, and Arráns R., 2003, "Total skin electron therapy treatment verification: Monte Carlo simulation and beam characteristics of large nonstandard electron fields," Phys. Med. Biol. 48, 2783-2796.

Peters V.G, and Jaywant S.M., 1995, "Implementation of total skin electron therapy using an optional high dose rate mode on a conventional linear accelerator", Medical Dosimetry, 20. (2), 99-104.

Podgorsak E.B., 2004, "Review of Radiation Oncology Physics: A Handbook for Teachers and Students", Educational Report Series. IAEA. Vienna. Austria.

Podgorsak E.B, Pla C, Pla M, Lefebvre P.Y, Heese R., 1983, "Physical aspects of a rotational total skin electron irradiation", Med. Phys. 10:159-168.

PRECISE OPERATORS MANUAL:, 2003, Chapter 11, High Dose Rate Electron Therapy (HDRE).

Proimos B.S, Wright K.A, Trump J.G., 1960, "Modification of strontium 90 emission for superficial therapy", Br. J. Radiol. 33:640-643.

Rath G.K, Mohanti BK., 2000, "Textbook of Radiation Oncology: Principles and Practice", BI Churchill Livingstone, New Delhi.

Raese D.E., 1976, "Monte Carlo principles and application", Med. Phys. 21(2), 181 – 197.

Richard P.H., 1997, "Computational Methods in Radiation Oncology", Thesis submitted for a Doctorate of Philosophy, University of Canterbury, New Zealand.

Richard T.H., 2003, "Mycosis fungoides: radiation therapy", Dermatologic Therapy, Vol. 16, 347–354.

Rogers D.W.O and Bielajew A.F., 1990, "Monte Carlo techniques of electrons and photon transport for radiation dosimetry" in 'The Dosimetry of Ionizing Radiation', edited by K.Kase, B.Bjarngard and F.Attix Vol III, 427 - 435.

Rogers D.W.O., 1991, "The role of Monte Carlo simulation of electron transport in radiation dosimetry", International Journal of Radiation and Isotopes. 42, 965 - 974.

Rogers D.W.O, Faddegon B.A, Ding G.X, Ma C.M and We J, 1995, "BEAM: A Monte Carlo code to simulate radiotherapy treatment units", Med. Phys. 22(5), 503 – 524.

Rogers D.W.O., B. Walters, I. Kawrakow, 2005, "BEAM user manual", National Research Council of Canada, NRCC Report, PIRS-0509(A)revK, (NRC, Ottawa).

- Rossi H. H and W C Roesch., 1962, "Field equations in dosimetry", *Radiat. Res.*, 16:783.
- Sung J.Ye, Pareek P. N, Spencer S, Duan J, Brezovich I.A., 2005, "Monte Carlo techniques for scattering foil design and dosimetry", *Med. Phys*, 32 (6) : 1460 –8.
- Sewchand W, Khan F.M, Williamson J., "Total-body superficial electron-beam therapy using a multiple-field pendulum-arc technique", *Radiol.* 130:493-498, (1979).
- Szur L, Silvester J.A, Bewley D.K., 1962, "Treatment of the whole body surface with electrons", *The Lancet*, pp. 1373-1377, June.
- Tetenes P.J, Goodwin P.N., 1977, "Comparative study of superficial whole-body radiotherapeutic techniques using a 4-MeV nonangulated electron beam", *Radiol.* 122:219-226.
- Turner J.R, Hugtenburg R.P, and Wynne C. J., 1995, "Total skin electron therapy at two energies on a linear accelerator". *Australasian Physical and Engineering Sciences in Medicine*, 18(4):208–220.
- Walter T. M., 1967, "Radiation Therapy", second edition (B. W. Saunders company. Philadelphia. London).
- Walters B, Kawrakow I, and Rogers D.W.O., 2005, "DOSXYZ users manual", National Research Council of Canada, NRCC Report PIRS-794 (revB), (NRC, Ottawa).
- Wambersie A, Gahbauer R.A., 1995, "Medical application of electron linacs", (Columbus, Ohio, 43210- 1228, USA).
- Williams P.C, Hunter R.D, Jackson S.M., 1979, "Whole body electron therapy in mycosis fungoides - a successful translational technique achieved by modification of an established linear accelerator", *Br. J. Radiol.* 52:302-307.
- Williamson J.F., 1989, "Radiation transport calculations in treatment planning", *Computerised Medical Imaging and Graphics*. 3. 251:268.

SUMMARY

Total skin electron therapy (TSET) is the treatment of choice for several malignant diseases of the skin (Kaposi sarcoma, mycosis fungoides). Several different techniques have been developed in various centers, in order to achieve homogeneous dose distribution over a large irradiation field ($200 \times 80 \text{ cm}^2$). However, to implement a TSET technique one has to account for a variety of parameters, from geometric (room design, space constraints) to physical (number, angle and energy of the beams). To obtain the most acceptable dose distribution an extensive set of measurements and a large number of calculations have to be performed. Therefore Monte Carlo simulation of TSET can facilitate optimization of this technique. In this study we implemented and optimized a TSET technique using 4 and 6 MeV electron beams. The dosimetric procedure intended to obtain adequate dose uniformity over the entire surface of the patient, and to reduce the patient treatment time using a high dose rate facility on the Elekta Precise accelerator.

The EGS4/BEAM code package running on a Windows based platform was used for the MC simulation. Percentage depth-dose curves and beam profiles were calculated and measured experimentally for the $40 \times 40 \text{ cm}^2$ nominal field at both 100 cm SSD and at the patient surface at the treatment plane (SSD 350 cm) for a single beam. The accuracy of the simulated beam was validated by the good correspondence (within less than 2%) between measured beam characteristic parameters (R_{50} , d_{\max} , R_p) and Monte Carlo calculated results. To obtain a uniform profile vertically, two vertical angles of incidence were used. The angle between the two beams that gave best uniformity was considered the optimum angle. The patient is to be placed on a rotating platform perpendicular to the beam and rotated through 60 degree increments to obtain six horizontal directions of beam incidence. The doses expected in the patient were measured with Kodak EDR2 films positioned at different levels between slices of a Rando phantom. TLDs were placed on the surface to relate the film measurements to dose. The delivered doses in the treatment plane were compared to simulated data that was obtained from the MC simulation.

The penetration depth of the dose distribution varied over various scanning directions between 2-3 mm and 3- 4 mm for 4 and 6 MeV respectively. This information is useful when treatment of lesions of different thickness are being considered. The composite percentage depth dose of all six dual fields for both 4 and 6 MeV yielded an 80 % dose at ~ 7 mm and ~ 9 mm depth, respectively. Good dose uniformity was achieved for both energies and it was about $\pm 5\%$ for 4 MeV and about $\pm 3\%$ for 6 MeV over a range of -100 to +100 cm. The bremsstrahlung contamination was 0.9 and 1.3 %.

Generally there was good agreement between the dose distribution calculated with MC and measured with films, thus validating our MC calculations. The dose distributions in phantom were found to comply with the guidelines described in the AAPM TG-23 protocol, showing the suitability of this technique for treatments of the skin diseases.

The HDRE is a useful operational mode providing reasonable output, field size, and X-ray contamination. Use of a dual field technique produces reasonable beam uniformity over an area large enough to allow total skin electron therapy in a conventional treatment room. Monte Carlo techniques provided a guiding principle to assist the verification of the beam characterization of a TSET technique. The absolute calibration of dose to the patient required the measurement of the ratio "skin dose to calibration point dose"; this was achieved by measurements with a parallel plate ionization chamber and TLDs.

Key Words: Total Skin Electron Therapy, Monte Carlo, High Dose Rate Electrons, Mycosis Fungoides.

OPSOMMING

Heelliggaam elektron terapie (TSET) is die behandeling van keuse vir verskeie maligne siektes van die vel (Kaposi sarkoom, mycosis fungoides). Verskeie tegnieke is ontwikkel deur verskillende sentra om 'n homogene dosisverspreiding oor 'n groot stralingsveld ($200 \times 80 \text{ cm}^2$) te bewerkstellig. Om egter die TSET tegniek te implementeer moet daar 'n verskeidenheid parameters in ag geneem word, van geometries (kamer ontwerp, ruimtelike beperkings) tot fisies (aantal, invalshoeke en energieë van die velde). Om die mees aanvaarbare dosisverspreiding te verkry moet 'n omvattende stel metings sowel as berekenings gedoen word. Om hierdie rede kan Monte Carlo (MC) simulاسie van TSET die optimisering van die tegniek vergemaklik. In hierdie studie is 'n TSET tegniek geïmplementeer en ge-optimeer vir 4 en 6 MeV elektronbundels. Die doel van die dosimetrie procedure was om aanvaarbare uniformiteit van dosis oor die hele oppervlakte van 'n pasiënt te verkry en om die behandelingstyd te verkort deur van 'n hoë dosistempo opsie (HDRE) op die Elekta Precise versneller gebruik te maak.

Die EGS4/BEAM program wat op 'n Windows gebaseerde platform geïnstalleer is, is vir die MC simulاسie gebruik. Persentasie dieptedosis krommes en bundelprofiel is bereken en ook gemeet vir die $40 \times 40 \text{ cm}^2$ nominale veld by beide 100 cm SSD en by die pasiënt oppervlak by die behandelingsvlak (350 cm SSD) vir 'n enkelveld. Die akkuraatheid van die gesimuleerde veld is geverifieer deur die goeie ooreenkoms (binne 2%) tussen gemete karakteristieke bundelparameters (R_{50} , d_{maks} , R_p) en MC berekende resultate. Om 'n uniforme vertikale profiel te verkry is twee vertikale invalshoeke gebruik. Die hoek tussen die twee velde wat die beste uniformiteit gegee het is as die optimale hoek aanvaar. Die pasiënt sal op 'n roterende platform staan, loodreg op die invalsrigting van die veld en sal roteer word deur 60 grade intervale om ses horisontale invalshoeke te bewerkstellig. Die verwagte dosis in die pasiënt is gemeet met Kodak EDR2 film wat op verskillende vlakke tussen die snitte van 'n Rando fantoom geplaas is. TLDs is op die oppervlakte geplaas om die filmmetings te koppel aan dosis. Die gelewerde dosisse in die behandelingsvlak is vergelyk met data verkry van die MC simulاسies.

Die penetrasiediepte van die dosisverspreiding oor verskillende skandeerrigtings het gevarieer tussen 2-3 mm en 3-4 mm vir die 4 en 6 MeV onderskeidelik. Hierdie inligting is waardevol wanneer behandeling van letsels met verskillende diktes oorweeg word. Die saamgestelde persentasie dieptedosis van al ses dubbelvelde vir beide 4 en 6 MeV het 'n 80% diepte van ~ 7 mm en ~ 9 mm opgelewer. Goeie dosisuniformiteit is vir beide energieë verkry en dit was $\pm 5\%$ vir 4 MeV en $\pm 3\%$ vir 6 MeV. Die bremsstrahlung kontaminasie was tussen 0.9 en 1.3 %. In die algemeen was daar goeie ooreenkoms tussen die dosisverspreidings wat bereken is met MC en die wat gemeet is met film, wat dus die geldigheid van die MC berekenings bevestig. Die dosisverspreidings in die fantoom het voldoen aan die riglyne beskryf in die AAPM TG-23 protokol, wat die toepaslikheid van hierdie tegniek vir behandeling van velsiektes bevestig.

Die HDRE opsie is 'n nuttige operasionele tegniek wat 'n redelike bundelopbrengs, veldgrootte en x-straal kontaminasie lewer. Die gebruik van die dubbelveld tegniek lewer redelike bundeluniformiteit oor 'n oppervlakte wat groot genoeg is vir heelliggaam elektronbestraling in 'n konvensionele behandelingskamer. MC tegnieke verskaf 'n riglyn om te help met die verifikasie van die bundel eienskappe vir TSET. Die absolute kalibrasie van die dosis aan die pasiënt vereis die meting van die verhouding "veldosis tot kalibrasiepunt dosis"; dit is verbry of bereek of gaedaen deur metings met 'n parallelplaat ionisasiekamer en met TLDs.

Sleutelwoorde: Heelliggaam elektronbestraling, Monte Carlo, Hoë dosistempo elektrone, mycosis fungoides.